UNIVERSITY OF HULL

Characterisation of laser processed bio-compatible materials and the realisation of electro optical diffraction gratings

A Thesis

by

Abdulsattar Ahmad Aesa

Department of Mathematics and Physics

Submitted in partial fulfilment of the requirements

for the degree of

Doctor of Philosophy in Physics

Date /07/08/2018

Accepted by the Graduate School

_____, _____

Date, Dean of the Graduate School

Abstract

Laser processing methods using excimer lasers have become very attractive for processing materials and the fabrication of micro and nano optical components. Diffraction gratings are used in a wide range of applications and require different fabrication methods. These components can be fabricated from a variety of biocompatible polymers. In this work, an Argon Fluoride (ArF) excimer laser operating at a wavelength of 193 nm has been used to process chitosan and agarose substrates. These materials have been characterised for differing laser processing conditions. Diffraction gratings and component demonstrators have been realised using Laser Direct writing (LDW) and nanoimprinting lithography (NIL). Characterisation of the ArF 193 nm laser work involves ablation threshold, optical absorption measurements and quantification of structural and morphological changes. This results can be used to identify the ideal laser fluence to be used for the production of a diffraction grating and similar optical components fabricated from chitosan. An ablation threshold of chitosan at 193 nm wavelength has been measured as 85 $mJcm^{-2}$ and an optical absorption coefficient of 3×10^{3} cm^{-1}.

A diffraction grating structure, measuring 12 µm, was generated in biocompatible materials films; chitosan and agarose, using a laser processing method. The results showed that the interaction between the laser and these materials can potentially open the pathway for a wide range of practical, real world applications such as optical and biomedical applications. Diffraction gratings with a feature size of 1 µm were successfully formed on the biocompatible material free standing films using a NIL technique. Microstructure cross grating patterning made of chitosan and agarose have been fabricated by ArF excimer laser processing using a mask projection ablation technique. Temperature rise calculations have been carried out by COMSOL™ Multi-

Physics v5.3 using a Finite Element Method (FEM), to predict the temperature rise during laser ablation processing of chitosan and agarose. In addition, COMSOL^{TM} Multi-physics v5.3 has been used to simulate the electric field in the vicinity of a diffraction grating that is illuminated with light from a HeNe laser emitting at a wavelength of 632.8 nm.

The final experimental work investigated the possibility of realising 5CB liquid crystal doped chitosan diffraction gratings doped with Sudan Black B (SBB) dye to enhance the absorption properties at 632.8 nm. Diffraction gratings was fabricated using two intersecting beams from a HeNe laser. Polymer Dispersed Liquid Crystal (PDLC) chitosan doped with 5CB and SBB dye diffraction gratings were experimentally characterised.

Acknowledgements

In the name of Allah, the Most Gracious and the Most Merciful

Alhamdulillah, all praises and thanks are to Allah who keep me composed when I shatter in the moments of grief and despair. For answering my prayers, for giving me the strength to work hard and for his blessing in completing this work.

At the point of completing this thesis, I would like to express my sincere thanks to who assisted me in my academic achievements. First of all, I would like to take this opportunity to show my sincere gratitude to my supervisor **Dr. C.D.Walton**, for his kindness, patience, support and guidance throughout my PhD's program in physics.

Many thanks to all the staff of Physics department and the University of Hull on a whole for their cooperation. I would like to express my gratitude to all those who made it possible to complete this thesis.

I am sincerely grateful to the Ministry of Higher Education and Scientific Research Iraq, the University of Kirkuk for their financial support in the form of the PhD scholarship to undertake this study at the University of Hull.

I would like to acknowledge the Iraqi cultural attaché in London for their support.

A special and unique thanks to all of my friends at the University of Hull, especially, I would like to mention my group friends for their support and help.

I would like also acknowledge Mr. T. Sinclair for his assistance with SEM measurements.

Additionally, I would like to thank Dr. Bethany Newton for her help with proof reading this thesis, it is greatly appreciated.

My deepest thanks goes to my beloved mother; who is no more in this world but her everlasting love, limitless prayers and motivation led me to the highest pursuits of life and completing the study.

I would like to thank all my family for always being there for me although in distance and for their prayers that gave me the strength to go on. Especially, I would like to give my thanks to my brother, Mohammed (Abo Samah) for his encouragement and sincere support. I would like to give a heartfelt thanks to my wife whose patient love and moral support enabled me to complete this research work. Without her sincere support and encouragement it would not have been possible for me to conduct this study. Also it would be unfair if I did not mention and thanks my sweet child Adnan, who has companioned me during my studies and the rest of my sons and my daughter for their patience and encouragement.

Papers, Poster and conference

1. Aesa AA, Walton CD. 193 nm ArF laser ablation and patterning of chitosan thin films. Appl Phys A 2018;0:0. doi:10.1007/s00339-018-1859-z.

2. Fabrication of a Surface Relief Grating from a Chitosan Thin Film using an ArF 193 nm Excimer Laser/ in progress.

3. Ablation of biopolymer with 193 nm excimer pulses/ has published as a cooperation with Coherent, Inc. /USA and it is live onto following:

https://www.coherent.com/company/news/news-and-events

Posters

1. 193 nm ArF laser ablation and patterning of chitosan film/ International conference on laser ablation (COLA 2017)

Conference

1. Attending and presented a poster in title of, 193 nm ArF laser ablation and patterning of chitosan thin film/ International conference on laser ablation (COLA 2017), 3^{rd}-8^{th} September 2017, France/ Marseille.

List of symbols

Symbols	Definition	Unit
I_0	The total intensity	Wm^{-2}
I_T	Transmitted intensity	Wm^{-2}
I_R	Reflected intensity	Wm^{-2}
I_A	Absorbed intensity	Wm^{-2}
R_s	Reflection coefficient	
E_r	Electric field of reflected light	NC^{-1}
E_i	Electric field of incident light	NC^{-1}
n_1	Refractive index of material	
n_2	Refractive index of atmosphere	
θ_i	Incidence angle	Degree
θ_t	Transmittance angle	Degree
T_s	Transmission coefficient of S-polarization	
T_p	Transmission coefficient of P-polarization	
n	Refractive index	
c	Speed of light in vacuum	ms^{-1}
v	Speed of light in medium	ms^{-1}
R	Reflectivity	
k	Extinction coefficient	
α	Absorption coefficient	cm^{-1}
λ	Wavelength	nm
d(F)	Ablation rate	nm per pulse
α_{eff}	Effective absorption coefficient	cm^{-1}

F	Laser fluence	$mJcm^{-2}$
F_{th}	Ablation threshold fluence	$mJcm^{-2}$
Δh	Thickness of layer ablation per pulse	nm per pulse
I_{α}	Optical penetration depth	cm
I_T	Thermal penetration depth	cm
V	Velocity of removal material	ms^{-1}
ΔE	Energy of bond breaking	mJ
T_s	Temperature of surface	K
m	Diffraction order	
M	Groove intensity	Grooves mm^{-1}
θ_i	Incidence angle	degree
θ_m	Diffracted angle	degree
G	Groove frequency	mm^{-1}
Λ	Grating period	nm
q	Heat flow	W
D_s	Thermal conductivity	$Wm^{-1}K^{-1}$
ρ	Density	Kgm^{-3}
c_p	Heat capacity	$JKg^{-1}K^{-1}$
τ_{th}	Thermal relaxation time	s
χ	Thermal diffusivity	m^2s^{-1}
ϕ	Velocity potential	
P	Pressure	Pa
β	Volume expansion coefficient	K^{-1}
A	Absorptivity	
R	Optical reflectivity	

Γ	Gruneisen coefficient	
$Z_{air,chitosan}$	Acoustic impedance of air and chitosan	Pa s m^{-3}
c_s	Acoustic velocity	ms^{-1}
τ_p	Laser pulse duration	ns
X	Degree of decomposition	degree
W_0	Initial mass of material	gm
W_f	Final mass of material	gm
E_a	Activation energy	mJ
E_g	Band gap energy	eV

Table of Contents

List of tables

List of figures

CHAPTER 1.

Introduction to laser ablation of polymers

1.1. Introduction and motivation

In recent years, biocompatible polymer materials have been intensively investigated as a novel type of intelligent material for Lab on Chip (LOC) applications, biomedical and biochemical fields. Microfabrication and photolithography have contributed an important role in most of these applications. Diffraction grating sensors have been fabricated using different methods, including soft lithographic techniques, Laser Direct Writing (LDW), nanoimprinting, photolithography, micro imprinting lithography and e-beam lithography. Laser processing is an alternative method that has been used to process, pattern and modify biocompatible polymers. Laser ablation has been used extensively for material processing [1,2], specifically chitosan [3–6] and other bio-polymers [7].

A wide range of laser wavelengths have been exploited for the fabrication purposes. A KrF 248 nm laser was used to generate a submicron grating in fused silica and polyimide [8,9] this has been utilised for the fabrication of microfluidics devices [2]. A laser emitted at a wavelength of 488 nm has been used to produce a surface relief grating on an epoxy based polymer [10]. An excimer laser emitted at a 193 nm wavelength has been employed previously to pattern a surface grating in a period of Λ=500 nm on borosilicate glass [11]. In addition, a CO_2 laser operating at 1064 nm was used to fabricate a long period grating on optical fibres [12]. Different laser wavelengths have also been used to process a biocompatible material [13,14]. Biocompatibility of biopolymers is one of their most important characteristics which allows them to be used in a wide range of applications including; biological systems, optical devices, biomedical and pharmaceutical

applications. Biocompatibility can be defined as “the ability of a material to perform with an appropriate host response in a specific application” [15] or in another words, the biocompatibility means that the biocompatible materials should fulfil their function when used for bio-applications without initiating undesirable effects. Chitosan is one of the most valuable biopolymers which has received a great deal of interest for its biomedical applications, including lab on chip (LOC) and its use as a bio-sensor.

Different reasons dictated the choice of chitosan; first, the excellent compatibility of it has been shown to be concordant with several other studies. These such works stated it to be a good choice for drug delivery and biological sensing. Secondly, crosslinked chitosan hydrogels are currently been explored for their potential usage in tissue engineering. Finally, other unique properties of chitosan are that it antimicrobial, biodegradable, not harmful to the environment and as an anti-tumor treatment. These make it an attractive biopolymer for biomedical and pharmaceutical applications listed above.

Chitosan has an active surface that is suitable for photochemical reactions; this surface has considerable importance for these reactions because it has amine (NH_2) groups. These groups give the chitosan films their unique properties, these allow it to be suitable for many reactions including biological reactions that occur on the chitosan surface. Agarose is another biocompatible material that has been widely used in research applications due to it is unique properties. In this case it is a non-toxic and a hydrophilic gel type material. An agarose film has been utilised for pH optical sensors [16], 3-dimensional micropatterning for cell cultures [17] and humidity sensors [18]. Forming a grating structure on the 5CB LC doped with the biocompatible material chitosan is also aimed in

the thesis because of their properties such as electro-optical effects allowed them to be use in wide range of applications.

The thesis is subdivided into eight main chapters and they can be described as follows:
Chapter 1: The main objectives presented in this chapter are: an overview of laser ablation in general and a brief synopsis of the advantages of using laser ablation to process these materials. An introduction for laser ablation processing of biocompatible materials is also presented. Various techniques to process the surface modification for applications are discussed. Furthermore, the main techniques of focus are Laser Direct Writing (LDW) and nanoimprinting methods to fabricate the diffraction grating on the biocompatible materials used for this project. The motivation for this work is presented, highlighting the importance of biopolymers to enhance and further many research fields. Moreover, it takes into consideration that biocompatible materials are valuable materials for their use in biological systems, tissue engineering and optical applications. This is due to their ability to be used as an appropriate host response. Additionally, the possibilities of using different techniques to fabricate the grating structure on the biocompatible materials films to be used for optical applications. This research particularly aims at understanding the interaction of an ArF 193 nm excimer laser with biocompatible materials at a wide range of laser fluences and the fabrication of diffraction gratings on thin films. The understanding of the electro optic effect of 5CB LC doped chitosan and how it is employed to tune a grating using a HeNe laser 632.8 nm wavelength is also studied.

Topics related to the laser processing of biocompatible materials including ablation processing and fabrication using excimer lasers are presented. Various applications of using biocompatible materials such as chitosan and agarose are briefly discussed.

Chapter 2: The main topic presented in this chapter is the light matter interaction. In the beginning, it is introduced that light interacts with materials in different ways; absorption, transmission and reflection. The principle behind excimer lasers is also presented as well as a discussion on the interaction between the laser light and materials in terms of ablation processing. Laser ablation mechanism, such as photothermal, photochemical and photoacoustic mechanisms are conversed in detail.

Chapter 3: This chapter provides a background for theory of diffraction grating including the equation. This is followed by the specifications of the diffraction grating such as the resolution, efficiency and dispersion. Types of diffraction grating, phase and amplitude grating are conferred. Applications of diffraction gratings such as grating couplers and waveguides are presented.

Chapter 4: The experimental methodologies are presented in this chapter. The experimental procedures of producing solutions as well as film preparations including spin coating and the ablation process, are described.

Chapter 5: This chapter involves the results of laser ablation, temperature rise modelling and generating a diffraction grating. This begins by introducing the heat transfer mechanisms including conduction, convection and radiation. The COMSOL^{TM} software that was used to simulate the temperature of the biocompatible materials irradiated with the excimer laser is shown. The heat equation is discussed followed by the processed results from the temperature rise simulation of chitosan. The laser ablation of biocompatible materials is presented in this chapter. Two materials, chitosan and agarose, were treated with the excimer laser ArF 193nm laser. The characterisation of the laser beam of 193 nm is also considered. A characterisation and laser ablation of chitosan film

is presented. A laser ablation of the chitosan film is analysed in terms of the photoacoustic mechanism. The surface morphology of films before and after irradiated by laser is also processed. Laser ablation using mask projection and nanoimprinting techniques used to produce a diffraction grating on biocompatible materials films. This chapter involves patterning the structure of the two biocompatible material films, chitosan and agarose using a 193 nm laser. A method of forming the cross grating structure on films is described, and the results are analysed. Also, the electro-optic effect and the materials used to investigate the electro optics effect on 5CB LC and 5CB LC doped chitosan are presented in this chapter. The charactrisation of 5CB LC doped chitosan using a UV-VIS spectrophotometer and AFM are investigated. Finally, producing a 5CB LC doped chitosan cell to tune the electro optical diffraction grating on it is introduced and discussed.

The conclusion of the project is presented.

Chapter 6: This contains potential future works to advance the project.

1.2. Excimer laser ablation

In the last few decades, excimer laser ablation has been a hot topic that has attracted interest from many researcher groups due to it is ability to produce very accurate microstructures in a wide range of material types. This has advantages over other chemical or mechanical processes as laser ablation is a dry process that eliminates several processing steps. Furthermore, a large amount of energy can be accurately delivered by laser into specific regions of a material to create the desired response, the rate of energy can also be controlled. Laser ablation is applicable in a wide range of applications for example thin film deposition, surface modification, lab on chip (LOC) fabrication, nanomaterial synthesis, medical and biological applications. A variety of parameters play

a significant role in the process of laser ablation, these include laser wavelength, pulse duration, pulse repetition frequency, laser irradiance and laser fluence. Others involve optics parameters, such as the focal length and numerical aperture of the lens used to focus the light and the demagnification when in imaging systems, which is very important in the ablation processing.

Principally, the ablation characteristics are transcribed by the interaction between the laser and material as well as the laser parameters mentioned above. Laser ablation is one of the standard methods for the surface modification of materials. Laser surface modifications have been widely reported for biopolymers to improve their performance in a physiological environment [19]. Surface modifications offer an opportunity to modify the physiological and physical properties to be used for specific applications [20–22]. Natural polymers can be found in three categories; proteins in the form of (collagin, actin, gelatin, silk and keratin), polynucleotides in the form of Deoxyribonucleic Acid (DNA) and Ribonucleic Acid (RNA) and polysaccharides in the form of (cellulose, amylose, chitin and dextran) [23,24].

Hence, surface modification of biomaterials is an attractive method that has been widely used to improve the mechanical properties, tribological [25] and device multifunctionality [26]. Surface modification is also used to improve the biocompatibility of a polymeric scaffold [27,28]. Different laser types; Argon Fluoride (ArF) 193nm and Krypton Fluoride (KrF) 248nm excimer lasers have been used to study the effect that different wavelengths have on the surface morphology of biocompatible materials [29,30].

Moreover, many studies have illustrated that the ablation of biocompatible materials using UV lasers causes the breakup and spontaneous destruction of materials from the solid surface by the process of photodecomposition ablation [31,32]. In addition, ablation

of biocompatible materials consists of a cavitation phenomenon which causes foaming as a result of extremely high pressure, photothermal, photodecomposition and photoacoustic mechanisms [33]. Usually, the foaming formation during the ablation process of biopolymers is caused by the UV irradiation [34–36]. However, an ArF excimer laser has been previously used to remove the corneal tissue without damaging the overall structure. This ablation process is due to the photoablation mechanism and is non-thermal because of the high absorption coefficient of corneal tissue at 193nm [37,38].

A variety of parameters, such as the absorptivity, reflectivity, acoustic velocity and the thermal expansion, are playing an important role in fulfilling the conditions of the ablation processing of materials. In addition, for polymers, the bond breaking can occur before the removal of the material. Therefore, two ablation mechanisms, photothermal and photochemical, were considered for polymer ablation using 193nm and 248nm wavelength lasers sources [39].

Although, laser ablation has been used to modify the surface morphology, it is also used to realise patterns for various applications. Microelectronic circuits by definition require a small structure and devices that can be patterned on a surface in a controllable and repeatable. Therefore, a photolithography technique using an ArF laser was employed to produce a circuit at the critical dimension of 0.1μm [40]. Laser ablation has been widely used to fabricate diffraction gratings for the realisation of Distributed Feedback lasers (DFB) [41] and grating coupler devices [42]. A variety of techniques have been developed to generate diffraction gratings with high resolution on a nanometer or a micrometer scale; mechanical scribing [43], dip pen lithography [44], 3D printing [45], micro-contact printing [46,47], holography[10] and laser ablation [48–50].

The high flexibility of the ablation process makes it beneficial for employment in these fields, as well as the ability for the microchannels to be produced very rapidly. In this work the laser beam delivery system was designed to be used with the ArF laser, emitting a wavelength of 193nm. In this thesis, the surface morphology of biocompatible material is explored before and after laser irradiation. In addition, the surface relief grating on biocompatible materials films supported by substrate is formed by a Laser Direct Writing (LDW) method using a mask projection technique. Two biocompatible materials (chitosan and agarose) were chosen for laser processing and fabrication diffraction grating to be employed for their optical applications.

The reason for choosing a fabrication diffraction grating is because it has been used in a wide range of optical applications, such as optical communications, integrated optical devices and lasers. Choosing the grating period is a very important part in designing many applications. The diffraction grating is fabricated by using two different techniques: nanoimprinting lithography and Laser Direct Writing (LDW). The (LDW) technique offers flexibility for quick prototyping. Generally, " direct-write processing refers to any technique that can create a pattern on a surface or volume in a serial or spot-by-spot fashion [51]. Three important aspects are considered for the LDW systems: laser source, the beam delivery system and the targets. The laser source is considered as the most important part of the LDW system because the interaction between the materials of interest with the laser needs to be taken into consideration.

Liquid Crystal (LC) doped biocompatible materials have been used in this work to investigate their effect on the production of grating. The capability of Polymer Dispersed Liquid Crystal (PDLC) as a composite material make them a valuable platform for various applications such as glasses with controllable transparency, display devices, optical

fibres, electro-optics devices and visual projection [52,53]. The ability of PDLCs to transmit the light under an external electric field is essential to be used for these applications, otherwise in a common state they become opaque. Several advantages for utilising PDLCs are the flexibility due to the polymer matrix, mechanical strength, high contrast, brightness and simpler fabrication [54]. Using PDLCs in applications improve the lifetime of the devices when at high temperature and high humidity. The composite materials also provide a cost reduction, as well as increasing the ratio of contrast, time of responding and transmittance [55,56].

Nowadays, nematic Liquid Crystal Displays (LCDs), pioneered at the University of Hull became an essential material in modern electro-optical technologies. For photorefractive materials low powered lasers are used to process the optical information. Instead of using a very high voltage cross the crystal a few volts can be used to induce the photorefractive grating in these materials [57,58]. Moreover, Polymer Dispersed Liquid Crystals (PDLCs) are an attractive materials and have been widely explored for numerous applications because of their electro-optic properties and light scattering capabilities [59,60].

In this thesis, an electro-optic material, 5CB liquid crystal doped chitosan was used to tune the gratings. 5CB is one of the most important liquid crystal materials because of its unique properties. Chitosan was chosen to be doped with 5CB due to its compatibility [10]. The main objectives of this thesis is to characterise the biocompatible surfaces and to develop the range of micro-patterns generated in the biocompatible films containing chitosan, agarose and silk fibroin. There is a growing demand for these materials to be used in areas such an optical devices, waveguides and grating couplers. Further, in this thesis the effect of electric fields on 5CB LC doped chitosan targets is studied. The aim

is to better understand the role of an applied electric field in the grating fabrication on the 5CB LC doped chitosan.

The laser ablation technique has been widely used for biocompatible material surface modification [61] and biomedical applications [62]. Two bio-compatible polymers (poly-l-lactide and poly hydroxybutyrate) were treated with ArF and KrF excimer lasers, and both were used in the medical and pharmaceutical fields [29]. A XeCl excimer laser emitting at a 308nm wavelength was used to investigate a photo-acoustic mechanism during laser ablation of biocompatible polytetrafluoroethylene (PTFE) [32] as well as the PTFE film behavior during ablation processing [63]. Surface modification of two biocompatible types (poly-l-lactide and poly hydroxybutyrate) were investigated using a different excimer laser KrF and ArF [29]. A study of surface properties of different biopolymers; collagen/polyvinyl pyrrolidone (PVP) and chitosan films was carried out after irradiation with KrF excimer lasers emitted at wavelengths of 248 nm and 254 nm [3,30].

The interaction of different laser wavelengths (532 nm, 595 nm and 1064 nm) with a biocompatible material and tissue was investigated [64]. A photoacoustic signal was observed in the laser ablation of polytetrafluoroethylene (PTFE) biocompatible using a XeCl excimer laser emitting a wavelength of 308 nm with 17 ns pulse duration [32]. This study has been reported that under ablation threshold fluence there is no signs of physical fractures meanwhile mechanical damage was very evident above the threshold fluence. An ArF excimer laser 193 nm was used to process the collagen and a photochemical reaction was seen to taken place during the ablation processing [65]. Silk fibroin and other biopolymers have been treated with two different types of lasers, first the ultraviolet laser KrF 248 nm and the femtosecond laser Yb:KGW [66]. A foaming formation was detected

on a silk fibroin film caused by UV irradiation above the ablation threshold. The surface morphology of poly-l-lactic-acid (PLLA) has been investigated using KrF 248 nm excimer laser [67]. A range of laser fluence and different numbers of laser pulses were applied to modify the surface. An increase in surface roughnesses was observed as well as changes in the surface morphology induced by the laser treating.

Relatively recently, the diffraction gratings have received a lot of attention from researchers. This attention is because the diffraction gratings can be used across different fields to analyse the light spectrum as well as many other applications associated with this. In regards to the importance of diffraction gratings, G. R. Harrison stated:
"It is difficult to point to another single device that has brought more important experimental information to every field of science than the diffraction grating. The physicist, the astronomer, the chemist, the biologist, the metallurgist, all use it as a routine tool of unsurpassed accuracy and precision, as a detector of atomic species to determine the characteristics of heavenly bodies and the presence of atmospheres in the planets, to study the structures of molecules and atoms, and to obtain a thousand and one items of information without which modern science would be greatly handicapped." [68].

From the past when the first diffraction grating was produced until now, they have been widely used in different applications such as; optical communications, biomedical sensors, grating coupler devices, chemical sensors, integrated optics devices and producing distributed feedback lasers (DFB). Moreover, Nano- and micro-patterned surfaces of polymeric components and devices play a main role in information and communication technology. For instance, nano- and micro-structured components are recently used in cell adhesion, biological and, security applications as well as the microstructure devices perform a wide range of optical and opto-electronic functions

[61,69–71]. We, as researchers are interested in the fabrication of diffraction grating made of biocompatible materials films and PDLCs, this will be the main subject of this thesis. The LDW technique was used to fabricate a microstructure on polymer scaffolds for a tissue engineering applications [72], the femtosecond Yb: KGW laser emitted at a wavelength of 515 nm was used as light source for the fabrication process. A surface relief grating was used to produce a grating coupler device and humidity sensing [73]. It has been reported that a grating generated on a SiO_2/TiO_2 waveguide that has a grating period of 1.2 μm, exhibits very high sensitivity of sensor applications used to theoretically determine surface and volume adsorption. Also, the mechanisms of the adsorption were determined from the measurements of the changes in the effective refractive index.

For coupling light from one waveguide to another, two grating couplers can be used [74]. It was reported that there is a possibility to couple light between two waveguides when a large distance separates them. The photonic bandgap structure was employed to improve the performance of the coupling device. It has been proposed that this type of coupling when a simple connection between them is not possible. Optical Waveguide Light mode Spectroscopy (OWLS) [75] was employed to investigate the interaction between molecules adsorbed to a surface. They reported that OWLS are classified as an effective technique to monitor protein adsorption and cell attachment, additionally the spreading processes were quantitatively monitored. The high efficiency of grating couplers is desired to provide strong light coupling into the waveguide. Therefore a short grating of 10 mm long was designed to butt-couple the light into fibre [76]. GaAs was used as a substrate in the design of an out of plane grating coupler, where the grating was fabricated on it by the electron beam lithography. It has been stated that the light coupling could be achieved for incident light ray, normal to the surface when the grating period is equal to the wavelength dividing by an effective refractive index. A wavelength of 1550 nm has

been used, presenting a coupling efficiency of 19 %. As the grating structure plays an important role for integrated optics, combining a rectangle grating shape in the period of 287 nm and 133 nm depth, in conjunction with a multilayer substrate reflector. This was used for the design of a grating outcoupled with a high directionally [77]. Different duty cycles of the grating (33, 37, 43 and 60 %) were utilised for the device structure to control the radiation factor in the air due to the high reflectivity of the multilayer surface. The reflectivity of the multilayer depends on the refractive index of the material and the grating period. A grating coupler device to couple light into a waveguide was demonstrated. The effects of the grating at the highest output for the grating coupler's efficiency were assessed [78]. The grating period of 400 nm was fabricated onto the uni-bond Silicon on Insulator (SOI) to be used as a grating coupling device and to achieve mode matching. Coupling efficiencies of 70 %, 60 %, 54 % and 30 % output were achieved with the grating height of 140 nm, 440 nm, 30 nm and 230 nm respectively.

A double grating structure was proposed to be a compact grating coupler device [79]. This type of structure was used to couple the light between two different SOI waveguides. Double layers of Si in thickness of 230 nm and 250 nm were used as a waveguide, and these thicknesses allow the system to operate in a single mode at a 1550 nm wavelength. The effects of the grating period and the grating depth were studied, this proved an efficiency of 22 % where the coupling was measured with the grating length to be 12.9 μm. Free space optical coupling grating to grating was demonstrated by fabricating the grating on an independent substrate [80]. A volume grating with width of 10 mm fabricated on the substrate was utilised to diffract light into the second grating, which was positioned onto the first one. The coupling efficiency reported between the nonoptimised, nonfocusing and unpatterned volume grating is 31%. One of the important conditions addressed by a free space grating coupler is the increase in the grating volume. Some of

the challenges associated with this are power loss and a high integrating density of components in the optical circuits. Therefore, a grating with double surface corrugation was used in the design of the a high-performance grating coupler devices to couple light into an optical waveguide [81]. The surface relief grating was patterned on the substrate by an ion milling technique to get a grating period of Λ= 347 nm with the depth of 74 nm, where the duty cycle was 50%. Beyond this, 74 % and 98 % input coupling efficiencies have also been measured. One of the significant challenges for photonic circuits is how to couple light between the single optical fibre and a nanophotonic waveguide. A grating structure with a period of Λ= 400 nm was produced onto a high refractive index material, Silicon-On-Insulator SOI wafer with a thickness of 200 nm using a UV-lithography 248 nm excimer laser to produce a grating coupler device [82]. In this structure, to avoid the reflected light due to the second order diffraction, a coupling at 10 degrees was chosen, where a 30 % coupling efficiency was measured with a 1dB bandwidth. A formula method was used to design the grating coupler device to couple light between the single-mode fibre and SOI waveguide [83]. With this method, a coupling efficiency of 78.5 % was achieved at a wavelength of 1551 nm and with a bandwidth of 3 dB.

For a grating coupler with a double-etched apodized waveguide has been previously designed to achieve a high coupling efficiency [84]. A grating with a period of Λ= 610 nm on a SOI wafer with a thickness of 340 nm was produced by utilising COMS technology, the grating was defined by deep UV photolithography. A coupling loss of -1.5 dB was measured at a wavelength of 1560 nm with a 3 dB bandwidth of 54 nm. The grating coupler structure used to couple light between a SOI and a single-mode fibre was presented [85]. A different wavelength was used to measure the Coupling Efficiency (CE). The highest CE obtained was 47.2 % at a wavelength of 1562 nm for a 340 nm

grating period by using a flat optical fibre with a tilted angle of 8.5 degrees. The effect of detuning on a grating coupler's efficiency was investigated [86]. Different grating periodicities detuned from -2.5 nm to -15 nm and +2.5 nm were studied from a 295nm resonance periodicity, where a high emission surface efficiency of 60% was measured.
A grating coupler device was designed to couple light between horizontal slot waveguides and single mode optical fibre [87]. A horizontal slot waveguide is considered a capable configuration for nonlinear applications of silicon based photonics. Grating periods of Λ= 807 nm and Λ= 670 nm for positive and positive detuned respectively were studied. The study showed high coupling efficiencies of 32% and 47% for positive and negative detuned system.

A Long period grating was fabricated on chitosan-coated fiber optics to be used as a biosensor [88,89]. The grating period of 435 nm patterned using the point by point writing method with a KrF excimer laser emitted a wavelength of 248 nm. This type of sensor was employed to detect the concentration of cholesterol in the range of 5.025 pm/ppm. Chitosan is receiving a great deal of scientific interest as a bio-compatible material for a wide range of applications [90]. It is a natural polymer (polysaccharide) prepared from chitin by deacetylation. The ability of chitosan to be spun to make bio-compatible thins films is a useful property. It is a material that has many medical and pharmaceutical applications; for example, as a substitute for artificial skin [91], bandages, contact lenses [92], drug delivery vehicles [93] and surgical sutures [94,95]. Chitosan waveguides are used to route light around LOC architectures [96]. Chitosan biocompatible material were used in the configuration of Fabry-Perot interferometry to be used for humidity sensors [97]. It was reported that the sensor operates in the range of 20% RH to 95% RH with a response time of 380 ms. Bragg gratings were fabricated using the nanoimprinting technique on the mixing biocompatible gelatin and chitosan film for biopolymeric optical

planar waveguides [98]. Devices of polymer waveguides are of interest for many research groups [99,100], they have accomplished their work by utilising direct writing by electron beam lithography to synthesis a grating required to produce grating coupler devices for strip waveguide and polymer slaps. The study presented a coupling efficiency of 67 %. The biocompatible hydrophilic chitosan film was used in the design of the waveguide layer to be used as an optical waveguide sensor at a relative high humidity [101]. The study showed a high sensitivity of 0.09 ppm with a low response time of 0.3 min. An agarose hydrogel film was used in the fabrication of optical device to be used for biological applications [102]. The device was used to encapsulate a biological cell inside an optical waveguide, and the study showed a good interaction between the light and cells.

In the last few years, vast attention has been given to Polymer Dispersed Liquid Crystals (PDLCs) as valuable materials as droplets of a liquid crystal suspension will disperse in a polymeric matrix with a low molecular weight. PDLCs have been used in electro-optics and other optical based applications due to their physical properties, for example, PDLCs have been used for visual displays [103]. Holographic transmissions and reflection gratings have been formed on the PDLC [104]. In this study, the electro-optical effect of a holographic transmittance grating has been investigated. A holographic grating with a density of 3000 line/mm was achieved using HeNe laser on various photopolymer films [105], the sensitivity of the diffraction grating was debated. A refractive index grating using a HeNe laser was formed on the nematic liquid crystal 5CB doped with Sudan Black B (SBB) dye. This presented five diffraction orders [106]. A quasi-permanent grating in the photorefractive nematic liquid crystal, 5CB doped with a fullerene (C_{60}) has been successfully formed using Ar laser [107]. Diffraction gratings made from the nematic liquid crystal 5CB, doped with a norland polymer using a HeNe

laser has been reported [108]. In this study, an electro-optic effect of the grating was investigated. A holographic grating with a period of 36 µm has been fabricated using different lasers such as the HeNe and Ar these were processed on PDLCs such as ,5CB, K15, (Merck), dipentaerythritol pentaacrylate (DPPA, Polysciences), and RB [109]. The study showed that the grating made by the HeNe laser was superior to the one made by an Ar laser.

1.2.1. Laser Ablation Patterning using mask projection

The procedures of surface modification of different materials have been widely investigated for several biomedical application [110–112] such as tissue engineering [113], biosensor [114]. Producing microstructures on the surface of different materials has received a high interest because of the tribological alteration material properties; for example, wettability [115–117] and surface adhesion [118].

Recently, a surface modification with a microstructure constructed on either assembling or patterning has been utilized for a wide range of applications; diffraction grating [119], chemical sensor [120] and optical components [121,122]. Therefore, different techniques such as chemical etching [123] photolithography [122] and laser ablation [124] have been suggested for microstructure fabrication. The laser ablation technique is the most efficient technique because it is fast, non-contact and provides more flexibility. The ablation processing was discussed with more details in Chapter 3 and the laser ablation of biocompatible materials in Chapter 6. The imperative type of laser used to fabricate microstructures is the excimer laser. This type of lasers are heavily used for producing complex microstructures and different features such as ramps, micro-channels [125] and sub-micron holes [126]. In addition, using excimer lasers for microstructure patterns has several advantages [127]:

1- The energy is delivered with high resolution and precise directionality.

2- The Heat Affected Zone (HAZ) is small.

3- High speed processing.

4- The ablated depth can be controlled.

5- Offers a short time (~20-40) ns for the material interaction.

6- A wide range of material can be processed.

All the above advantages make the fabrication of microstructure on different materials very effective with no comparison to any other technique.

1.2.2. Grating with imprinting method

The Nano-imprint lithography (NIL) is one of the lithography techniques consisting of a micro or a nano structure patterns with a template. The patterns is transferred to the material surface with high resolution to be used for different applications. The Nano-imprint lithography method is completely well-matched to the standard techniques of the micro-fabrication including the transfer processes such as lift-off and etching [128]. Different techniques including; Nano-imprint lithography (NIL) [129], dip-pen lithography [130,131], Micro-contact printing [132], the atomic force microscope lithography [133–135], hot embossing [136] and UV based Nano-imprinting lithography [137,138] have been used for the Nano-imprinting lithography .

The NIL is widely used and has attracted attention of the researchers because the high resolutions that can be achieved with it. In addition. The NIL is considered as high-throughput capability and a very low cost method because of the simple equipment used in the process. Figure (1-1) below shows schematic of the NIL method was used to imprint 10 nm hole array in poly(methyl methacrylate) (PMMA) [139].

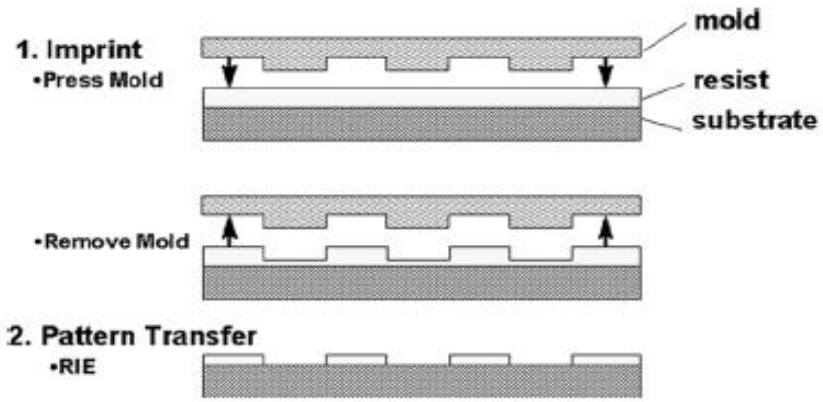

Figure 1-1: The schematic of nano-imprinting method was used to imprint 10 nm feature size [139].

It is important to know that choosing between these techniques depends on the material, the density of the features [140] and the feature size are required for specific application [141]. As well as a grating structure in large area can be easily produced with the NIL. Moreover, each technique has a specific processing for example, hot embossing needs a high temperature and a high force of contact [136] while in the UV based lithography uses the curing with UV-light exposure for the imprinting [138].

Recently, structure in nano scale features are required for a wide range of applications such as waveguide for optical components [142], biological [143], tissue engineering and bio-sensing [144] and nano-photonics [145].

Generally, NIL technique has involved three steps; firstly, the original master mold defines structures, secondly, the duplication of mold and the third one is the imprinting processing [145]. The simplification of patterning and functionalization are advantages of using polymers in various fields [146]. These processes such Nano-imprinting are much easier with using biopolymers such as silk with low temperature and low pressure [147].

Nano-imprinting lithography techniques have been used to duplicate a nano-structure into biopolymer materials but with limitations such as the range of temperature and the pressure [148]. Silk fibroin is an attractive biopolymer because of it is biocompatibility, optical and mechanical properties [149]. Nano structure in density of 3600 grooves.mm^{-1} was imprinted into a cast film of silk fibroin at room temperature [148]. As well as a periodic square patterns of holes in diameter of 100 nm was transferred into a silk film [150] NIL technique was employed to imprint, three dimensional structure patterns into different functional materials [151] and sub-100nm patterns into protein [152]. Chitosan is one of the important biocompatible material was fabricated using NIL technique. Different micro and nano structure such as microscale, nano wire and nano dot performed on the chitosan films were reported for bionanotechnology applications [153]. Agarose is another biocompatible material has been given big attention to be used for different applications. For example, agarose was used in the application to the design of biomolecular micro patterns [154]. Biocompatible agarose was used as a universal carrier to transfer the biomolecules in the viscus fluid matrix using a dip-pen nanolithography (DPN) [155]. Micro casting is another technique used for cell patterning with agarose [156].

1.3. Electro-Optics effect

Several years ago, it was proposed to use an organic electro-optic material for the electro-optical applications. Since then various devices have been introduced but a few of them were investigated for their electro-optic response [157]. Recently, electro-optic polymers show some advantages such as; producing a high performance, and low manufacture cost. Examples of uses for these materials are, as an electro-optic modulator, a variable optical attenuator or as a tunable filter [158]. These advantages allow these materials to be used in various optical devices applications such as; communication [159], optical sensing

[160], analogue and digital signal processing and information processing. Changing the optical properties by controlling the applied voltage is the main idea of the electro-optics devices [161]. The optical properties of such materials are; the permittivity tensor and the refractive index vary. This means that they modify some of the light features such as phase, amplitude and frequency when the light wave propagates through the electro-optic devices. Waveguide devices are another application for utilising the electro-optic field [162]. This type of devices based on the non-linear polymers have a high performance and potential with a high speed of signal processing and communication system. The multilayer structure of thin film can be used to produce polymeric optical devices, this is achieved by starting with a substrate such as glass, silicon or an upper electrode containing precious metals such as silver and gold.

Additionally, a lower cladding and the central waveguide layer. However, in this study, the electro-optical effect of a PDLC 5CB doped with chitosan and PDLC doped with dye has been investigated. This effect has been employed for realising an electro optic diffraction grating of PDLC (5CB doped with chitosan) doped with SBB dye. Switchable holographic grating made of Polymer Dispersed liquid crystals (H-PDLCs) has been formed by using Argon laser emitting at a wavelength of 532 nm [163]. This reported different grating periods made of solid films of PDLC and ±1 diffraction order was monitored. Holographic transmissions and reflection gratings have been formed on the PDLC [104]. A HeNe laser has been used to fabricate a phase holograms on several photopolymers and 3000 line mm^{-1} was achieved [105] also, the sensitivity of the diffraction grating was debated. Also, HeNe laser was employed to form a refractive index grating on the nematic liquid crystal 5CB doped with Sudan Black B (SBB) dye and five diffraction orders were presented [106]. A photorefractive nematic liquid crystal, 5CB doped with a fullerene (C_{60}) has been used to fabricate a quasi-permanent grating

using Ar laser [107]. Furthermore, diffraction gratings made from the nematic liquid crystal 5CB, doped with a norland polymer using a HeNe laser has been reported [108]. A polarisation grating has been created of nematic LC E7 doped with azo dye using holographic setup with CW Ar laser operating at 488 nm wavelength [164]. The grating period of 15 µm has been reported. A diode-pumped-solid-state (DPSS) laser operating at a wavelength of 532 nm was used to generate a diffraction grating on a film of LC E7 doped m with methyl red (MR) dye [165]. The effect of the writing beam ratio of the diffraction efficiency has been investigated. An example of grating device is shown in figure (1-2):

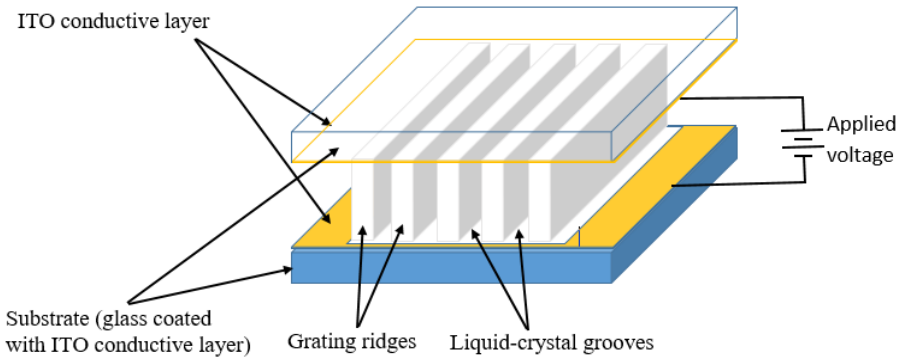

Figure 1-2: Schematic of the optical grating devices structure based on the liquid crystal [166].

In addition, liquid crystals in a nematic phase (NLCs) exhibit an electric field effect on their optical properties [167]. The first experiment in this field was examined by William [168]. LCs show three phases changes known as the; smectic A, nematic and finally the isotropic phase [169] as indicated in figure (1-3). It can be noticed that the LC phase changes with increase in the temperature: some of the matrix at low temperature exhibit a nematic and others Smectic A, while exhibiting an isotropic phase at high temperature.

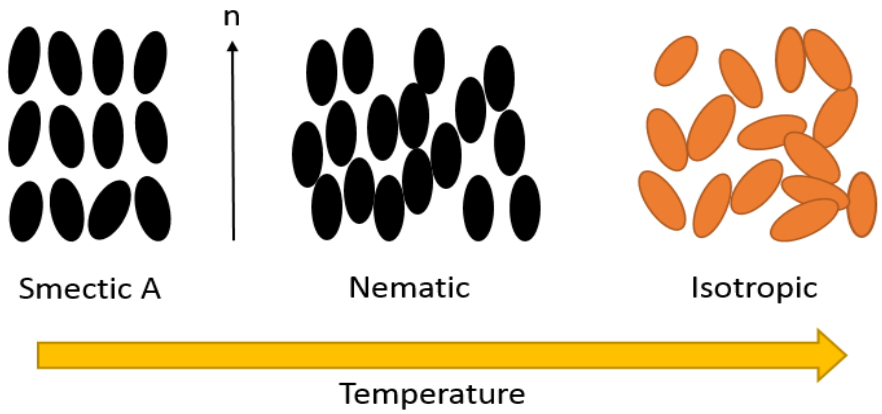

Figure 1-3: The picture of the liquid crystal phases showing the orientation order in the Smectic A, Nematic and isotropic phases [169].

The William Domain (WD) effect on the (NLC) appears when increasing the applied voltage but the frequency is lower than the critical value f_c = 168 Hz [167]. Moreover, Mayer and Helfrich explained the appearance of William domain in the high and low frequency respectively [170,171]. The NLC shows this effect at a critical voltage of U_c= 22.05 V [167]. While, the WD pattern starts to fluctuate and change the state , this is called dynamic scattering mode as the voltages exceed the critical voltage value [172].

A liquid crystal materials that has drawn a great attention is the 5CB (4-n-pentyl-40 – cyanobipheny). The simple molecular structure of 5CB undergoes a nematic phase transition at room temperature [173]. Figure (1-4) shows the chemical structure of the 5CB LC. This property allows it to be used for physical behavior investigations for a simple nematic material [174]. The 5CB liquid crystal has offered excellent physical and chemical properties such as chemical stability, stable mesophases, optical anisotropy and high dielectric properties. However, the absorption of the visible light range is weak [58]. The properties of the thermotropic liquid crystal 5CB makes it suitable for a wide range of applications such as optoelectronics [175], storage technologies [176,177] and for visual displays [168].

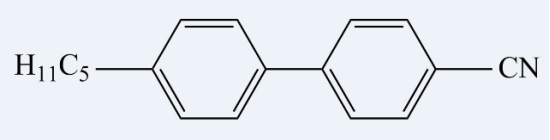

Figure 1-4: The chemical structure of 5CB liquid crystal produced by using chem. office.

The optical properties of 5CB LC are show in table (1-1) below:

Table 1-1: The optical properties of 5CB liquid crystal

Properties	Value	Reference
Heat capacity (c_p)	2 $Jg^{-1}K^{-1}$	[178]
Density (ρ)	10 gm^{-3}	[178]
Thermal diffusion coefficient	1.8×10-3 m^2s^{-1}	[178]
Elastic constant (K)	6×10-12 N	[179]
Dielectric constant ($\Delta\varepsilon$)	13.15	[180]
Transition temperature	(35-35.1)°C	[178]
Birefringence (Δn)	0.1788	[181]

For simplification the elastic constants of 5CB; $K_{11} = K_{22} = K_{33} = K$ is used. These values are justified to be equally are rather close to each other but they for thermotropic [179].

In the last few years, much interest has been given to polymer dispersed liquid crystals (PDLCs) films. These films are composed of liquid crystal microdroplets of dispersed within the polymer matrix [182]. The PDLCs offer controllable optical properties when utilising an electric field. By varying the electric field strength, there are noticeable changes to the light scattering properties as the composite changes to a transparent [183]. A wide range of applications have been used for PDLCs such as a holographic grating light window, switchable displays and as a Variable Optical Attenuator (VOA) [105,163,184]. Moreover, liquid crystals doped with dyes have also welcomed much attention from research groups. The modification of non-linear optical properties of the liquid crystals is the most important effect of dye molecules on the LC [185]. Various

parameters are affected the non-linear optical behavior of dye doped liquid crystals such as dye concentration, temperature, intensity and the wavelength of the laser used [186]. One of the dyes widely used when doping LCs is an azo-dye, Sudan Black B (SBB), this dye is used in for this work.

In 1934, Lison introduced the Sudan Black B (SBB) azo-dye as a specific lipid stain [187]. According to Lison, Lipids which have a biological origin can be used to dissolve the Sudan Black B dye. In addition, different solvents have been used to dissolve SBB such as acetone- alcohol, propylene glycol, ethylalcohol, and ethylene glycol. The chemical structure of the SBB dye is shown in figure(1-5) [185]. Some of the advantages of using the SBB dye are the high stability and a high dichroic ratio because of the rod-like molecular shape of it.

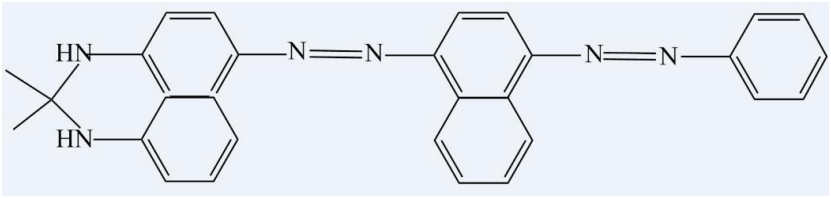

Figure 1-5: The chemical structure of Sudan Black B (SBB) produced by using chem. office.

1.3.1. Freedericksz transition

The Freedericksz transition (FT) was first investigated by the Russian Physicist, Vsevolod Freedericksz in 1933 [188]. Principally, a *phase transition* occurs in the molecular alignment of liquid crystals when either an electric or magnetic field is applied. When a liquid crystal (LC) material is held between two parallel plate electrodes and an electric field is applied the LC molecules begin to align with the electric field. The molecules only become aligned above a certain voltage/electric field threshold. This threshold level is referred to as the Freedericksz transition (FT) and it is a unique property of liquid

crystal materials due to their freedom of movement [189]. It has been reported that molecular orientation can also be observed when a magnetic field is applied [190] but in this work we are principally interested in the response of the LC molecules when an electric field is applied. The FT threshold induced by an electric field can be calculated using the equation below [191]:

$$E_{th} = \frac{\pi}{d}\sqrt{\frac{K_{11}}{\varepsilon_0 \Delta\varepsilon'}} \tag{1-1}$$

where d, K_{11}, ε and $\Delta\varepsilon$ are the cell thickness, elastic constant, electrical permittivity of free space and dielectric anisotropic respectively. Then the threshold voltage can be calculated using the equation:

$$V_{th} = E_{th} d \tag{1-2}$$

combining equations (1-1) and (1-2) we can write:

$$V_{th} = \pi\sqrt{\frac{K_{11}}{\varepsilon_0 \Delta\varepsilon'}} \tag{1-3}$$

With knowledge of threshold voltage, the electric permittivity and the dielectric anisotropic parameter one can determine the elastic constant K_{11}. We experimentally determine K_{11} and discuss the experimental results later. Shown below is a schematic illustration of LC molecular alignment with and without an applied electric field see figure (1-6):

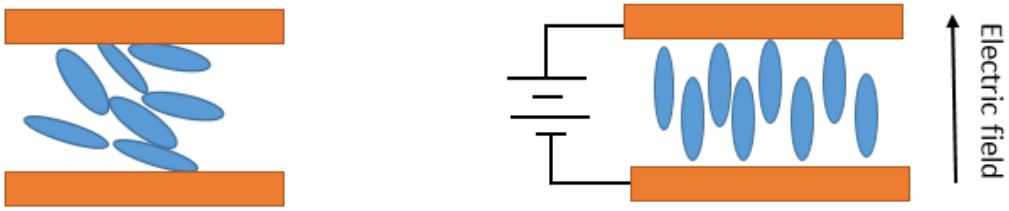

Figure 1-6: Schematic illustration show in the effect of an applying an electric field to a LC cell. When the electric field is applied as shown the director is oriented normal to the plane of the electrodes.

CHAPTER 2.

Light matter interaction

2.1. Introduction

When the light passes through a material under appropriate conditions, there is an interaction happens between the light and molecules of the materials. The light will be either transmitted, reflected, absorbed or scattered. Therefore, the sum of all intensities; transmitted, reflected and absorbed is equal to the total intensity of the incident light [192].

$$I_0 = I_T + I_R + I_A \tag{2-1}$$

Where, I_0, I_T, I_R, I_A are the total, transmitted, reflected and absorbed intensities respectively. These interactions depend on the material properties such as the refractive index of the material and the wavelength of light. Depending on the basis of interacting materials with incident light, they can be categorized into three types [193]:

A high transmission material with little absorption and reflection is called a transparent material, whereas a semitransparent material allows not all light to pass through. Materials that absorb all light are called opaque.

When light impinges on the surface of a material then due to the discontinuity of the real part of the refractive index, some of the light will reflect and the rest will be transmitted [194]. The reflected power of light depends on different parameters; refractive index of material, refractive index of atmosphere, polarisation and the angles of incidence and transmittance light. The reflection coefficient of both *S* and *P* polarisation are given by the Fresnel equations [195]:

$$R_s = \left[\frac{E_r}{E_i}\right]^2 = \left[\frac{n_1\cos(\theta_i) - n_2\cos(\theta_t)}{n_1\cos(\theta_i) + n_2\cos(\theta_t)}\right]^2 \quad (2\text{-}2)$$

$$R_p = \left[\frac{E_r}{E_i}\right]^2 = \left[\frac{n_1\cos(\theta_t) - n_2\cos(\theta_i)}{n_1\cos(\theta_t) + n_2\cos(\theta_i)}\right]^2 \quad (2\text{-}3)$$

Where, E_r, E_i, n_1, n_2, θ_i and θ_t are respectively the electric field of the reflected light, electric field of the incident light, refractive index of the material, refractive index of the atmosphere, incident angle and transmitted angle.

Then the transmission coefficient of S and P polarisation can be calculated by:

$$T_s = 1 - R_s \quad (2\text{-}4)$$

$$T_p = 1 - R_p \quad (2\text{-}5)$$

For the flat surface equations (3-2) and (3-3) can be written as:

$$R = R_s = R_p = \left(\frac{n_1 - n_2}{n_1 + n_2}\right)^2 \quad (2\text{-}6)$$

2.1.1. Refractive index

Refractive index or index of refraction is one of the important specifications of the materials and it is a dimensional physical quantity that characterize the light speed in the medium. When the light inters the medium is directly bending because the speed of light becomes different [196]. Two types of refractive index can be defined; the absolute refractive index and the relative refractive index. It can be considered as a complex quantity $(\tilde{n} = n - ik)$, n and k are the real part which is the relative refractive index and the extinction coefficient respectively [197].The absolute refractive index can be described as a ratio between the speed of light in vacuum into the speed of light in specific medium and it is always greater than 1 as the speed of light is highest in vacuum. While, the relative refractive index is the ratio between the speeds of light in two different selected mediums. The absolute refractive index is given by [198]:

$$n = \frac{c}{v} \tag{2-7}$$

Where, c and v are the speed of light in vacuum and the speed of light in selected medium respectively and the relative refractive index can be given by:

$$n = \frac{v_1}{v_2} \tag{2-8}$$

Where, v_1 and v_2 are the speeds of light in the medium 1 and 2 respectively.

The refractive index of a material can be calculated by the following equation at different wavelength [149,199–201]:

$$n = \left\{ \left[\frac{4R}{(R-1)^2} - k^2 \right]^{1/2} - \frac{R+1}{R-1} \right\} \tag{2-9}$$

Where, R is the reflectivity of the material and k is the extinction coefficient, which can be calculated by [149,200]:

$$k = \frac{\alpha\lambda}{4\pi} \tag{2-10}$$

Where, α is the absorption coefficient and λ is the wavelength.

2.1.2. Optical path length

Travelling the light from point to point in a selected medium is called an optical path length (OPL). It depends on the refractive index of medium or mediums, therefore it can be described as a multiplying the length between two point by the refractive index [202]:

$$OPL = nd \tag{2-11}$$

The OPL is equal to one when the light travels in air. Figure (2-1) shows the OPL in air and different medium.

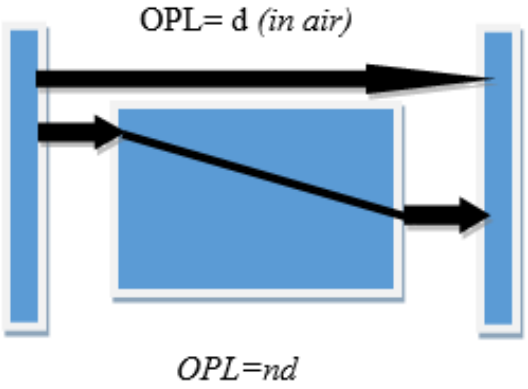

Figure 2-1: The optical path length (OPL) in air and different medium.

Moreover, the OPL can be define as follow [203]:

$$OPL = \int_a^b n(s)ds \tag{2-12}$$

By this integral equation the OPL can be described as a proportional to the time of travelling light between two points.

2.2. Excimer Laser

Excimer lasers are a type of ultraviolet lasers having a high-powered beam. Two words "excited and dimer" are constructed by the word of Excimer [204]. In 1970 Nikolia Basov, V.A. Danilychev and Yu. M. Popov invented the excimer laser at the Lebedev Physical Institute in Moscow, using a Xenon dimmer (Xe) and it is excited by an electron beam to produce the stimulated emission at the wavelength 172 nm [205]. Then many improvements have taken place since 1975. A wide range of wavelengths between 126 nm in the vacuum UV and 400 nm have been generated by the different transition of excimer lasers. The lasers media of krypton fluoride (KrF, 248 nm), argon fluoride (ArF, 193 nm) and xenon chloride (XeCl, 308 nm) are the most commercially available among these type of lasers [206,207]. Recently, another excimer laser with a short wavelength

(F_2, 157 nm) have been used in various applications [208]. In rare-gas halide lasers, the transitions can be excited in discharges such as ArF_2 laser which is shown in figure (2-2):

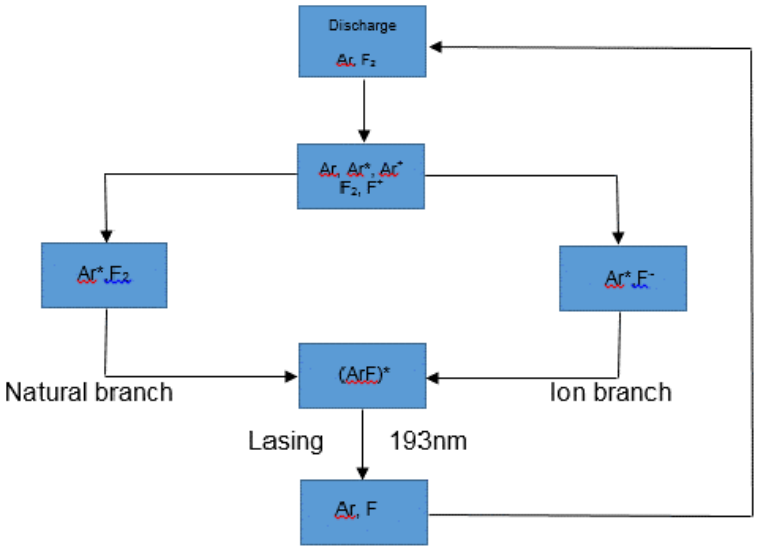

Figure 2-2: The reaction paths for generation of ArF*.

Excimer lasers have pulsed output primarily emitting electromagnetic radiation in the ultra violet spectral region. Laser temporal pulse durations are typically in the range of 10-50 ns full width at half maximum (FWHM). Excitation occurs in a gas discharge where electrons collide with halogen and rare gas species to form negatively charged halogen and positively charged rare gas ions. These ions combine to form excited bound rare gas halogen molecules in an upper level energy state referred to as an excimer state. In the upper level the excimer state is bound together for a sufficiently long time to form a population inversion. The upper laser level has a minimum in the potential energy and is relatively unstable. The upper level lifetime has a finite time and a transition to a lower energy level leads to the emission of electromagnetic radiation at the associated excimer wavelength. At the lower energy ground state level the molecules are weakly bound and they dissociate into individual halogen and rare gas species. The figure below can explain the phenomenon. The graph in figure (2-3) shows the curve of energy in (eV) as a function of atomic distance between the molecules in (nm) [207,209] .

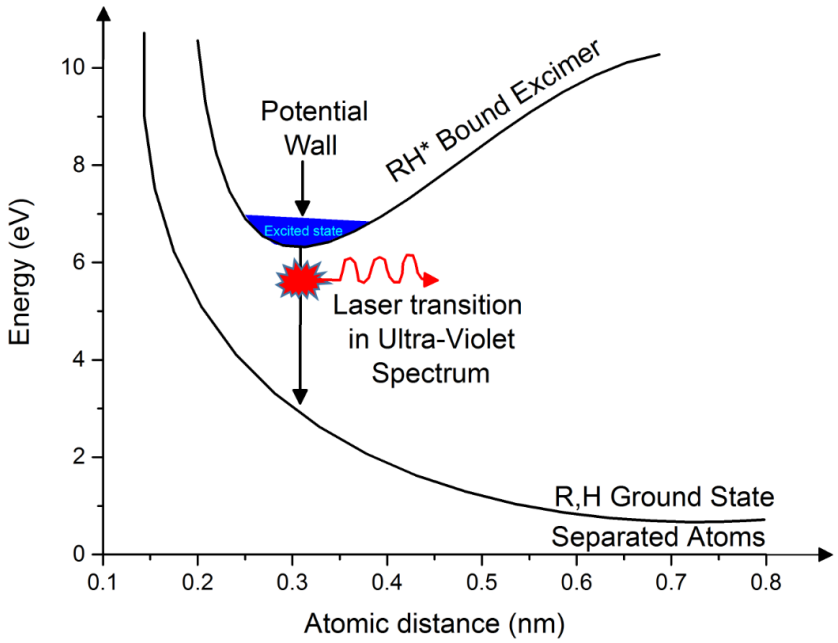

Figure 2-3: Shows a graph of energy (eV) as a function of atomic distance (nm). The lower curve shows the ground state and the upper curve the excited state. The vertical arrow indicates the optical transition between the upper and lower state [207,209].

Typically a noble-gas atom such as (Ar, Kr, or Xe) interaction with a halogen atom such as (Fl, Cl, or I) are produced the excimer lasers under the appropriate conditions of high pressure and electric stimulation [206]. For example, asymmetric molecules of ArF are caused by pumping an argon fluoride laser (ArF). Then the excimer stay retracted only in an excited state, then the atoms separate once again by the following pulse electrical discharge. Which means, the atoms excited by the pulse and causes them to fuse together into atomic pairs called dimer. While, the activation state an electromagnetic radiation is emitted by the excimers before rapidly dissociation into separate gases. This rapid dissociation is very useful in the laser system because it prevents the reabsorption of molecules of the emitted radiation. Moreover, there are two mirrors at the both ends of cavity to reflect the radiation until the radiation emitted by the front mirror. Interestingly, today excited complex (exciplexes) of rare-gas monohalides is another name of excimer lasers are used rather than excited dimmer from the active medium [207,208]. Furthermore, exciplexes occurs with some stability only in the excited state. A few

nanoseconds of radiative transition to the ground state following a fast relaxation to the lowest vibrational level within the electronically excited state can be provided by the buffer gas at a high pressure. The pumping, stimulated emission and loss processes expressions are shown below for an ArF_2 excimer laser which are describing the inherent chemical reactions and it is taken as an example because it has used in this study:

Pumping:

$e^- + Ar \Rightarrow Ar^+ + e^- + e^-$	Positive inert-gas ion production	(2-13)
$e^- + Ar \Rightarrow Ar^* + e^-$	Inert-gas metastable production	(2-14)
$e^- + F_2 \Rightarrow F^- + F$	Negative halogen ion production	(2-15)
$Ar^+ + F^- + M \Rightarrow ArF^* + M$	ArF* production (ion branch)	(2-16)
$Ar^* + F_2 \Rightarrow ArF^* + F$	ArF* production (natural branch)	(2-17)

Stimulated emission:

$$ArF^* + h\nu \Rightarrow Ar + F + 2h\nu(193nm) \quad \text{Laser emission} \quad (2\text{-}18)$$

Losses:

$ArF^* \Rightarrow Ar + F + h\nu(193nm)$	Spontaneous emission	(2-19)
$ArF^* + M \Rightarrow Ar + F + M$	Collisional deactivation	(2-20)
$ArF^* + M + Ar \Rightarrow Ar_2F + M$	Collisional deactivation production Ar_2F	(2-21)
$X + h\nu(193nm) \Rightarrow X^*$	Laser photon absorption	(2-22)

Where $*$, M and X specify the excited states of an atom or molecule, third body collision partner and impurities of the laser gas respectively. Similarly, the excitation and lasing processing of the following excimer laser (ArF and XeCl, KrF) lasers. Moreover, figure (2-4) shows the spectral properties of these lasers [206] . Fluorescence emission of 1-4 nm bandwidth is indicated by this figure. The fluorescence emission is relatively broad and the lasing process reduces the spectral width to 0.05-0.5 nm. As a results of the wide bandwidth of the fluorescence emission the wavelength of laser is adjusted in the range of 0.3-1 nm.

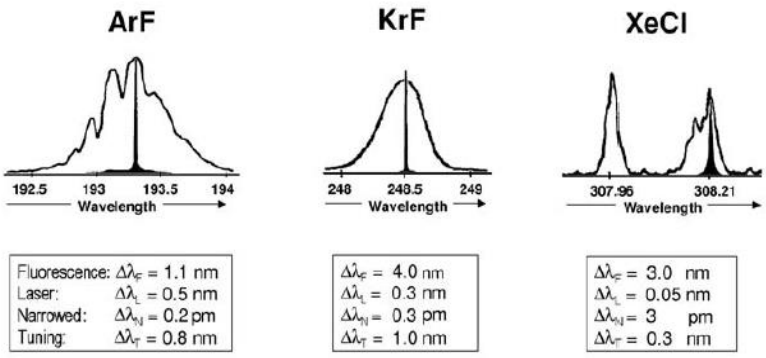

Figure 2-4: The fluorescence and lasing spectrums of excimer lasers (ArF, KrF, XeCl), $\Delta\lambda_F$, $\Delta\lambda_L$, $\Delta\lambda_N$, $\Delta\lambda_T$ represent; fluorescence, laser, narrowed and tuning respectively [206] .

A typical structure of excimer laser is shown in figure (2-5) including a gas discharge section and the laser tube [206,210]:

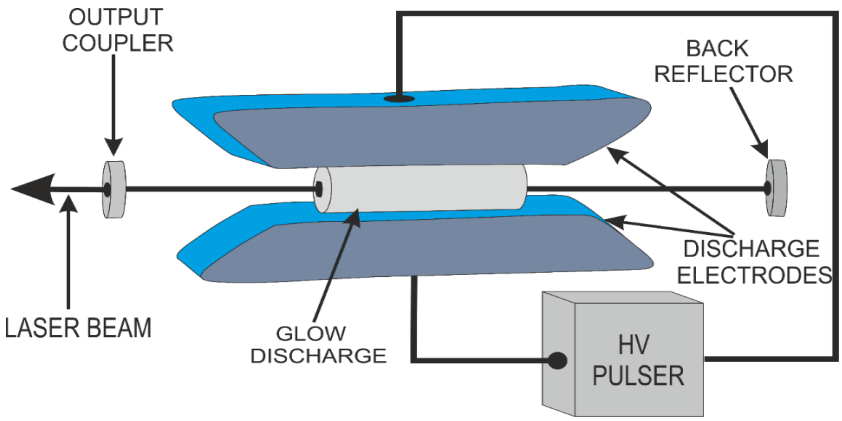

Figure 2-5: The schematic diagram of excimer laser.

The laser tube is designed to have a high pressure gas cavity and it is integrating into the discharge unit.This type of laser tube is made of a high quality electrode material such as stainless steel, polyvinyl, and Teflon [206], which give the tube a long lifetime and preventing the corrosion. In addition, output of up to several joules and repetition rates in the range of kHz can be provided by high pressure gas discharge. Typical radiative transitions for excited dimers have lifetimes that are relatively short in the range of 10-30 ns. Excimer lasers are used in a wide range of applications from semiconductor chip

manufacturing to thin film deposition. It relies on the deep ultraviolet (UV) emission at 193nm. Laser pulses duration of around 10 ns and operate at pulse repetition frequency (PRF) to 500 Hz. The beam profile is rectangular and the three dimension beam can be observed in the figure (2-6), the laser beam spot is 4×6 mm^2 [205]. The excimer laser has become a very useful source for carrying out laser ablation.

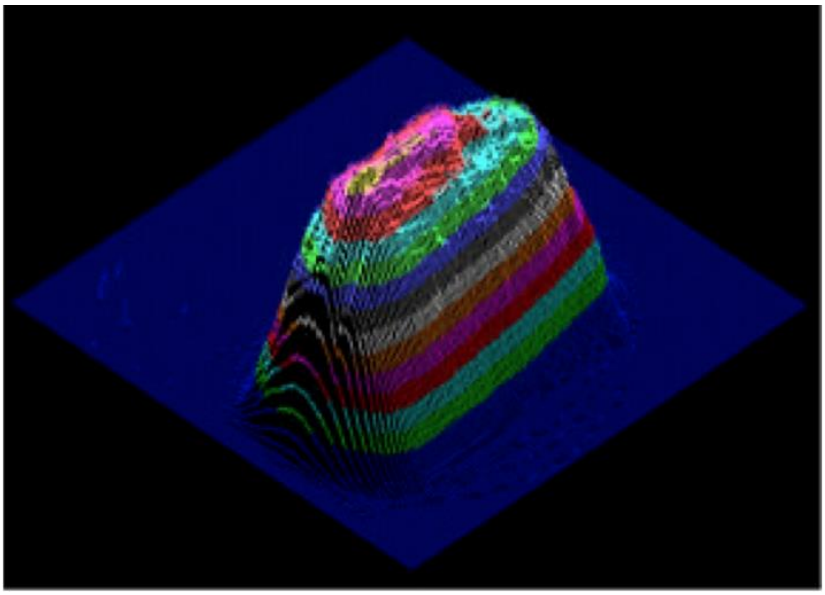

Figure 2-6: 3D beam profile of an excimer laser [205].

This is primarily due to the high degree of spatial homogeneity of the laser pulse. There are several commercial companies producing excimer lasers; GAM [1], Coherent [2], Lambda [3]. Table (2-1) below shows the typical excimer laser characteristics [209].

Table 2-1: output Characteristics of excimer laser. Note that all output Characteristics [209]

Characteristics	F_2	ArF	KrCl	KrF	XeCl	XeF
Wavelength (nm)	157	193	222	248	308	351,353
Energy pulse (J)	0.05	0.6	0.2	1.5	2.0	0.8
Average power (W)	3	60	10	160	180	70
Repetition rate	1 to 500 Hz					
Gas pressure	3-4 atm					
Pulse duration	Typically 10-50 ns					
Beam divergence	2-3 mrad					
Pulse to pulse stability	±3-6 %					
Beam dimension	10×30 nm					

2.3. Laser ablation theory

Laser ablation can be described as a complex interaction between the surface of a material and a laser beam. These interactions describe as an optical, thermal and chemical processes. The interaction includes absorption of the optical radiation and this absorption will convert into heat for thermal ablation. Ablation processing is more effective in the shorter wavelength because the surfaces of many materials have a high absorption coefficient (α, usually $\geq 10^4$ cm^{-1}) [211]. Laser having (ns, ps and fs) pulse durations play a big role in the ablation quality. Moreover, melting of materials occurs with a ns pulse duration, however, ps and fs pulse durations there is a shift away from electron and lattice vibrational coupling [212]. In this regime we speak of *cold ablation*.

Laser ablation mechanisms involves two processes thermal and non-thermal (electronic). The first one, which is a thermal process occurs when the surface is heated by the laser pulse. The expansion and vaporization are produced in this process from melted and solid areas. Both of these processes can be involved in the laser ablation mechanism. For instance, when the interaction between the laser pulse and the surface has occurred the non-thermal process is firstly happened because the surface is not heating yet. After that the temperature increases rapidly because the surface has absorbed the rest of the laser pulse and thermal process may begin [205].

There are two theory have been introduced to explain the mechanism of ablation the photochemical bond-breaking theory and the photothermal reaction theory. It has been suggested that UV irradiation makes fundamentals changes to the polymer surface and the radiation reacts with the polymer molecules and this reaction will create the unstable molecules for example, CO and CO_2 causing ablation on the surface [2]. The different mechanisms are discussed below briefly [213]:

Photochemical: As a result of electronic excitation in direct bond breaking.

Photothermal: Thermalizing of electron excitation on Pico second timescale resulting in thermal bond breaking.

Photophysical: In this model there are two processes thermal and non-thermal play a role. Therefore, this model is more applicable to short laser pulse.

Ablation processes are depicted by another method which divided into two models surface model and volume model. The volume model describes the ablation process within the bulk of the materials and can be subdivided into the photochemical volume model and photothermal volume model. However, the surface models take into consideration only a several monolayers of the materials. This model is subdivided into two models which are photochemical surface model and thermal surface model [214,215]. Different applications fields follows [216]:

Micro-structuring: Using lasers to ablate and structure different substrate materials.

2.3.1. Ablation threshold

The ablation threshold is the beginning point for removing materials, and it describes the energy density to be enough for ablation either photochemical or photophysical. In another word, the ablation processing is significant above the ablation threshold. It is varying from polymer to another, and it depends on many factors. Some of them are related to the nature and strength of the bonds in the polymer type, others depending on the laser wavelength. Table (2-2) shows the ablation threshold for some materials [217].

Table 2-2. Ablation threshold fluence for some selected materials, (Polystyrene (PS), Polyethylene terephthalate (PET), Polycarbonate (PC), Polyimide (PI) and Photoresist material [218].

Material	Fluence ($mJcm^{-2}$)	Wavelength (nm)
PS	15.3	193
PET	18.4	193
Truemode™ acrylate polymer	20	248
PC	21.5	193
PI	25.1	193
Photo resist	30	-
PC	40	-
PI	~40	248

The ablation threshold can be presented as a plot of the laser etch rate versus the logarithmic scale of fluence at the onset of significant ablation we refer the *ablation threshold* [219]. There is a trend, see table (2) where we see the reduction in the ablation threshold with decreasing wavelength. For example, the ablation threshold for Polyimide is 25 $mJcm^{-2}$ at 193 nm whereas it is 100 $mJcm^{-2}$ for the same material at 355 nm, and therefore there is an approximately a four times difference between these two wavelengths. The ablation threshold can be obtained experimentally by the Lambert-Beer law: [213,220].

$$d(F) = \frac{1}{\alpha_{eff}} \ln\left(\frac{F}{F_{th}}\right) \tag{2-23}$$

Where $d(F)$ is the ablation rate per pulse, α_{eff} is the effective absorption coefficient, F the irradiation fluence, and F_{th} is the ablation threshold fluence.

Ablation parameters can be obtained by the equation (2-23) as well as the ablation threshold which are the ablation rate $d(F)$ and effective absorption coefficient α_{eff}. The ablation rate refers to the total of mass per laser pulse ablated from the sample. For thermal and non-thermal ablation mechanisms the ablation threshold decreases with increasing the absorption coefficient α [221]. This is because the small volume of material will be excited by the laser energy. Various measurement methods can give very different

ablation rate. This occurs with some materials when the ablation process does not begin with the first pulse, but it starts after successive pulses, or the depth of ablation crater is difficult to measure because it is too small. In this regime laser ablation is referred to as the incubation effect [222], and occurs when the physical or chemical material is modification by successive laser pulses.

2.3.2. Ablation rate

The ablation rate can be explained as the mass removed from the target after one laser pulse at a specified laser fluence [223]. The results of measuring the ablation rate can be influenced by successive absorption of laser pulses. Ablating a material close to the ablation threshold may result in material not being removed. However, on receiving laser pulses at the same laser fluence may have the effect of increasing the absorption resulting in material removal. This is referred to in the literature as incubation. The ablation rate can be written using equation (2-23). By this equation, the ablation threshold can be defined as the slope of plot the logarithm of the laser fluence on the x-axis versus the ablation depth on the y-axis.

Three fluence ranges can be observed and are shown in figure (2-7) [222]. These three ranges can be explained as follows:

Low Fluence Range: The ablation threshold in this range is defined, also in this range, the incubation can be noticed.

Intermediate Fluence Range: In this range of fluence the slope of the ablation rate would be increased, and this occurs because there is a more efficient ablation of the polymer.

High Fluence Range: In the ablation processing the laser light is incident on different materials, for example, solid, liquid, and gaseous ablation products and the laser produced plasma.

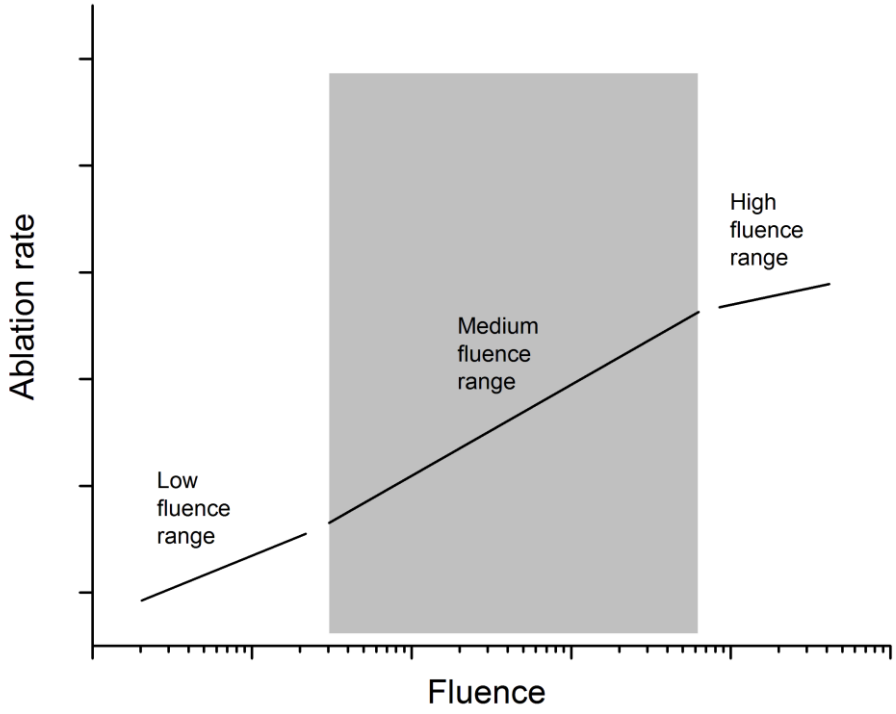

Figure 2-7: Laser ablation rate vs. laser fluence and showing three different regimes in polymers [222].

2.3.3. Mechanisms of ablation

Laser ablation processing with ultrashort short laser pulses of a massive power and small energy has been becoming very important and powerful [224]. This is because, in this type of laser, the energy of the laser is delivered to the material at a rate to be absorbed causes evaporating or flying parts. Since the laser ablation has been discovered but is not fully explored. Laser pulse ablation processing can be classified into two important mechanisms [225]; thermal, photophysical and photochemical mechanisms. As well as some materials are involved with a photoacoustic mechanism such as biopolymer materials. The ablation mechanisms are shown in figure (2-8) [226]. The type of materials plays a main role in determining which mechanism is taking place on the surface [227]. These ablation mechanisms will discuss in more details below.

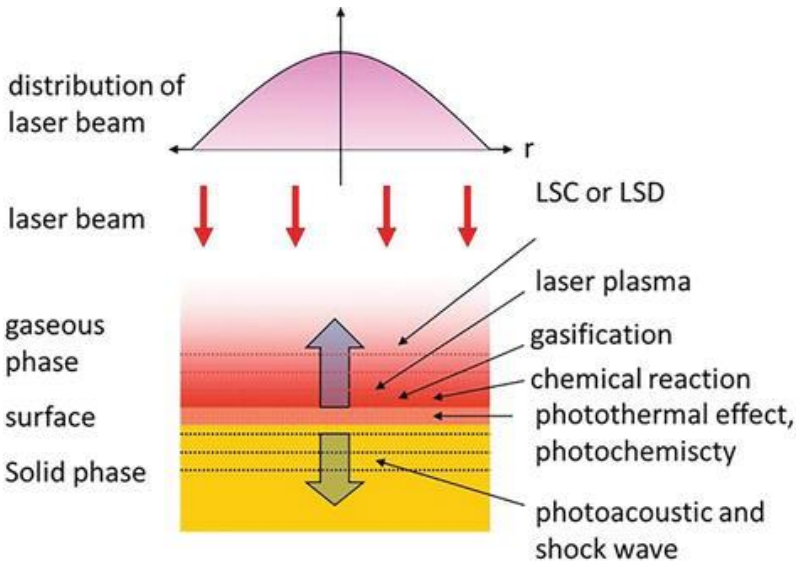

Figure 2-8: The interaction ablation mechanisms including photothermal, photochemical and photoacoustic mechanism [226].

2.3.3.1. Photothermal ablation

Two types of the photothermal ablation mechanisms; thermal and non-thermal are involved in the ablation processing [228]. For the thermal processing, the laser light is absorbed directly by the electrons of material. In this case, the energy is transferred to the atomic lattice which causes a melting and vaporisation of the material. There is a various in the vaporisation for the chemical material due to the difference in the latent heat of vaporisation. All these processes are shown in figure (2-9) below for the nanosecond laser ablation [229].

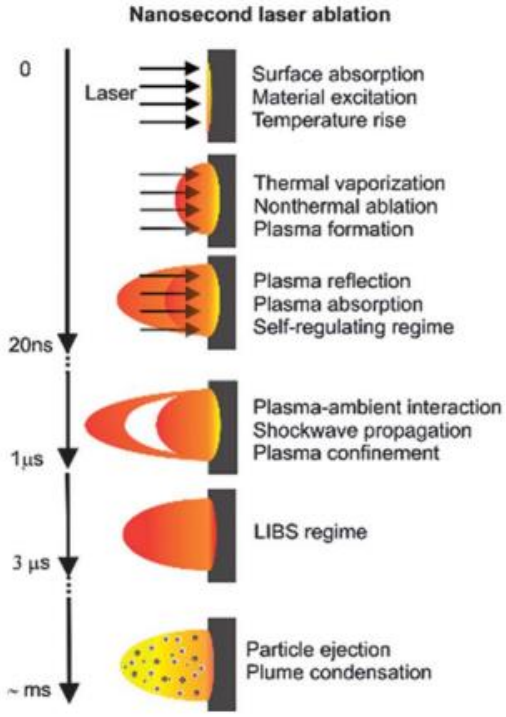

Figure 2-9: The energy absorption and ablation mechanism time scale for the nanosecond laser ablation [229].

The thermal model can be divided into three cases [224]: First case: The relaxation times is very short compared to the laser pulses. Second case: Maintaining the thermal equilibrium with the short pulses but the evaporation causes the heating of sample. Third case: The structure relaxation times are long compared the ultrashort pulses. In this case the non-thermal equilibrium will happen.

The laser ablation processing can be considered as a thermal process when the activated desorption time compared to the thermal relaxation time τ is very long [221]. Following heating by the thermal process the material starts to evaporate after the first melting. Moreover, if the chemical structure gets a sufficient heat, then the weak bonds will break. For polymers, the evaporation occurs without reaching the melting point. The photothermal laser ablation processing was reported for different polymers [230]. In this study, a temperature distribution was studied in the size of 1 μm and with resolution of time 1 μm. The thickness of the layer ablated (Δh) per pulse depends on the optical

penetration depth and the thermal penetration depth. The condition of the thickness can be defined as [225]:

$$\Delta h \approx \max\left(l_{T,} l_{\alpha}\right) \tag{2-24}$$

l_{α} is the optical penetration depth which is defined by $(l_{\alpha} = \alpha^{-1})$ where α is the absorption coefficient. l_T is the thermal penetration depth $\left(l_T \approx 2\left[D_T \tau_l\right]^{1/2}\right)$where D_T and τ_l are the thermal diffusivity and thermal relaxation time respectively. Moreover, the velocity of removal material can be defined as [225]:

$$V = V_0 \exp\left(-\frac{\Delta E}{T_s}\right) \tag{2-25}$$

Where, ΔE, Ts are the energy of the bond breaking and the temperature of the surface respectively.

2.3.3.2. Photochemical ablation

The photochemical ablation is a type of the nonthermal process [224]. In this type of ablation mechanism, chemical bonds are broken directly by the photon energy, but they are not affected by the heating. The photon energy can be calculated by $(h\nu)$ or $\left(hc/\lambda\right)$, h is the Planck's constant, ν is the radiant frequency, λ is the light wavelength, and c is the light velocity. The photochemical ablation mechanism is not involved in changing the temperature of the surface [231]. Taking in consideration, a polymer material composed of a long chain and for easy ablation can break the bond into small pieces by a direct photochemical effect. By simplified the intensity distribution inside the material which is given by Bouger- Lambert-Beer law then the photochemical law can be described as [232]:

$$h_e = \begin{cases} 0 & \Phi < \Phi_{th} \\ \dfrac{1}{\alpha}\log\left[\dfrac{\Phi}{\Phi_{th}}\right] & \Phi \geq \Phi_{th} \end{cases} \tag{2-26}$$

Where h_e is, the etch depth per pulse, α is the effective absorption coefficient, Φ is the laser fluence and Φ_{th} is the ablation threshold.

2.3.3.3. Photo-physical ablation

A photophysical process is a type of ablation mechanism which consists of both thermal and non-thermal (photomechanical) processes [221]. The photophysical mechanism can be explained by the following equation [233]:

$$X = x_{photomechanical} + x_{photothermal} \tag{2-27}$$

$$X = \frac{1}{\alpha_{eff}} \ln\left(\frac{\Phi}{\Phi_{th}}\right) + \frac{1}{D}\int_{\Phi_{th}}^{\Phi} \frac{1}{\Phi}.\exp\left(B/\Phi\right)d\Phi \tag{2-28}$$

The photochemical ablation can be easily made with ultraviolet energy higher than 3.5 eV because the higher laser energy gives a rise of the excitation of material electron [234]. However, the photothermal ablation happens on the polymer by converting the electron energy to heat up the sample which is caused increasing the surface temperature via non-radiation transition [235].

2.3.4. The Laser ablation of biocompatible material

Laser ablation of bio-compatible and bio-degradable materials continue to be of great interest in a wide range of scientific and industrial areas [236]. Chitosan is a natural polymer β-l,4-1inked 2-amino-2-deoxy-D-glucopyranose that is used in medical applications and drug delivery [237,238], antimicrobial applications [239], tissue engineering [240], realisation of waveguides [241] and diffraction gratings [242]. Several preparation methods are available which include; spin coating for thin film work [243,244], casting methods [245] and gravity assisted drop-sphere techniques for producing spherical samples [245,246]. Laser processing of natural polymers are also of interest from a laser processing and light-matter interaction perspective. It is therefore of

interest to understand the light matter interaction processes as this will provide information as to which type of laser is best suited to process a specific material. With respect to laser processing of chitosan reported in this work it is important to minimise thermal damage and denaturation. For a knowledge, one of the first work on excimer laser ablation of chitosan was carried out by Lazare *et-al* [247]. A KrF laser emitting at 248 nm was used to study the ablation of collagen, chitosan and PMMA. Laser ablation resulted in foaming of the material in the irradiated region and the mechanism attributed to photo-acoustic effects. This work reports experimental results of laser ablated chitosan using an ArF laser emitting at a wavelength 193 nm. Stress wave simulations is carried out and discussed.

Lasers continue being used to study light-matter interactions of a wide range of materials. Ablation mechanisms vary and depend on the optical and material properties of a target material and on the specific laser parameters such as wavelength and photon energy. Laser ablation of polymers and biological tissue continue to be studied frequently with a wide range of applications in mind. Excimer lasers have been frequently used to ablate or desorb material from a target surface. Typically, optical absorption depths in the ultra violet (UV) part of the electromagnetic spectrum tends to decrease with decreasing laser wavelength. Therefore, laser processing in the UV spectral region permits high depth resolution. If the absorbed energy from a laser is rapidly deposited such that the heat does not have time to relax and diffuse out of the ablation volume we have a condition called thermal confinement. This condition can be written in terms of the thermal diffusivity, χ , where the criterion for thermal confinement is that the laser pulse duration has to be shorter than a characteristic thermal relaxation time it is given as:

$$\tau_{th} = \frac{d^2}{4\chi} \tag{2-29}$$

where d is the shortest distance within the irradiated volume, either the spot size or the optical absorption depth. For many biological tissue and natural polymer's the thermal diffusivity is low (typically ~ 10^{-8} m^2s-1) and thermal denaturation is often minimal when using short laser pulses. Although only small amounts of material can be expelled from the surface of laser irradiated polymeric materials large acoustic stresses can be imparted due to recoil momentum [248]. Photo-mechanical mechanisms have been widely reported on laser ablation of biological tissue and polymeric materials [14]. The photo-acoustic (PA) mechanism can take place when energy from a pulsed laser is rapidly transferred to a material. The PA mechanism can be formally quantified in terms of the laser pulse duration τ_p. If the laser pulse duration, τ_p is shorter than the acoustic relaxation time τ_{ac} a condition of stress or inertial confinement can take place. Stress confinement can be written in terms of these two parameters as, $\frac{\tau_{ac}}{\tau_p} \geq 1$. Under this condition, an irradiated material does not have sufficient time to reconfigure by changing its volume and consequently an increase in the internal pressure can occur. Under conditions of stress confinement, a compressional wave develops into a tensile wave and molecular bonds can be weakened and break. Because stress waves can result in material damage without imparting significant thermal damage the ablation process is referred to as *cold ablation*. We can write a condition for stress confinement in terms of the speed of the stress wave, c_s as:

$$\frac{l_{ac}}{l_{opt}} = \frac{c_s \tau_p}{\alpha^{-1}} = \alpha c_s \tau_p < 1 \qquad (2\text{-}30)$$

where l_{opt} is the optical penetration depth and l_{ac} is the distance travelled by the acoustic wave propagating inside an irradiated material. When the above equation is satisfied changes in the internal pressure become significant. Therefore, absorption of short laser

pulses, τ_p in materials that have moderate absorption coefficients, α, can lead to photo-mechanical ablation. We note that the absorption of optical radiation and material properties are sensitive to the concentrations and preparation methods. Therefore, in this work experiments are carried out on samples that have had equal drying times before the laser ablation experiments were conducted. As the energy from the laser pulse is deposited inside a target material a compressional stress wave propagates in both the $\pm z$ direction normal to the sample surface where the positive $+z$ direction is designated as the beam propagates direction. Similarly, a compressional wave propagates in the opposite $-z$ direction towards the free surface of the sample. At the free surface there is in general a high acoustic reflection coefficient at the air-material interface and the acoustic stress wave is reflected back into the bulk of the sample in the +z direction. As the compressional wave relaxes a tensile stress wave builds up and propagates back into sample. The magnitude of the tensile stress increases with depth into the bulk of the material before decaying away.

Such tensile stresses may lead to bond breakage, cavity formation and bubble nucleation. In some cases, depending on the laser fluence, heat may also be generated and lead to laser induced material damage. For an isotropic solid the laser induced stresses can be described by a general stress-strain tensor shown below [251]

$$\sigma_{ik} = \frac{3B}{1+\sigma}\left[\left(1-2\sigma\right)\varepsilon_{jj} + \sigma\varepsilon_{kk}\delta_{ik}\right] - B\beta\Delta T\delta_{ij} \tag{2-31}$$

where B is Young's modulus, σ (without subscripts) is the Poisson ratio, ε_{jj} are the induced strains and δ_{ik} is the Kronecker delta function. The stress-strain tensor takes on negative and positive signs for tensile and compressive stresses respectively. The last term in the stress-strain tensor, $B\beta\Delta T\delta_{ij}$, corresponds to the maximum stress. A relative

change in volume can be written in terms of the strains as $\frac{\Delta V}{V} = \varepsilon_{kk} = \varepsilon_{11} + \varepsilon_{22} + \varepsilon_{33}$. On absorption of a short duration laser pulse and if $\varepsilon_{kk} = 0$ the condition of stress confinement is obeyed. In this context, short laser pulses refer to the laser pulse duration being less than the acoustic transit time, $\tau_p << \tau_{ac} = \frac{d}{c_s}$. Where *d* is the shortest distance in the irradiated volume. The circular geometry and axial symmetry of the ablation sites used in this work is suited for the use of polar coordinates. In many laser ablation experiments there are cases where the radial stresses, σ_{rr} and circumferential stresses, $\sigma_{\Phi\Phi}$ become significant and contribute to laser induced damage [252]. Although the magnitude of circumferential stresses are smaller than longitudinal stresses, circumferential (Hoop) stresses can exist for extended lifetimes and therefore play a significant role in laser induced damage. As radial stresses are induced inside an ablation crater the expanding material can push material outwards inducing circumferential tensile stresses in the region outside of the ablation crater [253]. Shown below are expressions for the radial and circumferential stresses respectively:

$$\sigma_{rr} = \frac{E}{1+\sigma}\left(\frac{\partial^2 \varphi}{\partial r^2} - \nabla^2 \phi\right) \tag{2-32}$$

$$\sigma_{\Phi\Phi} = \frac{E}{1+\sigma}\left(\frac{1}{r}\frac{\partial \phi}{\partial r} - \nabla^2 \phi\right) \tag{2-33}$$

where ϕ is the thermo-elastic displacement potential [254]. These stresses can become important considerations especially when laser beams have circular symmetry and when using circular object masks. Shown below is an equation for thermo-elastic wave written in terms of the velocity potential, ϕ .

$$\nabla^2 \phi - \frac{1}{c_s^2}\frac{\partial^2 \phi}{\partial t^2} = \frac{\beta}{\rho C} S \tag{2-34}$$

S is a heat source term per unit time and volume, and C is the specific heat capacity. From the velocity potential one obtains the velocity by taking the gradient of ϕ.

$$v = grad\phi \tag{2-35}$$

and by taking the partial derivative of ϕ one obtains the pressure as shown below.

$$P = -\rho\left(\frac{\partial\phi}{\partial t}\right) \tag{2-36}$$

The pressure developed inside a target depends on the relative volume change plus any addition of a change in the material temperature and we can write the over pressure as:

$$P = -B\frac{\Delta V}{V} + B\beta\Delta T \tag{2-37}$$

where β is the volume expansion coefficient, V is the volume of the irradiated material, B is the bulk modulus and T is the corresponding temperature of the material. Of relevance in this work is to estimate the pressure at a laser fluence F as shown below:

$$P = \pm\frac{\beta AF}{C_P\alpha\tau_p^{\,2}}\left(1-e^{-\alpha z}\right) \tag{2-38}$$

where A is the absorptivity (1-R), where R is the optical reflectivity of the material at the corresponding wavelength and the remaining parameters have been defined earlier. We note when energy is rapidly deposited by a laser pulse the tensile stress evolves. In this work we simulate an acoustic wave propagating inside chitosan using an approach as previously reported [20,22]:

$$P_0(z,t) = P_1 + P_2 + P_3 \tag{2-39}$$

$$P_1(z,t) = 0.5P_{\max}e^{-\alpha(z-c_s t)} \qquad z > c_s t \tag{2-40}$$

$$P_2(z,t) = 0.5P_{\max}e^{-\alpha(z+c_s t)} \qquad z > 0 \tag{2-41}$$

$$P_3(z,t) = 0.5P_{\max}R_s e^{-\alpha(c_s t-z)} \qquad c_s t > z > 0 \tag{2-42}$$

where the maximum pressure, $P_{\max} = \Gamma \alpha F$, can be written in terms of the laser fluence, F, the absorption coefficient, α and the Gruneisen coefficient, $\Gamma = \left(\frac{\partial \ln P}{\partial \ln U/V} \right)_V$ where U and V are the internal energy and volume respectively. $R_s = \frac{Z_{air} - Z_{chit}}{Z_{air} + Z_{chit}}$ is the reflectivity of the acoustic wave, and $Z = \rho c_s$ is the acoustic impedance of air and chitosan. The resulting pressure wave $P_T(z,t)$ can be found by carrying out a convolution of the acoustic wave with the temporal laser pulse $g(t)$ and is written as:

$$P_T(z,t) = g(t) \otimes P_0(z,t) \tag{2-43}$$

$$P_T(z,t_2) = \int_0^{t_2} g(t_1) P_0(t_2 - t_1) dt_1 \tag{2-44}$$

The laser pulse used in the simulations is represented by $g(t)$ and the function closely resembles the ArF 193 nm excimer laser pulse used in these experiments.

$$g(t) = t^2 e^{-\frac{t}{\tau}} \left(\int_0^{\infty} t^2 e^{-\frac{t}{\tau}} dt \right)^{-1} \tag{2-45}$$

In this work the laser pulse duration τ_p = 11.5 ns FWHM. The simulation was implemented using MatLAB. In the simulations presented here positive and negative values correspond to compression and tensile stress respectively.

CHAPTER 3.

Diffraction Grating Theory

3.1. Introduction

Diffraction gratings are optical components that consist of a periodic structure. A physical periodicity is referred to an amplitude grating whereas if the grating has a modulated refractive index it refers to a phase grating. Light either reflected or transmitted from a diffraction grating is split into beams that propagate into different directions are called diffraction orders [258]. Two parameters, the grating period and the wavelength of light determine the directed angles of the diffraction orders [259–261]. The spectral range, resolution and the performance of diffraction gratings are dictated by the groove density (period), depth and the profile of the diffraction grating [262].

In 1758, Rittenhouse discovered the principle of the diffraction grating, but no attention was attracted to it [263]. Afterwards, the early research on diffraction gratings was done by Fraunhofer [264]. The fundamental physical work of the diffraction grating is the spatial variation in refractive index of the grated surface. The variation in refractive index of the grated surface will modify either amplitude or phase or both of electric field of the light incident on the grating. Two types of grating are found; transmission grating and reflection grating [265]. Transmission grating can be divided into two categories; transmission amplitude grating and transmission phase grating. Amplitude gratings (wire grid type) periodically block light whereas phase gratings, as the name suggests, changes the phase of the propagating wave. Phase gratings can be realised in two ways, having a modulated refractive index or by having a binary relief structure on a surface such that the optical path length is modulated. Gratings can also be divided into transmission or

reflection gratings. In the type of a transmission grating, a transparent surface is superimposed with a periodic grating, whereas, superimposing a reflective surface with a periodic grating will generate a reflection grating. Usually, reflection grating is widely used for optical communication such as pulse compression. The reflection and transmission gratings are shown by figure (3-1 a and b) respectively [43]. Geometry in figure (3-1a and b) illustrates diffraction of light by a reflection and transmission gratings. It shows the grating diffracts light rays of wavelength (λ) at angle α for a diffraction grating that has a groove spacing d . The different diffracted angles are represented by a set of angles β_m measured from the grating normal. The successive groove reflect the rays of light and the difference between the corresponding angles can be written [266]:

$$\Delta = \Delta_1 - \Delta_2 = a\sin\alpha_i - a\sin\beta_m \tag{3-1}$$

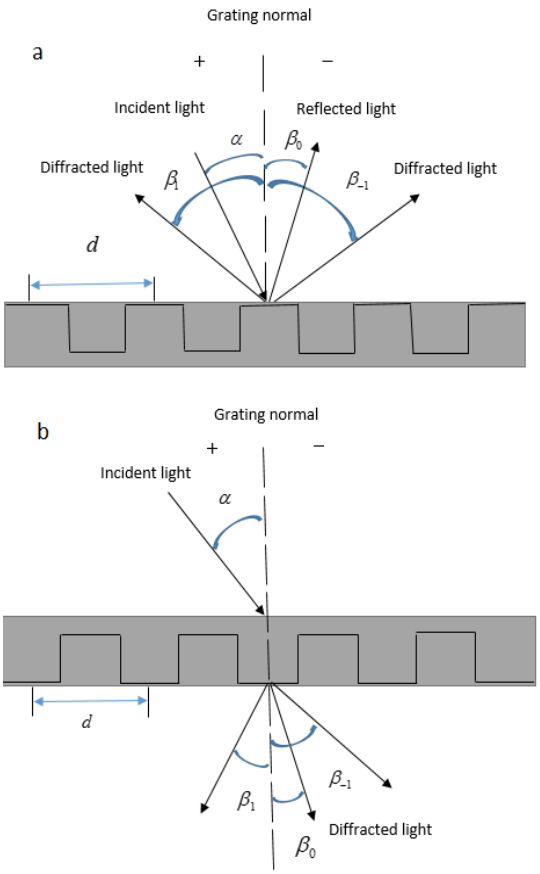

Figure 3-1: (a) Reflection grating, the incident light and diffracted rays are on the same side of grating
(b) Transmission grating, the incident light and the transmission rays are on the opposite side of the grating.

where $\Delta = m\lambda$, an integer multiplied by the wavelength of light, α_i is the angle of the incident light and β_m is the angle of both rays which have different directions after diffraction. Later, the grating fabricated out of gold films deposited on glass substrates by Fraunhofer. He fabricated diffraction gratings with the aid of a ruling machine. This consisted of a sharp diamond tip that was used to scribe (ruled) directly onto a glass surface [263].

3.2. The specifications of diffraction grating

The importance of the diffraction gratings arisen because they transmit or reflect light in different angles depending on the properties of the grating. These diffraction order are very sensitive to the wavelength of the incident light. Diffraction grating can be specified by resolution and order efficiency. The importance of these features depend upon the specific applications [261].

3.2.1. Resolution

Resolution feature is the most important parameter to assist the performance of the grating devices. Increasing the density of grooves can be used to improve the resolution power of the spectrometers [267,268]. Measuring the ability to separate adjacent spectral lines are of average wavelength λ is the resolution of the grating [264]. Usually, the resolution of the grating is called the resolving power and it can be expressed as [43,269]:

$$R \equiv \frac{\lambda}{\Delta\lambda} = |m|M \tag{3-2}$$

Where, *m, M* and Δλ are the diffraction order, groove intensity and the limit of resolution respectively. For two lines in the diffraction grating which having the same intensity the difference in wavelength and for the peak of two wavelengths λ_1 and λ_2 can be given [270]:

$$\left|\lambda_1 - \lambda_2\right| < \Delta\lambda \tag{3-3}$$

Theoretically, the resolving power can be given [261]:

$$RP = mN \tag{3-4}$$

$$RP = \frac{mW}{d} \tag{3-5}$$

$$RP = \left(\frac{W}{\lambda}\right)\left(\sin\alpha - \sin\beta\right) \tag{3-6}$$

Where, *m, N, W* are the diffraction order, the total number of grooves and the width of grating respectively. In ideal grating the resolving power influenced by the grating width and the incident and diffraction angles.

3.2.2. Efficiency

The diffraction efficiency is the distribution of the incident light energy between the diffraction order [264,271]. It depends on various parameters; groove shape, incident angle and the coating reflectance [272]. The directions of modes are predicted by the diffraction equation while this equation does not determine how much power is in them. The diffraction efficiency is a value that expresses that, how much energy can be obtained from diffracted light with respect to the energy of the incident light [270]. Generally, the efficiency of diffraction can be expressed by two ways, "absolute diffraction efficiency" and "relative diffraction efficiency." The absolute diffraction efficiency is the ratio of the diffracted light intensity, of a specified order, to the incident light intensity, and the relative diffraction efficiency is obtained by dividing the absolute diffraction efficiency by the reflectance of the coating material [261,271], minus the losses [264]. The total efficiency is the sum of all the energy that carrying out by all diffraction orders [264]. Different factors are effected the absolute efficiency; the groove shape, the amount of scattering energy, the surface grating reflectivity [261], The angle θ and λ/d [270]. For

the grating has a profile that can be expressed by $\lambda/a = f(x/a)$ irradiating with the wavelength λ with a fixed incident angle θ produces the same efficiencies for all modes:

3.2.3. Dispersion

Dispersing the light spatially by wavelength is the main purpose of the diffraction grating. As discussed above, when a light incident on the grating the diffraction orders are produced and separating then each order will be diffracted into a different direction [273]. Measuring the separation between diffracted light of a different wavelengths either spatially or angular is called a dispersion. Two types of dispersion; angular dispersion and linear dispersion. Angular dispersion can be expressed by the spectral rang per unit angle while the linear dispersion is expressed by the spectral range per unit length. When the angle of incident light is fixed the angular dispersion can be gotten by differentiating the grating equation with respect to the wavelength to be [264,273,274]:

$$\frac{d\theta_d}{d\lambda} = \frac{m}{d\cos\theta_d} \tag{3-7}$$

Therefore, the ratio $\frac{d\theta_d}{d\lambda}$ can be defined as an angular dispersion which is a rate of changing the dispersion angle of light with wavelength. Moreover, the angular dispersion is produced by the incident angle and the groove spacing [272]. Therefore, increasing the incident angle will increase the dispersion as well as the dispersion can be increased by decreasing the groove spacing. A high resolution of grating can be obtained with a large dispersion.

3.3. Types of Diffraction Grating

Some criteria are usually used in dividing the diffraction grating [260]: their geometry, their material, behavior of their efficiency and manufacturing methods. Commonly, diffraction grating are classified into two broad groups: amplitude gratings and phase

gratings [264]. Amplitude gratings are simply changing the amplitude of the incident light through the grating structure. An example is shown in figure (3-2) below. These types of grating consisting of changing the imaginary part of the refractive index of grating material. The first gratings built were amplitude gratings. These gratings spatially modulate only the amplitude of the transmitted wave by either attenuating the beam or blocking it periodically. Whoever, phase grating is different because it is consisting of changing the phase of the incident light and it related to the differences of a real part of the refractive index of the material. Most of the gratings used in different applications are phase grating produced either by laser direct ablation [9] ,diffraction-mask projection [275] or nanoimprinting methods [276–278]. Figure (3-3) shows both types of phase grating; transmission phase grating and reflection phase grating. The diffraction efficiency of the first order of the diffraction grating has measured as a function of the grating half pitch [277]. The diffraction efficiency of the transmission grating has measured because this type of grating has widely used in different devices [279,280].

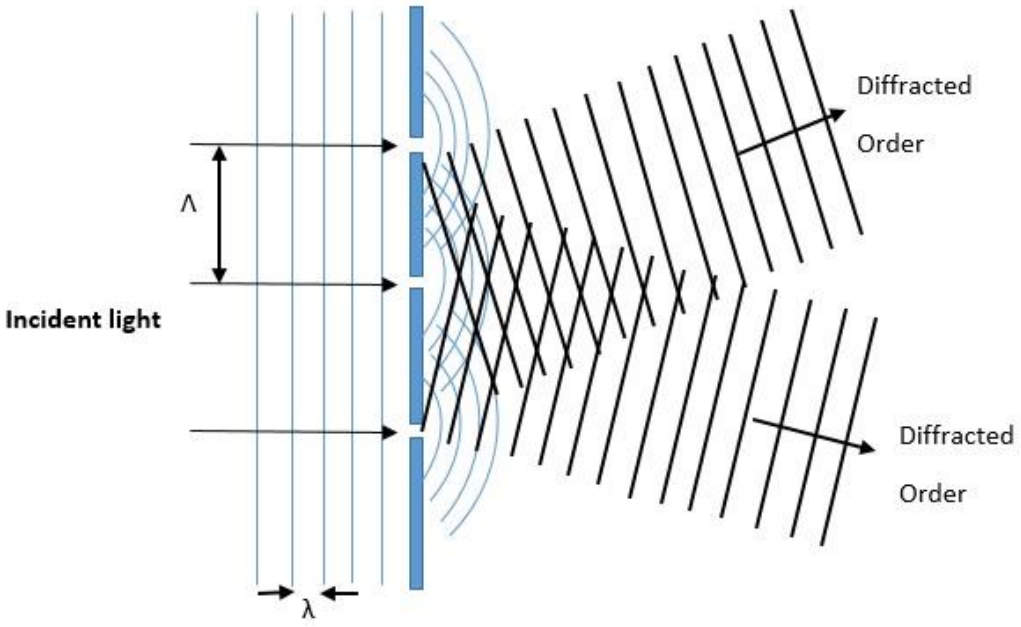

Figure 3-2: The amplitude grating

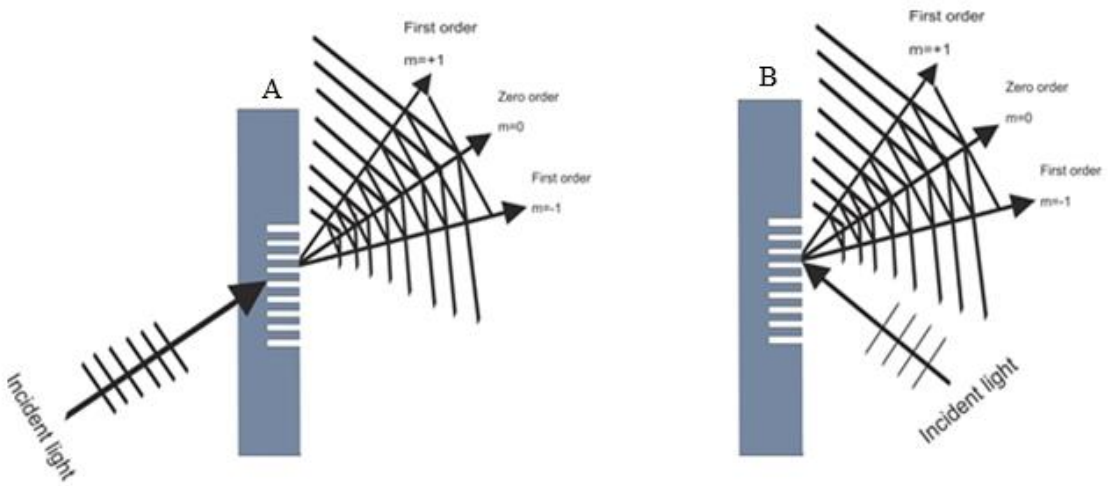

Figure 3-3: (A) Transmission phase grating. (B) Reflection phase grating

3.4. The Diffraction Equation

Grooves diffract the incident light on the grating surface [264]. In fact, the light is reflected and transmitted by the each groove; therefore, each groove converts a very small source of light. The light incident at θ_i on the grating normal is shown in figure (3-4):

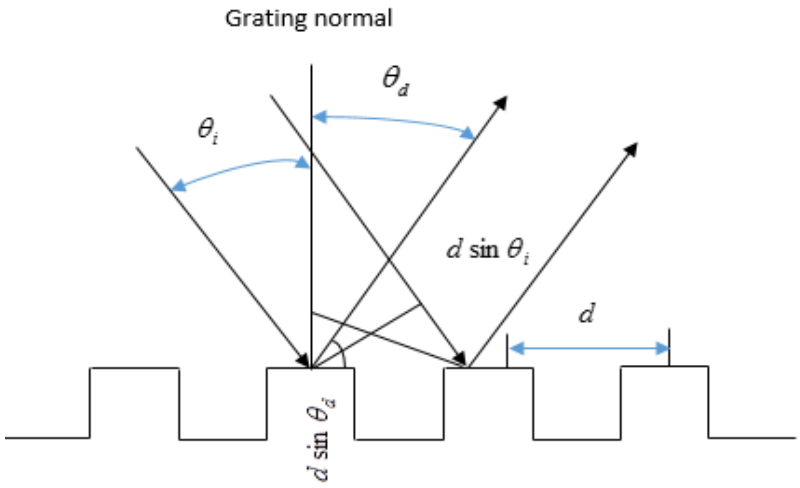

Figure 3-4: Phase relation between the rays diffracted from adjacent grooves.

The successful grooves diffract the light in a direction θ_d and the path difference of rays can be described by ($d \sin\theta_i - d \sin\theta_d$), where d is the grooves spacing, and the

interference just only happened when the difference equal to the wavelength of light. The equation below called a grating equation [264,267], and it illustrates the distinguished direction of the diffract incident light:

$$\sin\theta_m = \sin\theta_i + m\frac{\lambda}{d}, m = 0,\pm1,\pm2.... \quad (3\text{-}8)$$

Where θ_i and θ_m are the angles between the incident and the diffracted leadership and the grating normal, λ is the light wavelength, d is the grating spacing which is typically measured in μm and m is an integer and it is some the diffraction orders. The grating frequency can be given by $\left(\frac{1}{d}\right)$, or it is called groove frequency. It gives the number of grooves per mm (gr/mm). Another form of grating equation can be written as [281]:

$$Gm\lambda = \sin\alpha - \sin\beta \quad (3\text{-}9)$$

Where $G = 1/d$ is the groove frequency, α and β are the angles between the incident and diffracted light and the ordinary grating, λ is the wavelength of light and m is the orders of the diffraction. Therefore, the equation can be written:

$$m\lambda = d(\sin\alpha - \sin\beta) \quad (3\text{-}10)$$

The right side of the equation which is $d(\sin\alpha + \sin\beta)$ gives the difference between light from neighboring grooves [43]. When $\beta < 0$, the part $d\sin\beta$ will be negative. When the difference equals the wavelength λ the constrictive interference will happen and the destructive interference will happen at all others angle. However, in case $m = 0$, $\alpha = \beta$ that is lead to low reflection and the grating will be worked as a mirror. According to the grating equation, the light of wavelength λ is permitted to be diffracted into both negative and positive orders [264]. And all the range of orders m exist for:

$$-2d \langle m\lambda \langle 2d \qquad m \text{ is an integer} \quad (3\text{-}11)$$

For *1/d* << 1, a large number of diffracted orders will be existent. The conditions below are used to distinguish between the negative and the positive orders:

$\beta \rangle -\alpha$ for the positive orders (m > 0).

$\beta \langle -\alpha$ for the negative orders (m < 0).

$\beta = -\alpha$ for the specular reflection (m = 0).

In spite of, the grating equation unable to determine the relative power directed into each of the diffracted orders, the direction of light can be determined by the equation [260].

3.5. Grating coupler

Diffraction gratings have been employed to couple light into optical waveguides [282]. This system is frequently referred to as a grating coupler system. The planar waveguide can be produced by a grating that has a periodic distribution with grating period *Λ* [283] and the diagram of grating coupler system is represented in figure (3-5).

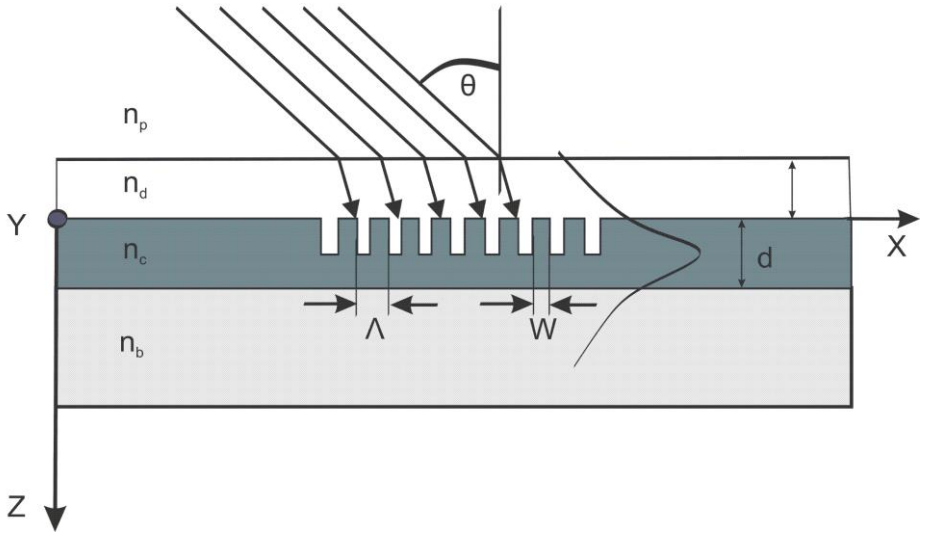

Figure 3-5: The grating coupler diagram for a planar waveguide.

The conditions of coupling the beam of the incident light into the waveguide for input coupling through the grating G_a and for output coupling through G_b are given by the following [282].

$$\left[k_a - (k_a \cdot n)n\right] + H_a = K_N = \left[k_b - (k_b \cdot n)n\right] + H_b \quad (3\text{-}12)$$

Where k_a, k_b are the wave vectors of the incident wave, outcoupled wave, n is normal to the waveguide surface, K_N is the guided wave vector, H_a and H_b, are the vector of two independent gratings. The grating period Λ of the grating coupler devices can be calculated by using the Bragg condition [284,285]:

$$n_c . \sin\theta = n_{eff} - m\frac{\lambda}{\Lambda} \quad (3\text{-}13)$$

Where n_c and n_{eff} are the effective refractive indexes of the fibre core and the grating respectively. Λ, θ, λ are the grating period, coupled angle and the light wavelength respectively.

The grating region has an effective refractive index which can be defined as:

$$n_{eff} = ff . n_{eff1} + (1 - ff) . n_{eff2} \quad (3\text{-}14)$$

Where n_{eff1}, n_{eff2} are the effective refractive indexes of the grating teeth and the grating slots respectively, where ff is the fill factor which is can be defined as the ratio of the grating teeth width to the grating period Λ.

When designing any grating coupler devices the coupling efficiency should be taken into consideration which is can be defined as a ratio between the input power to be coupled in and the output power from the grating [286]. Different approaches were employed to improve the grating coupler performance for example; corrugated a double sided cover film [287], multi-layers high reflectivity metal [286] and sub-wavelength microstructures [288].

3.5.1. Calculation of the coupling efficiency

Usually, injecting the light into the integrated optical waveguide can be done but with high insertion losses especially for the submicrometer thick waveguide [289]. Therefore,

grating coupler is considered as an alternative method to couple the light into the waveguide with a good coupling efficiency. Two calculations are required to analyses the grating coupler [290]; the first one is calculating the leakage factor of the corrugated waveguide and the second one is calculating the coupling efficiency. The expression below is used to calculate the coupling efficiency [289].

$$\eta(z)=\left[2k_{p,z}^{''}\left\{\left|r(z)\right|^2+\frac{\mathrm{Re}\left[ir(z)q^*(z)\right]}{\left(k_0\sin\theta_0+m\frac{2\pi}{\Lambda}\right)}\right\}\right]\times\left[\frac{\left(k_0\sin\theta_0+m\frac{2\pi}{\Lambda}\right)k_{z,p}^{''}}{2k_0\cos\theta_0}\int_{-\infty}^{+\infty}\left|E_{m,y}\left(k_{p,z}^{'}\right)\right|^2dx\right] \quad (3\text{-}15)$$

Where, $E_{m,y}\left(k_{p,z}^{'},x\right)$ is the complex amplitude profile of *m* diffracted order, Λ is the grating period, $k_0=\left(\frac{2\pi}{\lambda}\right)$ is the normal wave vector, θ is the incident angle, λ is the wavelength and $k_{p,z}=k_{p,z}+ik_{p,z}$ is the complex pole of *m* diffracted order field amplitude. The output power of the uniform grating structure can be expressed by [82,291]:

$$P=P_0\exp\left(-2\alpha(z)\right) \quad (3\text{-}16)$$

Where 2α is the leakage factor and it is given by the following equation [292]:

$$2\alpha(z)=G^2(z)/\left[1-\int_0^z G^2(z)dz\right] \quad (3\text{-}17)$$

Where *G (z)* is the normalized of the Gaussian beam profile.

3.6. Waveguide

In 1983 Lukosz and Tiefenthaler introduced the planer optical waveguide as an application of the grating coupler [293]. Since, introducing this type of application, many experiments has been made to optimize the sensor sensitivity. In the grating coupler

sensor the guided modes can be excited by the incident beam from either substrate side or cover side. The guided modes coupling efficiency can be given by [294]:

$$\begin{pmatrix} k_x^{'} \\ k_y^{'} \end{pmatrix} = \begin{pmatrix} k_x \\ k_y \end{pmatrix} + \begin{pmatrix} \kappa \\ 0 \end{pmatrix} \tag{3-18}$$

Where k_x and k_y are the components of the wave vector; $k_x^{'}$ and $k_y^{'}$ are the diffracted wave and $k=(k,0)$ is the grating vector of length and the k is given by:

$$\kappa = \left(2\pi/\Lambda\right)l \tag{3-19}$$

Where Λ and l are the period of the grating and the diffraction orders (l=0, ±1,±2,±….) respectively. The uncoupling condition can be expressed by the following equation when the guided modes is excited; $k_x=kN$ and $k_y=0$.

$$\pm N = n\sin\alpha_1 + l\left(\lambda/\Lambda\right) \tag{3-20}$$

Where α_1 is the incident angle measured in air and the uncoupling efficiency is given by:

$$\eta = P^{'}/P \tag{3-21}$$

Where $P^{'}$ and P are the power of the uncoupling light and power of the incident light respectively. The coupling efficiency can be described as a function of detuning variables:

$$\eta\left(\overline{N}\right) = \eta_m \hat{\eta}\left(\overline{N}\right) \tag{3-22}$$

$$\overline{N} = N - n\sin\alpha - l\left(\lambda/\Lambda\right) \tag{3-23}$$

When the condition $\overline{N}$ =0 is fulfilled, the maximum in coupling efficiency $\eta = \eta_m$ is obtained.

CHAPTER 4.

Experimental methodologies

4.1. Laser ablation methodology

Laser ablation experiments were carried out using a Lambda Physik LPF 202 laser emitting at a wavelength of 193 nm. The experimental set-up for the laser processing work is shown as a schematic in Figure (4-1). A stainless steel circular aperture of 2 mm diameter and the grid used to form the grating were positioned in a uniform part of the raw laser beam. All apertures were imaged onto the free surface of the chitosan using ×1/10 and ×1/5 magnification to identify the ablation threshold and for fabrication of the grating respectively. All samples were measured using a Scanning Electron Microscope, (SEM), model, Zeiss EVO60). Samples were mounted on a motion control stage (Aerotech, Fibre Align). The laser output passed through a dual rotating plate attenuator (Metrolux, ML2110) to control the laser fluence. Dielectric mirrors optimised for transmission at 45 degrees these were used to steer the beam such that the beam was incident from the vertical and normal to the chitosan surface. A joule meter (Melectron) was used to measure the output energy of the laser after all optical components were used in these experiments. A fast photo diode (Hamamatsu, S7911) connected to an oscilloscope (Infinium, 500 MHz, 2 Gb Samples s^{-1}) were employed for the laser pulse duration measurements.

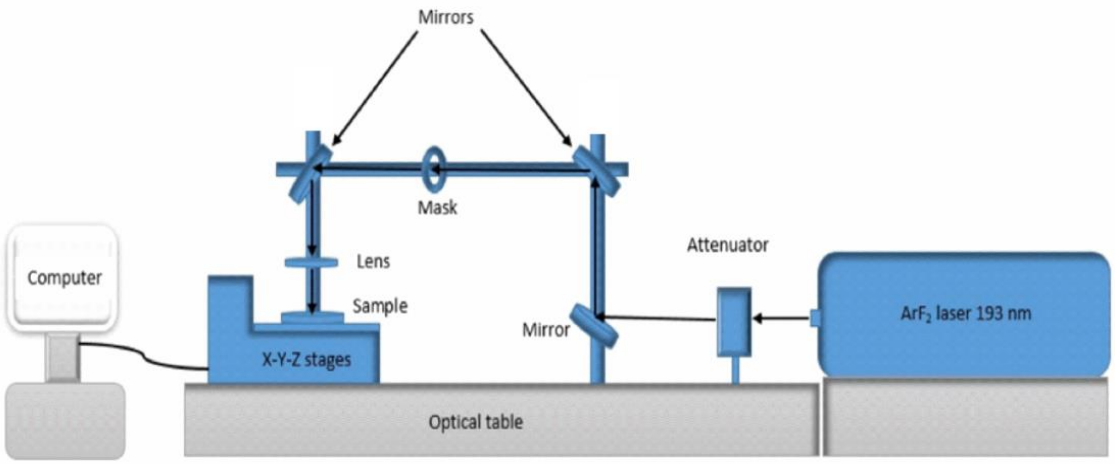

Figure 4-1: Schematic illustration of the 193nm laser system and beam delivery.

4.1.1. Laser beam delivery system

Figure (4-2) shows a beam delivery system for the laser 193 nm. It consists of a UV ArF laser 193 nm Lambda Physik LPF 202, with maximum energy of 285 mJ in an 11.5 ns (full-width at half-maximum) pulse at maximum repetition rate of 20 Hz, three Thorlabs construction rails: the standing rails are 750 mm long and have a 95 mm diameter and the horizontal rail is 2000 mm long and has a 66 mm diameter; three high energy excimer laser mirrors at an angle of 45° which have a diameter of 25.0 mm are designed to be used at 193 nm: two of them are Edmund co. mirrors which are on the horizontal rail and the third one is CVI co. on the standing rail near to the laser source; one plano-convex fused silica lens (Newport co.) with a diameter of 25.4 mm, which has a focal length of 81.8 mm at 193 nm; Aerotech motion control (x, y, z) stages; attenuator and a photo mask. The laser output passes through the attenuator and is orientated by three mirrors and a lens towards the sample, which is on the stage, the path length is approximately 2180 mm long. The output energy of the laser was measured using a Molectron joule meter. Using the output energy measurements and the area of the demagnification allowed us to determine the laser fluence.

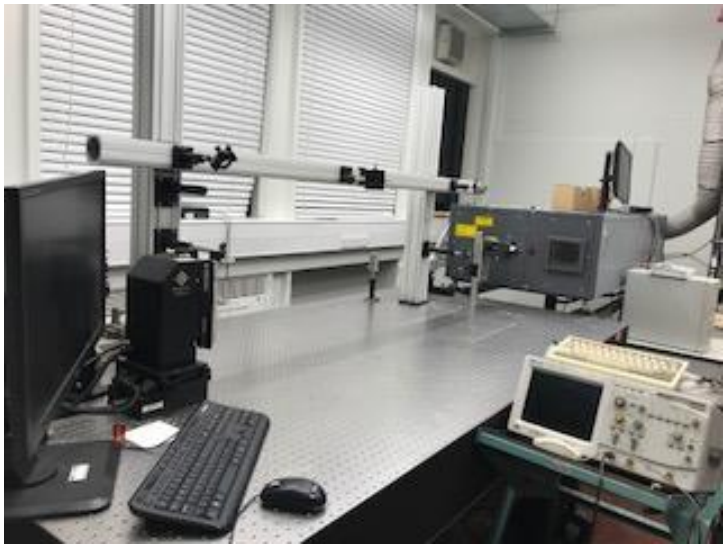

Figure 4-2: Beam delivery system of ArF 193 nm excimer laser.

4.1.2. Chitosan film preparation

Chitosan and solution used in these experiments were purchased from (Sigma-Aldrich, Chitosan-448869, 0.1M acetic acid). The chitosan solution was prepared by dissolving 0.2 mg chitosan in 10 mL acetic acid to achieve a 2% concentration. The chitosan solution was spin coated, (Oscilla) onto soda-lime glass microscope slides, (Thermo Scientific) to produce chitosan films. A calibration curve was carried out to identify the spin speed for samples having thicknesses in the range 300 nm to 10 μm. Samples were left to dry for one day before carrying out the laser ablation experiments.

4.1.3. Agarose film preparation

Agarose biopolymer (A6013-25G, Type I, low EEO) and 50% (v/v) glutaraldehyde were purchased from Sigma-Aldrich. 0.2mg of agarose was placed in 10mL of distilled water and then the mixture was heated to boiling using a microwave for 30 s to get (2% wt./v) concentration of agarose. To fully dissolve the specimen tube (75×25 mm) containing the agarose solution was placed on a hot plate (95°) and stirred for 15 min. 25μL of glutaraldehyde was then added into the solution and continue stirring with a hot plate for

another 15 min. A microscope slides (Thermo scientific) in dimension of (25×75) mm was cleaned and then cut into (25×25) mm to be used as a substrate. The agarose films were spin coated on the cleaned glass by using a spin coater with different speed for 30 s to have film thicknesses in the range of 300 nm to 5 µm. Then produced films were left for 15min to dry. A calibration curved was carried out.

4.1.4. Fabrication of diffraction grating using laser ablation technique

To fabricate the grating in the biocompatible materials films, a parallel bar TEM grid (Agar co, 400 Parallel Bar Nickel 3.05mm diameter: AGG2016N) was used as an object mask to fabricate the grating structure. The grid was placed in the raw beam and positioned to select the most homogeneous part of the beam. The mask was imaged onto the surface of biocompatible materials films using a × 1/5 magnification. The grating was realised on films by translating them line by line using the nano stages (XYZ). The films grating realised by laser ablation was characterised using the following equipments; Optical Microscope (Leica DMLM), White Light Interferometer (WLI, WYKO NT1100), Scanning Electron Microscopy (SEM, Zeiss EVO60) and Atomic Force Microscopy (AFM, Bruker edge). During laser ablation samples were translated relative to the incident laser beam using high precision motion control stages (Aerotech Fibre Align).

4.1.4.1. Laser ablation patterning of microstructure

The mask projection is the method used to fabricate microstructures on the surface of biocompatible materials in this study. Mask projection is a type of laser lithography. The laser beam passes through the parallel bars grid (Agar co, 400 parallel Bar Nickel 3.05mm diameter: AGG2016N). The grid was placed in the mask holder with diameter of 2 mm and projected onto the surface of the biocompatible film by use of an imaging system,

constructed using a set of mirrors and fused silica lens. In the system used, a 5× demagnification was used to reduce the ablated patterns. All biocompatible samples were placed on the holder connected to the XYZ nano-stages. Next all samples were translated relative to the laser beam. After scanning line by line in one direction the sample was rotated and the scanning process was repeated to achieve the square features. The Schematic in figure (4-3) shows the mask projection processing.

Using the mask projection processing has provided many advantages such as [127]:

1- The mask is protected from debris damage.

2- The de-magnification is used with the processing, this means that the laser fluence is higher at the sample than at the mask.

3- Changing the mask is possible, dependent on the applications at hand.

Moreover, producing a microstructure using mask projection can be achieved with different processing techniques [295] such as static ablation, microchannels, curved surface and linear ramps. In this study, the micro channels were fabricated by scanning ablation.

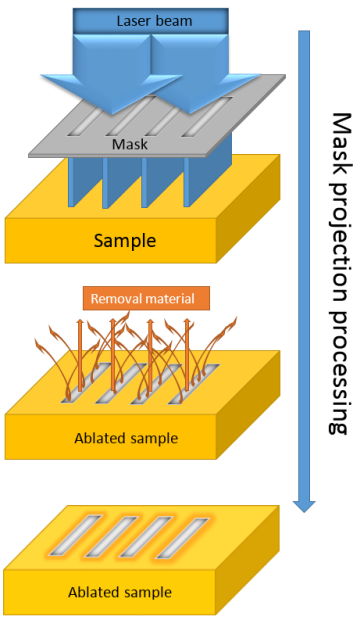

Figure 4-3: Schematic of mask projection processing shows the direct removal material by laser ablation.

4.1.5. Fabrication a diffraction grating using soft-lithography

A transmission diffraction grating with groove density of (1000 grooves mm^{-1}) was purchased form Edmund Optics Co. to be used for the wavelength in the range of 400nm-700nm. It was fabricated using holography technique on a clear polyester film. The preparation of solutions of biocompatible materials chitosan and agarose were discussed in more details previously in this thesis. The polyester card of dimension 50.8 mm^2 was covered with material solutions then the covering films were left for at least three days at room temperature to dry. After that the dried films were peeled off from the polyester films. The grating of 1µm period were replicated in the chitosan and agarose films. The schematic of the imprinting method was used is shown in figure (4-4). The replicated grating was characterized with AFM and WLI.

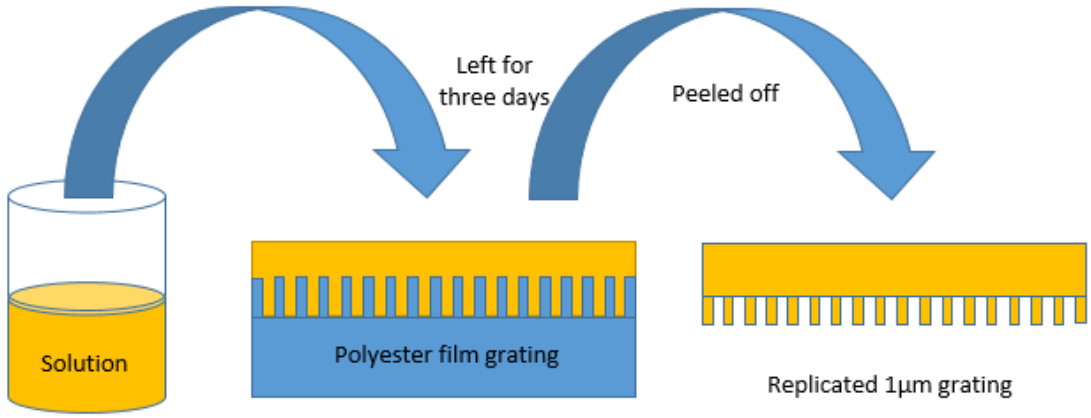

Figure 4-4: Schematic of nano-imprinting technique was used to replicate a grating in period of 1µm in biocompatible material films.

4.1.6. The preparation of PDLC doped dye solution

5CB liquid crystal was obtained from, Kingston Chemicals Limited, the School of the chemistry at the University of Hull. The procedure of 5CB LC doped with chitosan at different ratio has been previously reported [296]. In our work, 5CB LC was doped with chitosan in the ratio of 2:8. 2% (wt. /v) chitosan solution was added into the 5CB LC, the

mixture was then placed on magnetic stirrer plate for 1 hour until the solution became a milky colour. An azo-dye Sudan black B, (SBB) (sigma aldrich, 199664-25G, Lot # MKCD1338) was used to increase the absorption of inscribing laser light. The dye was dissolved in 10 mL of ethanol (0.01mg, 0.02 mg, 0.03 mg, 0.04 mg, 0.05 mg, 1mg, 2 mg) for each mass to obtain different concentrations (0.1, 0.2, 0.3, 0.4, 0.5, 1, 2) % wt./v respectively. The mixture of azo-dye Sudan black B (SBB) in concentrations of 2% within 5CB LC and PDLC 5CB doped with chitosan were studied.

4.1.6.1. Cell preparation

The PDLC doped with SBB dye cells were prepared using two glasses plates coated (25×25×1.1mm) with Indium Tin Oxide (ITO) to form transparent electrodes. The ITO slides were purchased from (delta-technologies, USA, CG-81IN-0115, Polished float glass, The ITO coated surface had an electrical resistance of 30-60 ohms. First of all, the ITO slides were cut into plates with dimensions of (12×25 mm) followed by cleaning. Each cell was prepared by sandwiching them with the PDLC solution doped with dye. The cavity between the two plates was made by using an ultra-thin double sided adhesive tape with a thickness of 5µm obtained from (Nitto co, Nitto Denko UK Ltd). The cell preparation is shown in figure (4-5).

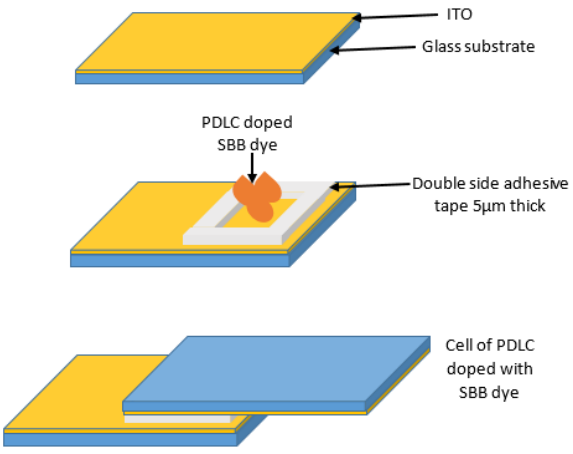

Figure 4-5: The cell structure of PDLC doped with SBB dye.

4.1.6.2. Realisation of the electro optical diffraction grating

The experiment of the inscription of electro optical diffraction gratings were realised using a holographic set up, see figure (4-6). It consists of two HeNe lasers (operating at 632.8 nm), with a maximum power output of 10 mW for the inscribing laser and 1 mW for the probe beam laser. A cubic beam splitter (Thorlabs) was used to split the laser beam into two to create an interference fringes inside the PDLC doped with SBB dye sample. A mirror (Thoralbs, 25 mm diameter) was used to redirect and intersect the converging laser beams. Two linear polarisers were used to obtain a *P*-polarised beams. The sample was placed on mechanical X,Y,Z, stages whose axes were orthogonal so that precise control could be used to create the required interference pattern. A DC power supply was connected to the sample to provide a voltage in the range of (0-30) V. A screen was placed after the sample to monitor the diffraction orders.

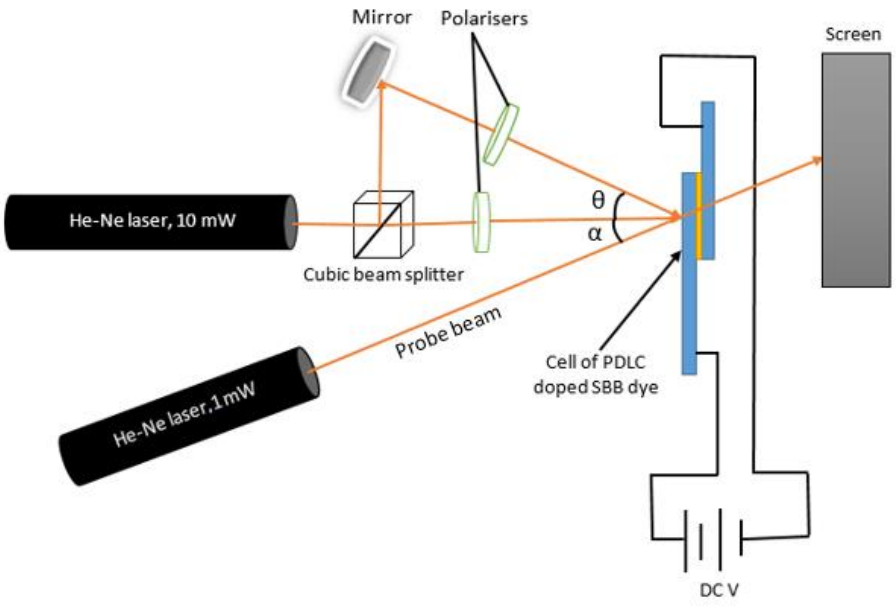

Figure 4-6: The experimental set up for the realization of the electro optical diffraction grating made from a PDLC doped SBB dye.

For the geometry of two beams interference shown in figure (4-6), the period of the interference patterns can be calculated by:

$$d = \frac{\lambda}{2\sin\theta} \tag{4-1}$$

where d is the grating period, λ is the wavelength of light and θ is the angle between two intersecting laser beams. The intersection angle was adjusted to be θ = 1.2° in this experiment. The angle α shown in this schematic is the incident angle of the probe beam on the sample and it is adjusted to be α = 7.2°. From equation 7-5 the grating period produced by interfering beams was calculated to be 15 μm. Cells of 5CB doped with SBB dye and PDLC doped with SBB dye in thickness of 10 μm were illuminated with *P*-polarised writing beams, each beam having a power of approximately 1.8 mW.

CHAPTER 5.

Laser processing results, modelling and discussion

5.1. Laser induced Temperature Rise simulation

5.1.1. Heat transfer

The heat transfer consists of three mechanisms: conduction, convection and radiation. Basically, how hot and cold a material is described by the temperature. The difference in the temperature of the material bodies will lead to the transfer of energy. The transfer of energy can be estimated by the heat transfer [297].

5.1.1.1. Conduction of heat transfer

The processing of generating the heat transfer by the vibration of object molecules are called conduction. During the heat transfer conduction process, the object is not moved. The conduction rate can be given by Fourier's law [298]:

$$q = -kA\nabla T \tag{5-1}$$

Where, q, k, A, ∇T are, heat flow vector (W), thermal conductivity ($Wm^{-1}K^{-1}$), cross sectional area (m^2), and the gradient of temperature (Km^{-1}) respectively.

The gradient of temperature can be described by:

$$\nabla T = \frac{\partial T}{\partial x} i + \frac{\partial T}{\partial y} j + \frac{\partial T}{\partial z} k \tag{5-2}$$

5.1.1.2. Convection of heat transfer

In the convection mechanism, the fluid is needed to transfer the energy between the fluid and the surface. The convection mechanism is explained by Newton's law of cooling [299]:

$$q = hA_s\Delta T \tag{5-3}$$

Where, q is the heat flow from the surface (W), h is the heat transfer coefficient ($Wm^{-2}K^{-1}$), A_s is the surface area (m^2) and ΔT is the difference in temperature between the fluid and the surface.

5.1.1.3. Radiation of heat transfer

In the radiation of heat transfer mechanism, the energy is transferred by the electromagnetic waves. It involves, absorbance, transmittance and reflectance. The radiation mechanism can be described by the concept of emissive power of surface which is given by [300]:

$$E = \sigma\varepsilon T_s^4 \tag{5-4}$$

Where, E, σ, ε, T_s are emissive power, Stefan Boltzmann constant (5.67×10^{-8} $Wm^{-2}K^{-4}$), surface emissivity and absolute temperature respectively.

5.1.2. Heat equation

The heat equation can be given by[301]

$$\frac{\partial T}{\partial t} = \kappa\nabla^2 T + f \tag{5-5}$$

Where, T, t, κ , ∇ and f are the temperature, time, thermal diffusivity, Laplace operator and rate of heating respectively. Both of the distribution of heat and conduction analysis in a specific position can be described by this partial differential equation over time.

In Cartesian coordinate, the heat equation can be written as follow [301]:

$$\frac{\partial}{\partial x}\left(k\frac{\partial T}{\partial x}\right)+\frac{\partial}{\partial y}\left(k\frac{\partial T}{\partial y}\right)+\frac{\partial}{\partial z}\left(k\frac{\partial T}{\partial z}\right)+q^* = \rho c_p\frac{\partial T}{\partial t} \tag{5-6}$$

Where, k, T, q^*, ρ, and c_p are respectively thermal diffusivity (m^2s^{-1}), temperature (K), heat generated per unit volume (Wm^{-3}), density (kgm^{-3}) and specific heat of material

($Jkg^{-1}K^{-1}$). The right term of the last equation describes the change in the thermal energy with time per volume unit. For the time dependent part the heat equation can be written:

$$\rho c_p \frac{\partial T}{\partial t} + \rho c_p u \nabla T + \nabla q = Q + Q_{ted} \tag{5-7}$$

Where, ρ, c_p, q, are material density, heat capacity and heat flow rate respectively.

An important requirement to obtain the solution of heat equation is the boundary conditions. There are three different boundary conditions stated below [301].

Firstly: Constant surface temperature

$$T(0,t) = Ts$$

Secondly: Constant surface heat flux

$$-k \left.\frac{\partial T}{\partial x}\right|_{x=0} = q_{s''}$$

Thirdly: Convection surface condition

$$-k \left.\frac{\partial T}{\partial x}\right|_{x=0} = h\left[\left(T_\infty - T(0,t)\right)\right]$$

Where T_∞ is the convection boundary condition.

This equation has an important applications in probability theory, statistical mechanics, financial mathematics and mathematics. As it is a challenge to find precise solution for this type of equation. Therefore, different methods have been used to solve the heat equation such as Finite Element Method (FEM), Finite Volume Method (FVM) and Finite Difference Method (FDM) [302].The FEM is considered an effective method to solve the heat equation.

An important property of all materials is the thermal diffusivity which is defined as a ratio of the thermal conductivity to the specific heat and density. It can be written as follow [303,304]:

$$D_s = \frac{\kappa}{\rho c_p} \tag{5-8}$$

Where D_s, ρ, κ, c_p and are in order the thermal diffusivity, density, heat capacity and thermal conductivity. It describes the ability of a material to conduct thermal energy relative to its ability to store thermal energy. Materials with large D_s have a quick response to the change in their thermal energy, whereas materials that are slow responding have small D_s therefore, it takes a long time to reach a new condition.

5.1.3. Finite Element Method

Finite Element Method (FEM) is a numerical method to solve Partial Differential Equations (PDE) such as heating equation. Therefore, developing a mathematical model is necessary to describe the behavior of materials in the thermal environment. The model in our simulation contains the heating equation that can be difficult to solve and it is considered as challenging to find a precise solution to this equation. In FEM there are four steps for computational modelling [305]:

Geometry modelling: is the first step to design the geometry structure of the surface.

Meshing: is used to divide the material geometry into a small parts called elements

Material property specifications: is an important step for analysis processing. For example, thermal properties such as thermal conductivity and, specific heat are required for thermal analysis.

Boundary conditions specifications: determination of the boundary conditions are dependent on the type of problem to be solved.

The mechanics and structure for solids heat transfer are most common physical problems solved with FEM.

5.1.4. COMSOL™

In 1986, Mr. Svante Littmark and Mr. Rarhad from Sweden created the first version of COMSOL™ group[306]. Then in 1998 the COMSOL™ group published the first version of COMSOL™ Multiphysics. The COMSOL™ software has been developed in different countries such as United Kingdom, Finland and United states. It is a finite element analysis used for solving and simulating different applications in physics and engineering. In addition, COMSOL™ Multiphysics has several applications such as acoustic model, chemical engineering module, heat transfer model and material library.

COMSOL™ Multiphysics software is used as a Finite Element Method (FEM) to solve the differential equations such as the heat equation. The simulation can be performed in 1D, 2D, 2D axisymmetric and 3D coordinate system [306].

The simulation was performed at 2D axisymmetric with heat transfer model.

The heat transfer model can be ran with stationary and time dependent analysis for 1D, 2D, 2D axisymmetric and 3D coordinate system.

5.2. Results of simulation

Finite Element Method (FEM) using the software COMSOL™ version 5.3 has been used to calculate the temperature rise of laser irradiated biocompatible material the subject of this study. The default solver settings were used for time-dependent heat transfer studies with the exception of the time stepping which was set to strict. This forces the code to solve at each of the manually defined individual time steps with the solver taking any necessary intermediate steps. A triangular mesh was selected and the simulations included temperature dependent properties. The experimentally measured temporal pulse shape (11.5 ns FWHM) was incorporated in the temperature simulations. The COMSOL™ simulation of temperature rise induced by the laser irradiating films are typically depend

on the material parameters, such as heat capacity, thermal diffusivity and absorption coefficient.

5.2.1. The temperature rise of laser irradiated chitosan

For the calculation of the chitosan temperature a three-layer geometry was implemented consisting of air at the front surface of a chitosan sample that was supported on a soda-lime glass substrate. As will be shown the substrate significantly effects the temperature due to heat sink effects.

FEM simulations was run to calculate the temperature rise of chitosan that has been irradiated using a laser fluence of 85 $mJcm^{-2}$ and 760 $mJcm^{-2}$ using COMSOL™ v5.3. The results of the simulation are shown in figures (5-1) and (5-2) for these two laser fluences respectively.

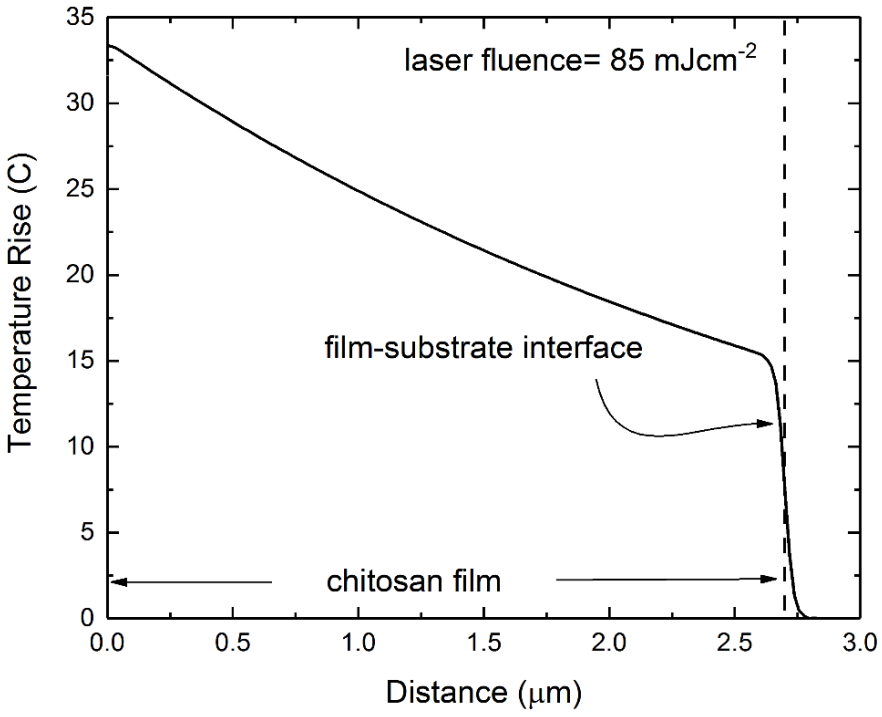

Figure 5-1: Temperature rise simulation using FEM (COMSOL™ v5.3) of irradiated chitosan film at laser fluence 85 $mJcm^{-2}$.

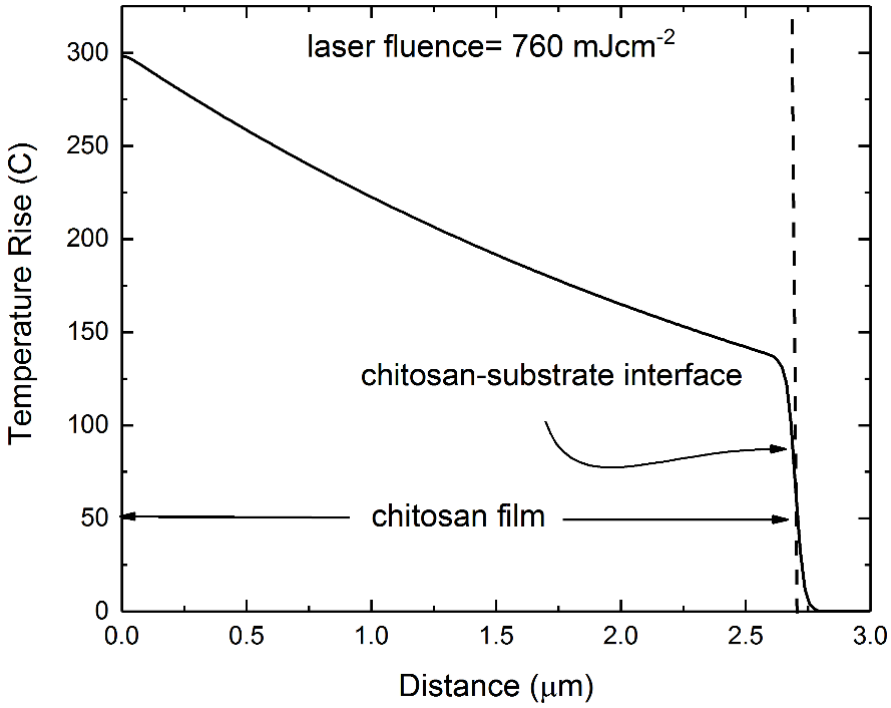

Figure 5-2: Temperature rise simulation using FEM (COMSOL™ v5.3) of irradiated chitosan film at high laser fluence of 760 mJcm^{-2}.

At the lower laser fluence the temperature rise is relatively low, at ~33°C. At a higher laser fluence of 760 mJcm-2 there is a concomitant increase in the temperature rise reaching ~300°C at the front surface of the chitosan. In both cases heat sink effects are observed as heat is being transferred through the glass substrate resulting in a more rapid decrease in the temperature at the chitosan-substrate interface. At the lower fluence the temperature rise is lower than the glass transition of chitosan [307,308] whereas at the higher laser fluence the opposite is true.

5.2.2. Diffraction grating modelling

Diffraction gratings have been used as a tool in optical devices to bend and spread light in devices. Therefore, it is essential to investigate the distribution of the electric field of waves propagating through the diffraction grating of optical components at a range of angles of incident light as this distribution can affect the performance of optical devices. An efficient way to achieve an ideal configuration is the simulation. In our simulation,

wave optics module using COMSOL^{TM} v5.3 was employed to simulate the diffraction gratings that have been fabricated on the biocompatible chitosan films. Floquet boundary conditions were performed in this simulation that allows investigating a single periodic unit cell, as well as a mesh with a fine size, was used to make an accurate simulation. A wavelength of 632.8 nm was used in these calculations.

Figure (5-3, A and B) show the SEM micrograph and the distribution of electric field at 0° of 12 µm of grating fabricated on the chitosan film using mask dragging by ArF excimer laser respectively. The electric field of one unit cell of gratings is shown in this figure B as Floquet boundary conditions were applied. Several parameters could be taken on consideration when the simulation carried out such as the wall of the grooves of the grating and the grating period. It can be observed by figure (5-3, A) that the grating in period of 12 µm made of chitosan film has a relatively well defined walls with some signs to find some texture deposit on the grooves surfaces. These are due to the laser heating during the ablation process. Also, it can be noticed that the grating is periodically which is very important for the grating simulation. For the grating structure made of a periodic slits then each slit is considered as a source of light. These will interfere together to generate the diffraction pattern. Therefore, each slit as a source of light will has an electric filed. ±5 orders of diffraction were monitored and thus because the diffracted angle is relatively small according to the diffraction grating equation. It can be observed in figure (5-3, B) that the electric field is vertical and very uniform. Also, the electric field is more consistent in the centre of the channel.

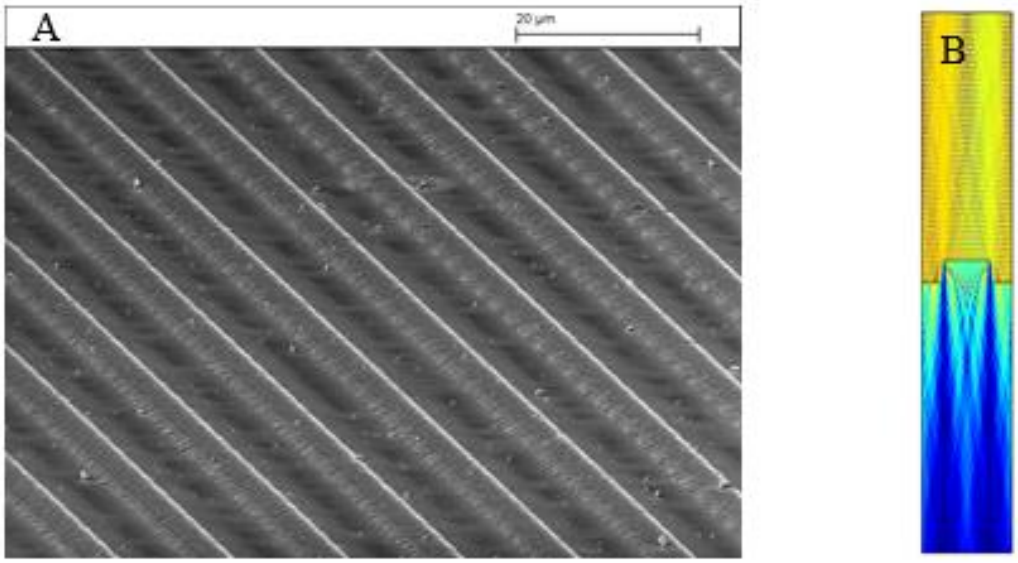

Figure 5-3: (A) 12 µm grating period made of chitosan film and (B) the distribution of electric field of diffraction grating simulated with COMSOL™ v5.3 was calculated using a wavelength of 632.8 nm

Figure (5-4, A and B) show the AFM micrograph and the distribution of electric field at 0° of 1 µm of grating was replicated on the chitosan film using nanoimprinting method respectively. As mentioned above the Floquet boundary conditions were applied to obtain the electric field of one unit cell of the grating which is shown in figure (5-4, B). A well-defined wall of the grating are shown on the AFM micrograph of the grating in figure (5-4, A). Diffraction order ±1 was monitored due to the large diffraction angle of the small grating period. The distribution of the electric field has been changed for the smallest grating period. However, the electric field is still vertical and very uniform also, it is more consistent in the centre of the unit cell.

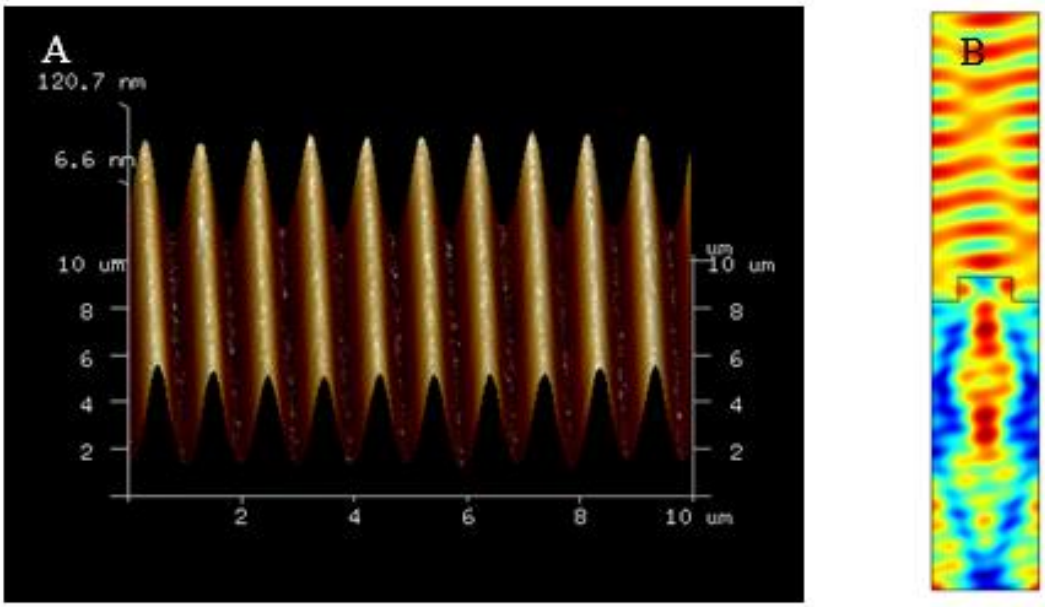

Figure 5-4: (A) 1 µm grating period made of chitosan film and (B) the distribution of electric field of diffraction grating simulated with COMSOL™ v5.3 was calculated using a wavelength of 632.8 nm

Using a simulation to calculate the temperature during laser processing gives useful information for understanding the ablation processing. The materials under laser irradiation are heated from room temperature up to a high temperature at which the degradation point occurs for the biocompatible materials. Depending on the laser fluence and material properties, the biocompatible materials are degraded by additional heating until it reaches the degradation point. Therefore, ablating samples below the decomposition temperature of the material is important for un-irradiated parts of a sample to avoid any chemical changes which may occur above this temperature in the laser ablated regions. For simulated materials, chitosan the decomposition temperatures were obtained from Thermo-Gravimetric Analysis (TGA), the measurements is 298°C (discussed later in this thesis). Using the simulation the temperature composition of chitosan was calculated corresponding to laser fluences of 85 $mJcm^{-2}$ and 760 $mJcm^{-2}$ respectively. Therefore, the relatively low laser fluence was employed for grating fabrication, assuming there is no shielding of the incident laser pulse by the ejected laser

ablation products. From this knowledge, the laser fluences was used to form the grating of the chitosan film is 110 $mJcm^{-2}$. Modelling the diffraction grating allows us to observe the uniformity of the electric field of the laser passing through the grating. It is also showing us the effect of the grating parameters, such as the etch depth and the period on the electric field distribution. Therefore, any change to one or all of these parameters leads to more optimization. The effect of the grating period on the electric field distribution can be seen in figure 5-3B and 5-4B. Knowing the distribution of the electric field propagating in the grating allows us to determine the most efficient period that can be employed before designing the grating devices.

5.3. Results of laser ablation of biocompatible materials

The laser ablation of biocompatible chitosan film using ArF excimer laser is investigated. Realisation of diffraction gratings made of biocompatible materials; chitosan and agarose using different technique also have been investigated. Before these investigations, all materials films were optically characterised. Also, these materials were characterised using Thermo-gravimetric analysis (TGA). Laser beam charactarisation has been reported in this section.

5.3.1. Chitosan

Usually in nature chitosan can be found as chitin. There are many natural produced of chitin [309], however, each one has a different amount of chitin. For example, the proportion of chitin in shrimp and crab is 58% and 85% respectively, while, it is about 20% and 60% respectively in mosquito and butterfly, as well as this some parts of animals contain chitin e.g. in hoofs and feet. Chitosan is derived from Chitin in the form of Deacetylation Degree (DD) [310], others use the degree of acetylation ($DA = 100 - DD$) [311]. Deacetylation means removing an acetyl from chitin, by deacetylation, chitosan are considered as a chitin family [312]. The chitin becomes a soluble in a dilute acid and

is called chitosan when the deacetylation degree is over of 60% [309]. The deacetylation degree can be defined by [311]:

$$DD = 100 \frac{n_{GleN}}{n_{GleN} + n_{GneAc}} \tag{5-9}$$

Where, n_{GleN} is the average number of D-glucosamine units, and n_{GneAc} is the average number of N-acetylglucosamine units. The chitosan is a copolymer of D-glucosamine and N-acetylglucosamine [313]. Therefore, from equation (5-9), the DD is a ratio between the D-glucosamine units and N-acetylglucosamine units. Figure (5-5) shows the chemical structure of chitosan [313], it appears as a straight chain copolymer, therefore, it is a semi crystalline polymer in the solid state.

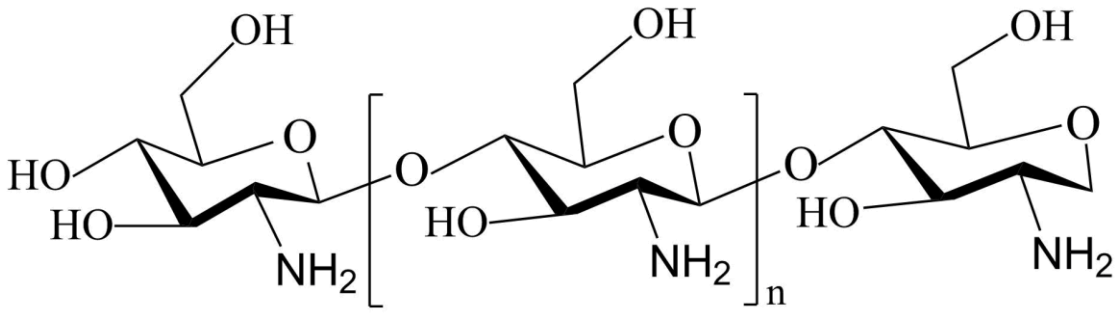

Figure 5-5: Chitosan chemical structure.NH_2 group is shown in the chitosan chemical structure produced by using chem. Office.

Figure (5-5) shows that the chitosan contains a NH_2 functional groups and these functional groups give chitosan their exclusive properties that are used in medical and pharmaceutical applications [312].These unique properties such as biocompatibility, biodegradability and non-toxicity [314], which make it suitable for applications in the biomedical field. In addition, chitosan has the following chemical properties; linear polyamine, reactive amino groups, reactive hydroxyl groups available and chelates many transitional metal ions [314]. There are different mechanisms of structural degradation. For example, oxidative, hydrolytic, thermo-photo and ultrasonic degradation are responsive to chitosan [3]. Moreover, chitosan has an active surface for the chemical

reactions such as the photochemical reaction, this surface has considerable importance for these reactions because it has an NH_2 group [314] as has been mentioned before, it is a positive group. These groups give the chitosan films their special properties which allows chitosan to be suitable for many reactions including biological reactions that occur on the chitosan surface [3].

5.3.1.1. Chitosan production

Two methods are used to produce chitosan [309], chemical method and enzyme method. Figure (5-6) below shows the chemical equation to produce the chitosan by removing acetyls from chitin by base of hydrolysis of chitin. From this equation it can be observed that the function of NaOH concentration is playing an important role in the deacetylation processing as well as the time of reaction and temperature [315], and these factors affect the chitosan performance.

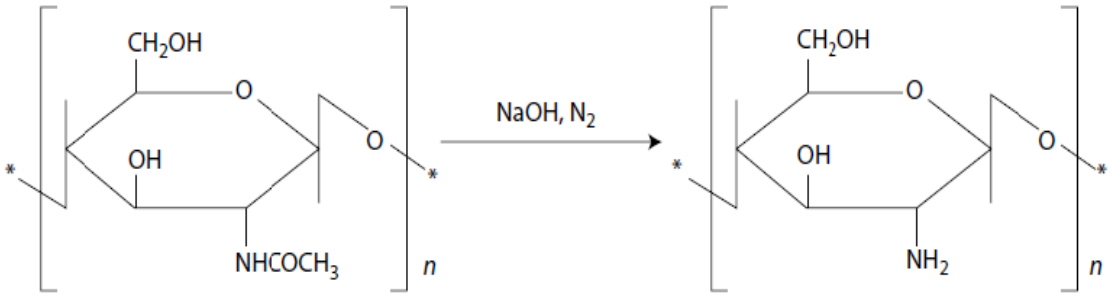

Figure 5-6: Chemical equation of chitosan preparation by base of hydrolysis of chitin

Chemical methods have been used to prepare chitosan and it involves several methods; the Alkali fusion method, the concentrated alkali solution method, the alkali catalysis method and the hydrazine hydrate method [309]. The preparation process to get the chitosan from shrimp and crab by chemical method is shown by figure (5-7).

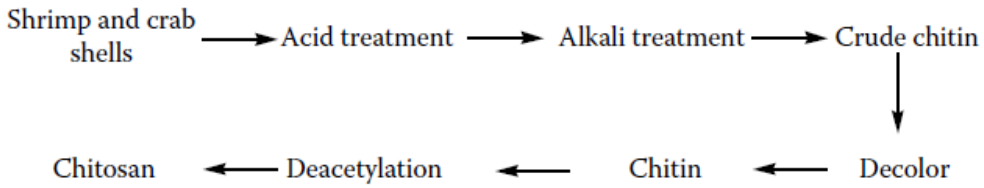

Figure 5-7: The chemical method for chitosan preparation from shrimp and crab shells.

Three solvents can be used in the deacetylation process; acetone, ethanol and water [309]. The DD will be higher with acetone, and the chitosan will be yellowish and you can have difficulty in washing a product. However, using water as a medium of reaction will cause a low DD especially when the temperature reaches 80°C and washing the product will be hard. Consequently, for deacetylation, ethanol is considered as the best medium between them. After production processing chitosan has a solubility in different chemical materials. For example, an organic solvent, alkali, acid at a high concentration, chitosan is insoluble [315], while, Chitosan has a good solubility in water when the DD is 50% [1,2]. In addition, chitosan becomes a modifiable polymer by reaction between the hydroxyl and the amino group [316]. Chitosan can accept a wide range of groups to offer a specific functionality, biological and physical properties. Different examples for reaction modifications [317]; acylation, hydrolysis, alkylation, acetylation. In the last few decades, several techniques have been developed to prepare chitosan microspheres, but the more recent one is spray drying[318].

5.3.2. Agarose

Agarose is considered as a biocompatible material extracted from agar; it is a natural and linear polysaccharide composed of (1,3) linked β-D-galactose (G), and (1,4) linked α-L-3, 6- anhydrogalactose (A) [319,320]. Figure (5-8) below shows the chemical structure of agarose.

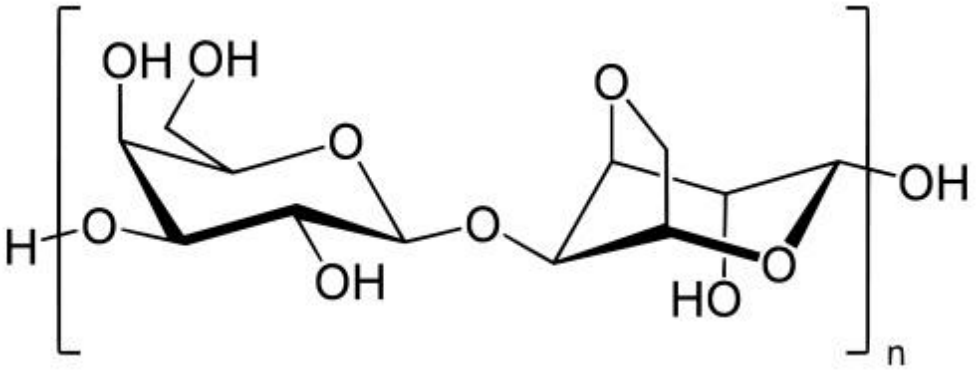

Figure 5-8: Agarose chemical structure produced by using chem. office.

Agarose hydrogel compounds can be easily molded into a microscale structure due to their strong structure [102]. The important properties of agarose are strongly hydrophilic, chemical inert, a resistant material of microbiologically [321]. Also, the agarose in the gel form is quite stable in affinity chromatography [322]. Different methods have been used to activate the agarose including allylbromide [323], Cyanogen bromide [324].Agarose as a natural hydrogel provides various properties including; fully non-cytotoxic, transparent, thermosensitivity as well as it is considered as a soft and non-adhesive material. Agarose as a biocompatible material has been employed to be used in a wide range of applications; it has been utilized as a substrate for the cell culture in the 3D micropatterning application [17], humidity sensing [325] and 3D cell migration [326]. In addition, agarose was used for pH optical sensor preparation [16,18,321,327], Optical waveguide fabrication [102] and for the microfluidics devices lab on chip [328]. It is also used in the fabrication of polymer microarrays [329].

5.3.3. Argon fluoride laser (ArF) 193 nm

The ArF laser is a type of excimer laser consisting of mixture of noble gas argon and halogen gas. Table (5-1) below shows all characteristics for UV ArF laser 193 nm which have been used in this work.

Table 5-1: characteristics of UV ArF laser 193 nm (Lambda Physik, LPF202)

Property	Value
Wavelength	193 nm
Pulse energy	(6.7-285) mJ
Pulse duration	11.5 ns
Average power (at 20 Hz)	5700 mW
Repetition rate	(1-20) Hz
Charge voltage	(19-26) kV

5.3.3.1. Beam characterization

The characteristics of the radiation emitted from excimer lasers such as, energy pulse, beam width, divergence, pointing stability and uniformity [210] even more a high stability and the controlling is very accurate over these characteristics are making them to be used in many applications. As an example, figure (5-9) illustrates the near field is recorded for ArF excimer laser (193 nm) (Novaline, lambda Physik). Both smooth and symmetric profile are indicated. The dimensional energy density distribution can be used to evaluate beam parameters. The temporal pulse shape of laser ArF laser 193 nm (Lambda Physik LPF 202) is shown in figure (5-10). The data was obtained using a fast photo diode (Hamamatsu, S7911) connected to an oscilloscope (Infinium, 500 MHz, 2 Gb Samples s^{-1}). The figure illustrates that the Full Width Half Maximum (FWHM, τ) is 11.5 ns of the laser

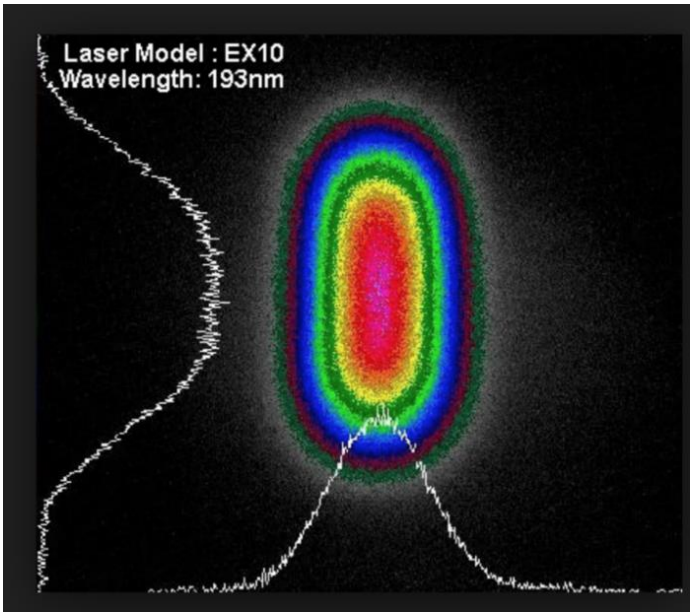

Figure 5-9: Near field profile of ArF (193nm) [210].

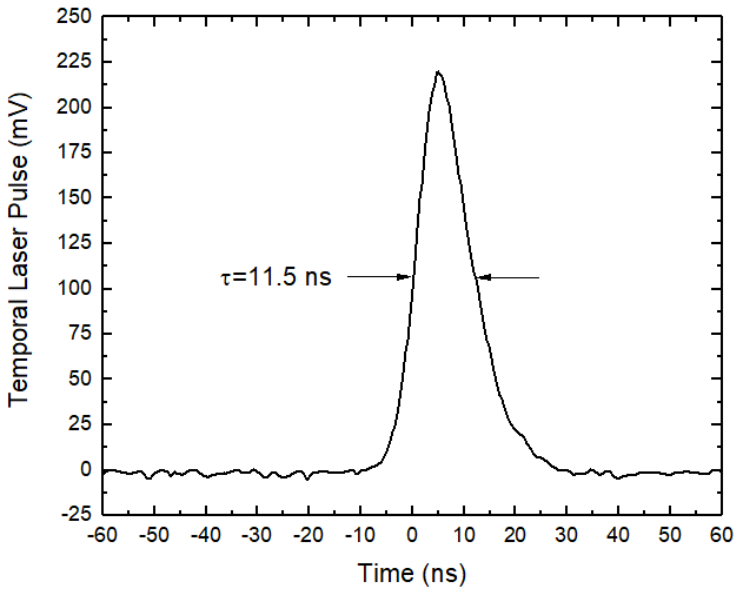

Figure 5-10: Pulse shape of ArF laser 193 nm. The data was obtained using a fast photo diode (Hamamatsu, S7911).

. Figure (5-11) depicts Raw Beam Energy of laser 193 nm induced that the beam energy of laser increased gradually with increasing charging voltage. However, at a higher charging voltage the energy of laser tends to be more stable. The pulse energy depends on the repetition rate of laser [209].

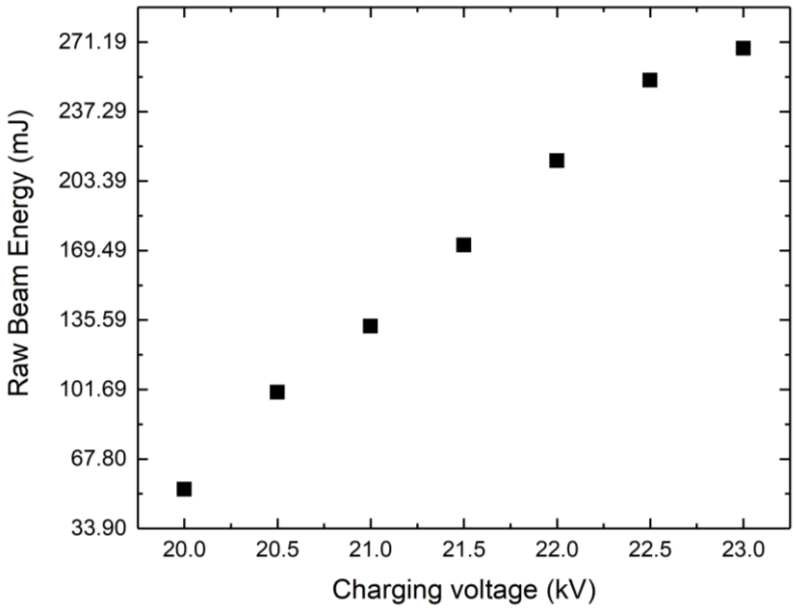

Figure 5-11: Raw Beam Energy of ArF laser 193 nm.

Laser fluence of laser 193 nm is shown by figure (5-12) as a function of charging voltage, which is represents the dependence of laser fluence on the repetition rate. As can be seen from figure, increasing repetition rate effects the fluence to be lower at a higher repetition rate.

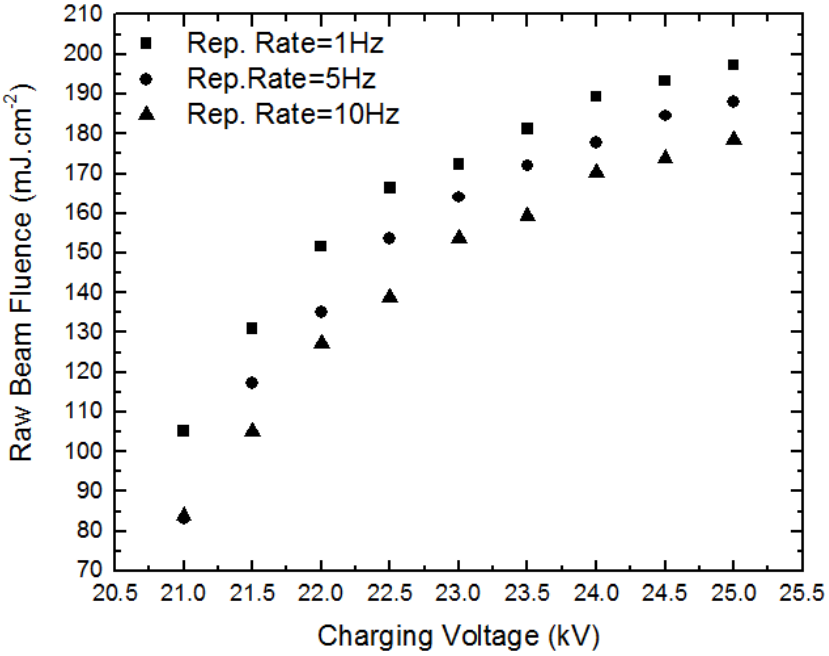

Figure 5-12: Laser beam fluence of ArF laser 193 nm at a different repetition rate(1 Hz,5 Hz, 10 Hz).

5.3.4. UV-VIS measurements

UV-VIS absorption measurements were carried out on dried biocompatible material films under study and chitosan solutions at different concentrations by using Thermo scientific UV-VIS spectrophotometer evolution 220.

5.3.4.1. Absorption coefficient

The absorption coefficient is a very important factor in light–matter interaction, it is used to determine how far the exact wavelength infiltrates into a material before light is absorbed. The Lambert-Beer law explains the intensity of beam of light when it is incident on a material [330]:

$$I = I_0 \exp(-\alpha d) \tag{5-10}$$

Where I, I_0 are the collected light intensity and the incident light intensity, respectively, d the thickness of material and α is the absorption coefficient. The absorption coefficient can be calculated by using the equation [331]:

$$\alpha = -\frac{1}{d}\ln\left[\frac{I}{I_0}\right] \tag{5-11}$$

In the intermediate region ($10^2 cm^{-1} < \alpha < 10^4 cm^{-1}$) the absorption coefficient can be determined as a function of frequency, in this case the absorption coefficient can be given as fellow[332]:

$$\alpha = \frac{1}{d}\ln\left[\frac{(1-R)^2}{2T} + \sqrt{\frac{(1-R)^4}{4T^2} + R^2}\right] \tag{5-12}$$

Where R, T are the reflection and transmission of material respectively at each frequency and d the thickness of the material. Generally, the absorption coefficient depends on the material and on the wavelength of light which is absorbed by the material. The Beer's law indicates the absorbance of material is proportional increases with increasing the film thickness [149,200].

$$\alpha = \frac{2.303A}{d} \tag{5-13}$$

Where, the absorbance, absorption coefficient, and the film thickness are represented by *A*, α and *d* respectively. The last equation was used to calculate the absorption coefficient of all biocompatible materials under study.

Figure (5-13) below shows an average of five absorption measurements of chitosan films for 2% concentration (w/v) of chitosan mixed with acetic acid.

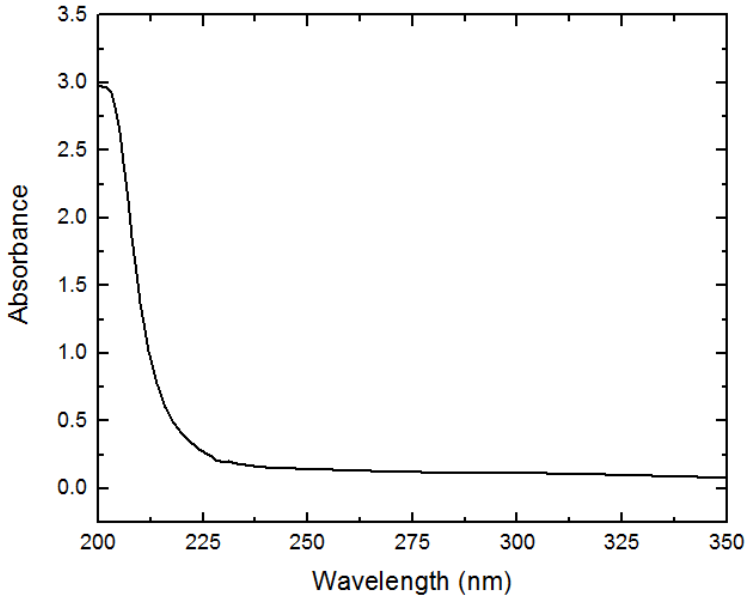

Figure 5-13: The UV-Vis spectrum of 2% (wt. /v) chitosan film.

As can be seen the absorption increases towards the UV spectral region. The spectra indicate that chitosan thin films are optically transparent over a broad range of the visible spectrum. At shorter wavelengths, around 225 nm the optical absorption increases rapidly. From these measurements, an average absorption coefficient of $\alpha_{Spec} = 3.0 \pm 0.3 \times 10^3\,\text{cm}^{-1}$ was determined. In many applications, it is prudent to minimise thermal damage induced during laser processing. Therefore it is important to select a low laser fluence to avoid damage to the surrounding material. Another graph of chitosan absorbance at the UV-VIS range is shown by figure (5-14) below:

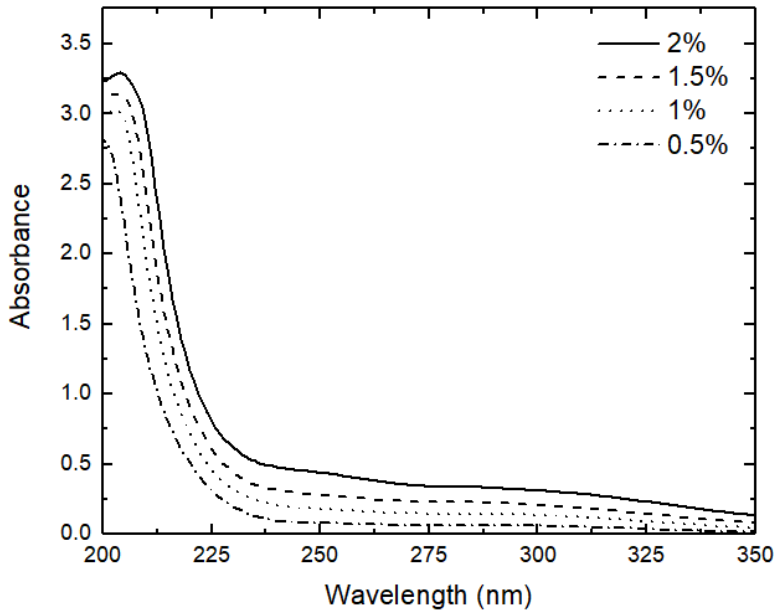

Figure 5-14: The UV-VIS spectrum of chitosan at different concentration.

Further study was done by preparing four different concentration of chitosan (0.5%, 1%, 1.5%, 2%) (wt. /v) by adding a chitosan weights of (0.5, 1, 1.5, 2) mg into 10 mL of acetic acid. This study was run to investigate the effect of concentration on the absorbance behave of chitosan solution. It can be noticed from the graph and according to the Beer's law that the absorbance increases in the direction of the UV range but also decreasing slightly with lower concentration. Another set of UV-VIS measurement is shown by figure (5-15) below to investigate the behavior of the absorbance of chitosan film spin coated with time. The 2% of chitosan solution was prepared and then spin coated into a fused silica plate (Airekacells co.) with 250 rpm to achieve an average chitosan film thickness of 8.6 µm. The absorbance was measured three times with thickness measurement by the WLI for each time. The film thicknesses for the first day, one week and two weeks after were in the average of 8.6 µm, 7.4 µm and 7.2 µm respectively. It can be noticed from the figure (5-15) that the absorbance of chitosan film is decreasing with the time for a very small range of the UV wavelengths ~ (200-205) nm whereas, no change can be seen in the absorbance for the rest of UV-VIS range. This is evidence of

shrinking the chitosan film with time and that observed by decreasing in the film thickness. According to the Beer's law, the absorbance decreases or increases proportionally with the film thickness. Therefore, a difference in the absorbance is observed for all thicknesses however, it is less between second and third spectrum due to the small difference in the thickness.

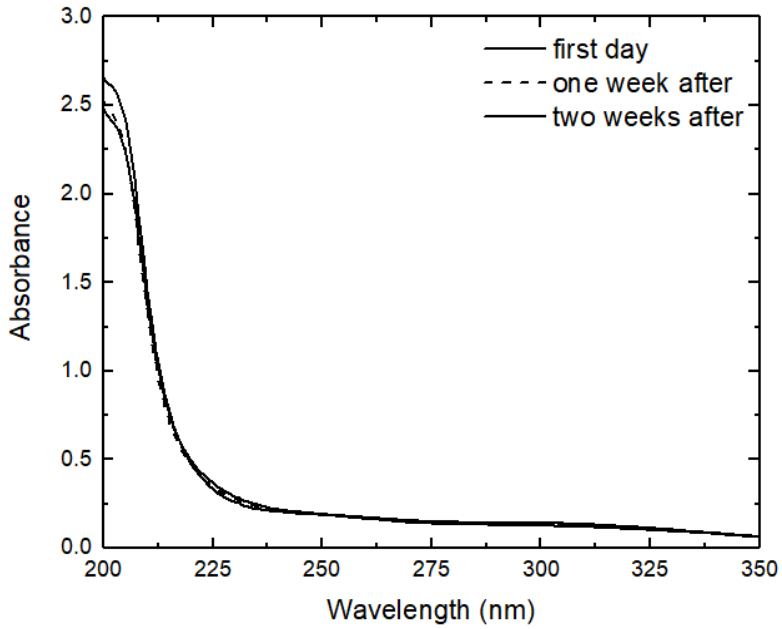

Figure 5-15: UV-VIS spectrum of 2% (wt. /v) chitosan film at different time.

It is noticed that the thermal diffusivity of chitosan is low and heat flow is of the order of $L_H = 4\sqrt{\chi \tau_P} = 120$ nm.

Figure (5-16) illustrates the absorption spectrum of the biocompatible agarose free standing film in thickness of 32 µm. The thickness was measured using a Dektak (Bruker). The absorbance curve shows that for long wavelengths > 300 nm there is approximately no light absorbed because most of light is transmitted. While for wavelength < 300 light absorbance starts to increase sharply to reach the maximum value in the very deep UV wavelength. Therefore, in the deep UV wavelength the light is nearly totally absorbed and there is no transmitted light.

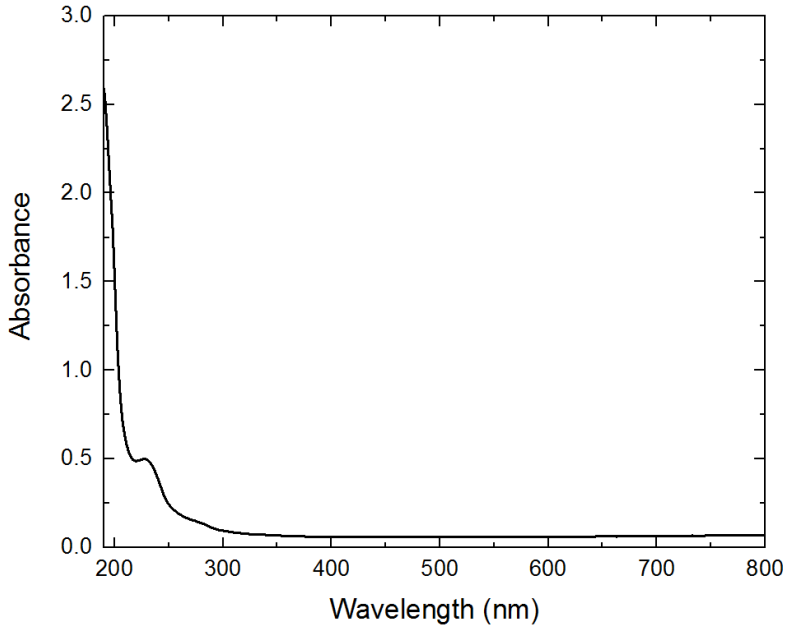

Figure 5-16: UV-VIS spectrum of 2% (wt. /v) agarose film.

Figure (5-17) below are displaying the ultraviolet absorption coefficient spectra of biocompatible materials agarose. Spectra was calculated using the absorption data with applying the equation (5-13). The absorption coefficient of agarose was calculated at the wavelength of 193 nm to be 1.67×10^{3} cm^{-1}. The absorption in the UV wavelength was discussed in terms of one photon processing and small amount of absorbing photon [66].

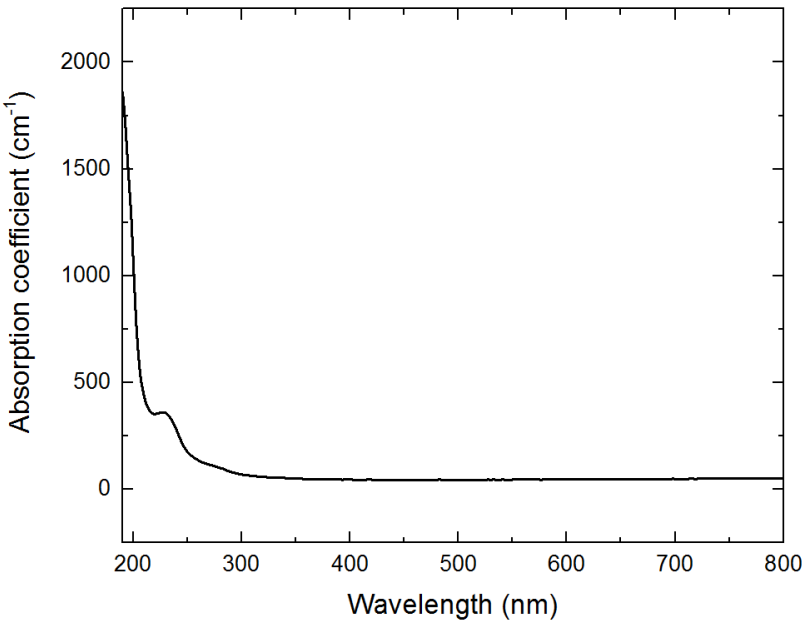

Figure 5-17: The absorption coefficient of 2% (wt. /v) agarose film was calculated using the absorption spectrum data.

5.3.5. Thermo-Gravimetric analyses (TGA)

The Thermogravimetric Analysis (TGA) is a technique that measures the change in weight of a sample as it is heated with a constant heating rate. The main purpose of using TGA is to characterize materials with respect to their composition. Thermogravimetric analyses (TGA) in this work were performed in a flowing nitrogen atmosphere on a PerkinElmer (TGA 4000) Co., Ltd. thermogravimetric Thermoflex system, using 2-3 mg of specimen. The temperature was raised to 600°C at a heating rate of 20°C/min. The degree of decomposition in the TGA can be calculated by [333].

$$X = \frac{W_0 - W_t}{W_0 - W_f} \tag{5-14}$$

Where, the degree of decomposition, the actual, initial and final mass of material are represented by X, W_0, W_t and W_f respectively. The expression below describes the model of kinetic process of the thermal degradation [334]:

$$\frac{d\alpha}{dt} = k(T) f(\alpha) \tag{5-15}$$

Where, the time, conversion degree, temperature, the rate constant of the temperature dependent and the function of temperature dependent are donated by $t, \alpha, k(T)$ and $f(\alpha)$ respectively. The rate constant of temperature dependent $k(T)$ can be described by the Arrhenius equation:

$$k(T) = A\exp\left(-\frac{E_a}{RT}\right) \tag{5-16}$$

Where, A, E_a, R and T represent in order, the frequency factor, activation energy, gas constant and temperature. Then the equation (5-25) can be rewritten as follows:

$$\frac{d\alpha}{dt} = A\exp\left(-\frac{E_a}{RT}\right) f(\alpha) \tag{5-17}$$

The difference in the decomposition degree can be expressed as a function of temperature when the temperature has changed with constant value $B = \frac{dT}{dt}$, then the decomposition degree equation can be written as:

$$\frac{d\alpha}{dt} = \frac{A}{B}\exp\left(-\frac{E_a}{RT}\right)f(\alpha) \qquad (5\text{-}18)$$

The last two equations are considered as the basic of the kinetic calculations. The TGA measurements for these works were completed in order to further investigate the results of surface modification and an attention has been turned out to the decomposition of chitosan. As was expected decomposition temperature and glass transition temperature may dependent on the rate that energy is transferred and the type of solvent and the concentration [335,336]. A small sample of chitosan was prepared under the same conditions as those samples used for ablation studies.

Two samples of chitosan in two different concentrations 2% and 2.5% (w/v) were used to measure the decomposition temperature using a thermo-gravimetric analysis (TGA). The preparation of chitosan solution was discussed in this thesis previously. Then solutions were poured in the dishes and left at room temperature for three days to produce a free standing film. The results of TGA are shown in Figures (5-18) and (5-19) below. It can be observed from the derivative that a peak representing a maximum decomposition rate occurring at a decomposition temperature $T_d = 300\,°\text{C}$ in both graphs. From these two graphs it can be deduced that the decomposition temperature is not effected by the concentration of chitosan. A careful study has been reported by *Sakurai, et-al,* on the glass decomposition temperature of chitosan reporting a glass transition temperature for chitosan of $T_g = 203\,°\text{C}$ [308]. Similarly, *Dong et-al*, have used four techniques to

measure the glass transition temperature of chitosan and a glass transition temperature has been reported in the range of $T_g = 140 - 150\,°\text{C}$.

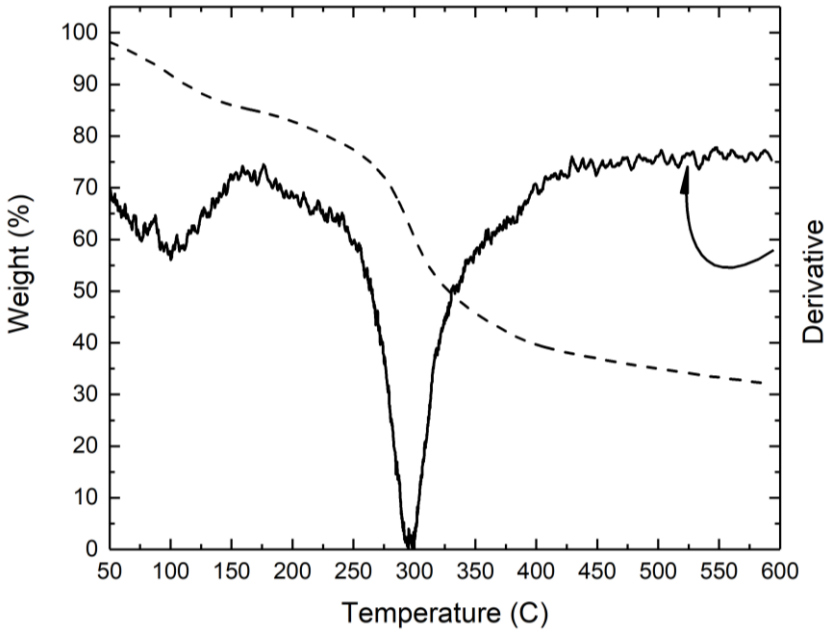

Figure 5-18: Thermo- Gravimetric Analysis (TGA) of 2% (w/v) chitosan in acetic acid. The dotted line is the TGA measurement and the solid line is the derivative of the measurement. Maximum mass transport is seen to occur at a temperature of 300 °C.

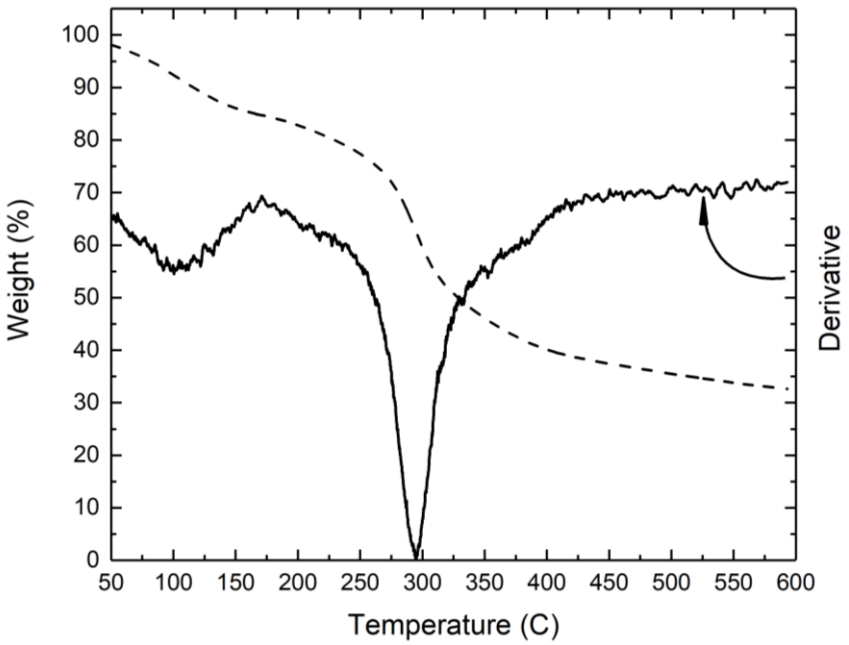

Figure 5-19: Thermo- Gravimetric Analysis (TGA) of 2.5% (w/v) chitosan in acetic acid. The dotted line is the TGA measurement and the solid line is the derivative of the measurement. Maximum mass transport is seen to occur at a temperature of 300 °C.

The TGA measurement of 2% (wt. /v) agarose is shown in figure (5-20). TGA measurements of agarose were carried out using the temperature in the range of 50°C to 600°C at a heating rate of 20°C min^{-1} in a nitrogen atmosphere, using sample mass of approximately 3 mg. The thermal decomposition was determined by TGA using derivative of the baseline of the weight loss of sample. It can be concluded that the thermal decomposition of biocompatible agarose 2% occurs at approximately 285°C. The weight loss of agarose can be divided into three stages. In the first stage, the agarose sample starts slowly losing 20% of the weight in the temperature between 50°C and 265°C. While, in the second stage a 75% of the sample weight was lost rapidly in the temperature between 265°C and 450°C. Then, in the third stage, the sample weight is back again to be lost slowly in the range of 450°C to 600°C. The major loss of agarose weight was reported to be between 270°C and 330C [337]. As the base of the agarose is water, therefore the first stage of losing weight of the sample is due to loss the water. While the second stage is donated to the agarose degradation.

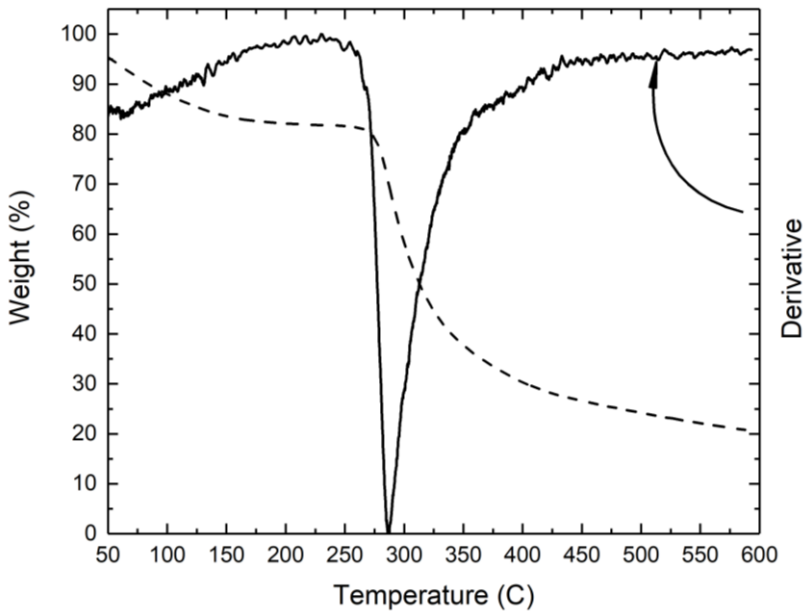

Figure 5-20: Thermo- Gravimetric Analysis (TGA) of 2% (w/v) agarose in water. The dotted line is the TGA measurement and the solid line is the derivative of the measurement. Maximum mass transport is seen to occur at a temperature of ~ 285 °C.

5.3.6. Laser ablation of chitosan thin films

Etch rate measurements have been carried out to determine the laser ablation threshold, F_T, and the results are shown in Fig (5-21) below:

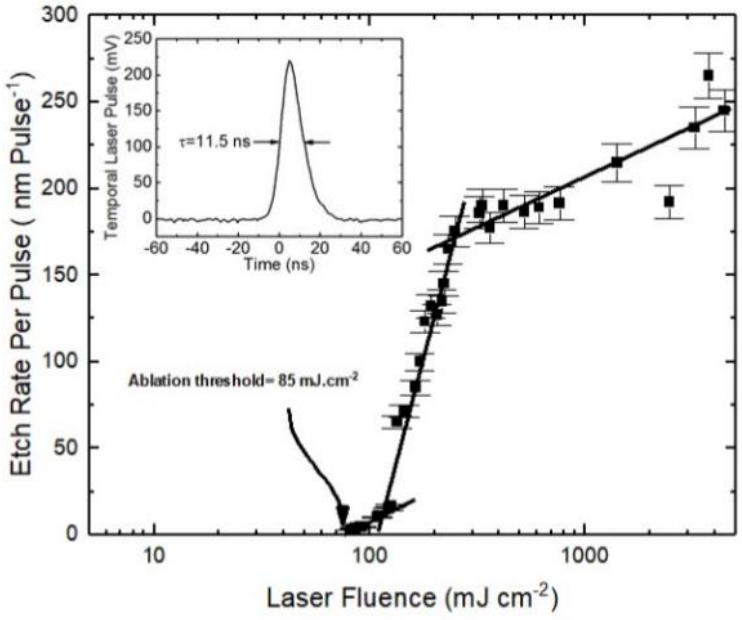

Figure 5-21: The laser ablation threshold data of chitosan film in a thickness of 2.7 microns and it indicates that the F_{th} to be 85 mJcm^{-2}. The inset shows the laser pulse of 193nm laser has been used in these experiments

A set of experiments were conducted over a laser fluence between 70 mJcm^{-2} to a maximum of 4.5 Jcm^{-2}. A WLI was used to establish the etch depths measurements by measuring the depths of the ablation craters. An ablation threshold of $F_T = 85 \pm 8$ mJcm^{-2} was determined from these measurements. Ablation etch rates close to F_T be relatively low at a nanometer per pulse level. At the higher laser fluence the etch rates were beginning to plateau. This can be assigned to several effects, photon shielding by ablation products, surface re-structuring causing the effective surface area to increase. It is suggested that the effective surface area increases as laser driven acoustic wave induces tensile stresses and bubbles nucleate modifying the surface topology. Photo acoustic studies of tissue ablation have been previously reported [338,339]. In some cases laser

ablation has resulted in the formation of bubbles and foaming at the surface of the irradiated site [36,247,340]. The experimentally determined ablation threshold was compared with a simple thermal energy balance equation:

$$\alpha A F_{evap} = \rho\left[C\left(T_b - T_0\right) + L_v\right] \tag{5-19}$$

where, C is the specific heat capacity, T_b and T_0 are the boiling temperature and initial temperature respectively, ρ is the density and L_v is the latent heat of vaporisation. Using the corresponding values a laser ablation threshold of $F_{evap} = 900$ mJcm^{-2} is calculated [340][6]. This is close to a tenfold higher value of the ablation threshold compared with etch rate experiments. From this calculation and from SEM measurements of the ablated chitosan samples presented here prompts one to investigate alternative ablation mechanisms to describe the ablation process.

The photoacoustic (PA) mechanism can play a significant role in laser ablation especially in polymeric materials and biological tissue [247,257]. Figure (5-22) shows an SEM micrograph of a circular ablation crater that was produced by applying a laser fluence of 125 mJcm^{-2}. This fluence is above but close to the ablation threshold and one observes localised blistering on the surface. Figure (5-23) shows a magnified image of the blistered region. The blistering is suggestive of sub-surface volumetric expansion due to gaseous species expanding from beneath the surface. In an attempt to select a uniform photon flux a circular object mask, 2 mm diameter was positioned centrally in the Hermite-Gaussian beam of the ArF laser beam. We suggest two possibilities for the appearance of localised blistering. Random, spatially distributed intensity fluctuations within the beam can occur [341].

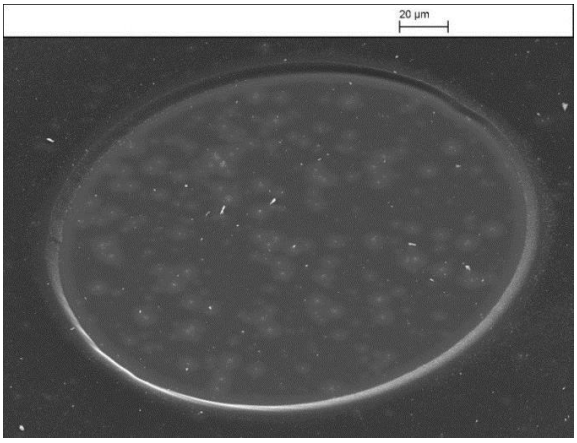

Figure 5-22: SEM image of chitosan thin film in thickness of 2.7 µm irradiated with 193 nm laser, imaged in 10 × magnification, repetition rate 1 Hz, 10 laser pulses, laser fluence 125 $mJcm^{-2}$, depth 16.6 nm per pulse, circle mask in size of 2 mm, tilt angle 45° and at a magnification of 1.6k.

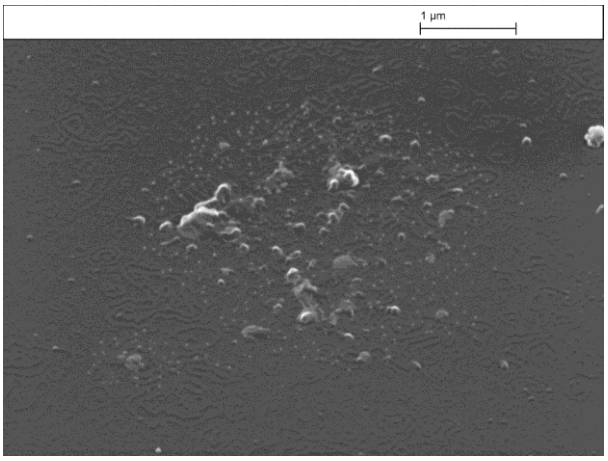

Figure 5-23: SEM micrograph of the center of above crater under the same parameters but at 60k magnification.

These intensity fluctuations will manifest in hot spots within the beam that are projected onto the near surface of the sample. The influence of hot spots may heat the chitosan at the surface and down the optical absorption depth α^{-1} and the hot spots may drive gaseous expansion. An alternative description may be due to incomplete mixing of the solvent during the sample preparation stage which may introduce different degrees of optical absorption. Similarly, a combination of these two effects could exist. However, to gain a deeper understanding of the mechanism associated with blistering requires further work. Figure (5-24) shows an ablation site under the same imaging condition as the previous results but at an increased laser fluence of $250\ mJcm^{-2}$

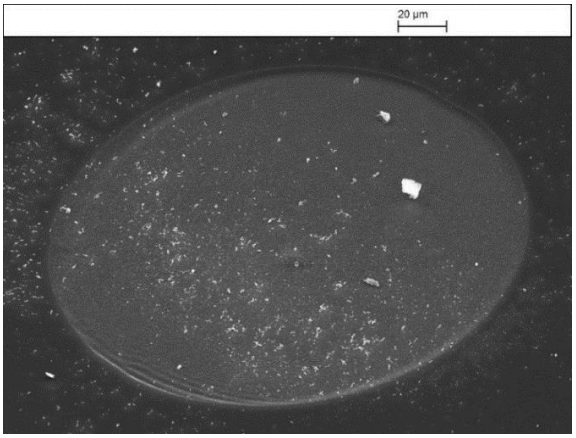

Figure 5-24: SEM image of chitosan thin film in thickness of 2.7 µm irradiated with 193 nm laser, imaged in 10 × magnification, repetition rate 1 Hz,10 laser pulses, laser fluence 250 mJcm^{-2}, depth 175 nm per pulse, circle mask of 2 mm diameter, 45° tilt angle, 1.6 k × magnification.

The surface topology has changed significantly from the lower laser fluence. Figure (5-25) shows an SEM of a magnified region within the floor of the same crater. Evidence of foaming is seen to be growing from the near surface. Foaming has been reported to occur during laser ablation of collagen using a KrF laser emitting at a wavelength of 248 nm [247]. Foaming of collagen was described in terms of cavitation effects induced by photo-acoustic stresses.

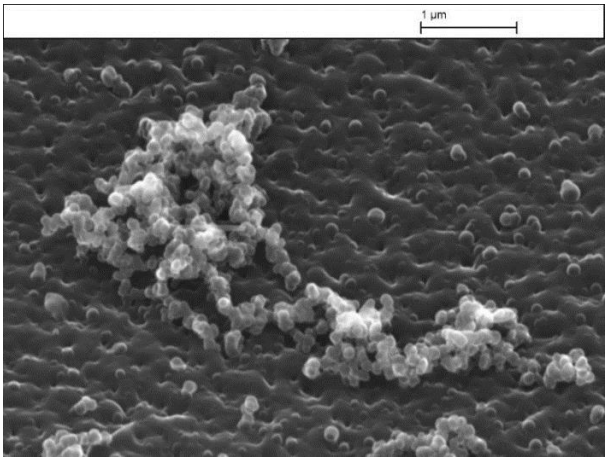

Figure 5-25: SEM micrograph of the Centre of the laser ablation crater in figure 24 but at 60k×magnification.

In the results presented in this work the regions of localised foaming consist of spherical globules that appear to be penetrating the surface of the chitosan. The formation of

spherical features and the nucleation of bubbles is suggestive of tensile stresses causing voids within the chitosan. One more evidence of chitosan foaming is shown by figure (5-26). It is a SEM image of the centre of crater of chitosan film was irradiated with laser fluence of 175 mJcm^{-2}. It is very clear that nucleation bubbles growth on the surface.

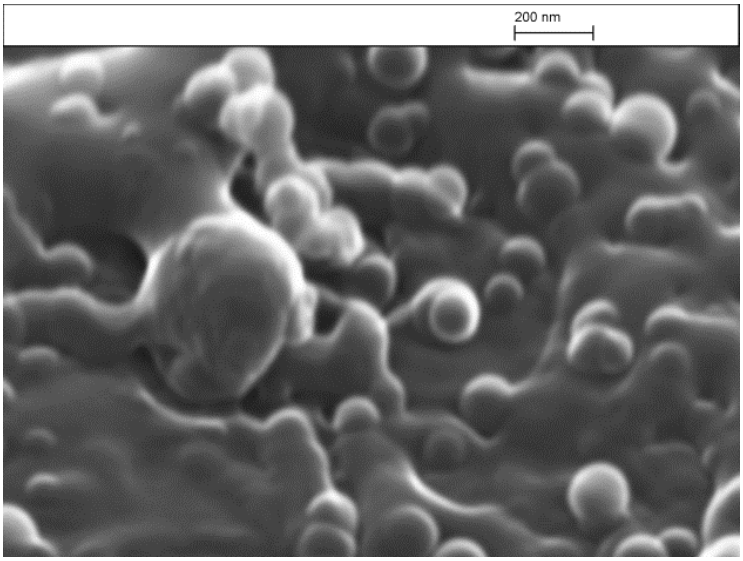

Figure 5-26: SEM image of the centre of crater of chitosan thin film irradiated with 193 nm laser, imaged in 10 × magnification, repetition rate 1 Hz, laser fluence 175 mJcm^{-2}, depth 132 nm per pulse, 45° tilt angle, 200k × magnification.

Figures (5-27,5-28, 5-29, 5-30), show AFM images of the surface topology of; un-irradiated chitosan film and laser irradiated chitosan film at a fluence of 80, 135 and 760 mJcm^{-2} respectively. this corresponds to average surface roughness, *Ra* ~ 32, 45, 110 nm respectively. The topography of the un irradiated and laser irradiated samples at the low fluence (80 mJcm^{-2}) are very similar. At a laser fluence of 135 mJcm^{-2} some bubbling is observed. The bubbling and cavity formation is unevenly distributed over the chitosan surface and *Ra* values vary over the measured area of 50 × 50 μm^2. At the high fluence of 760 mJcm^{-2} there is a concomitant increase in the density of foaming and cavities. Figure (5-30) indicates signs of strain on the surface and may be explained by chitosan having a negative thermal expansion coefficient

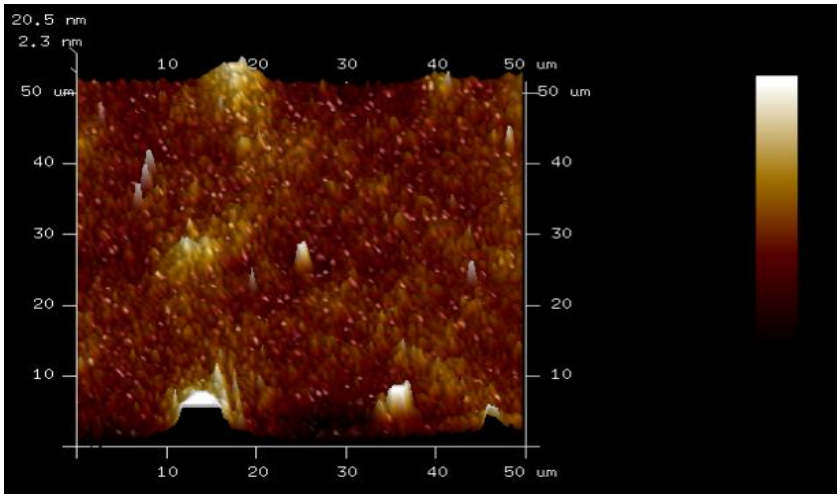

Figure 5-27: AFM micrograph of un-irradiated chitosan film

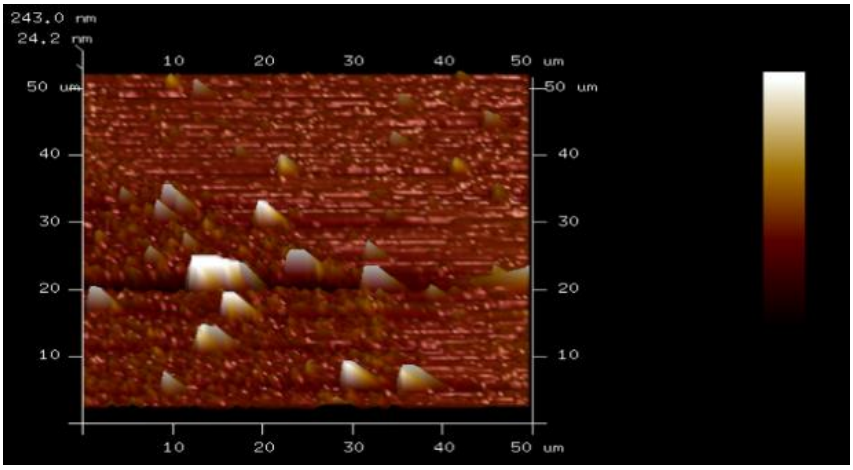

Figure 5-28: AFM micrograph inside the ablation crater of chitosan film was irradiated with 193 nm laser, imaged in 10 × magnification, repetition rate 1 Hz, laser fluence 80 mJcm^{-2}.

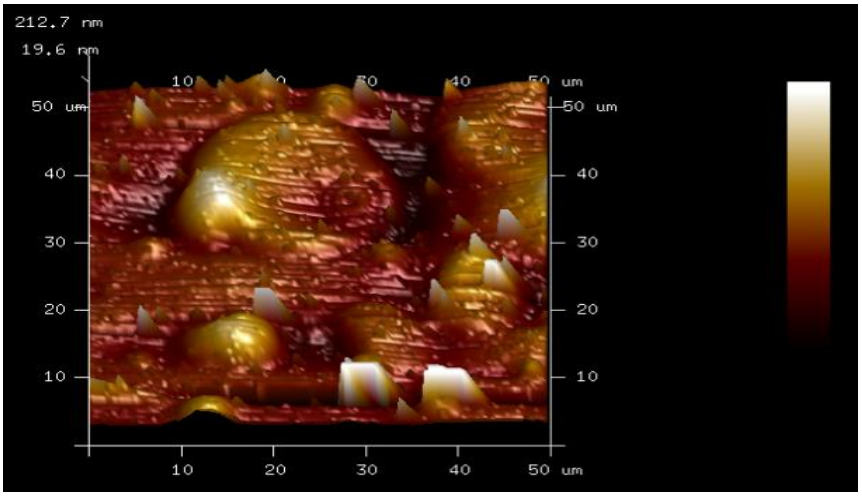

Figure 5-29: AFM micrograph inside the ablation crater of chitosan film was irradiated with 193 nm laser, imaged in 10 × magnification, repetition rate 1 Hz, irradiated with high laser fluence 135 mJcm^{-2}.

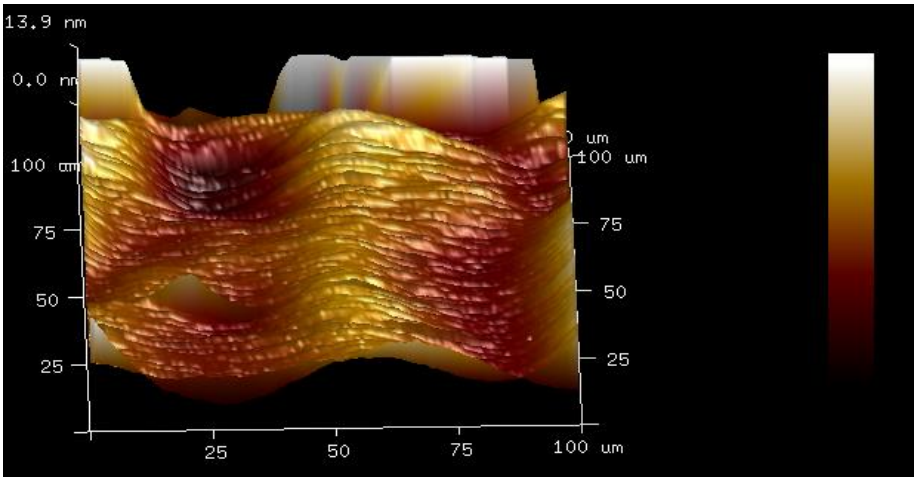

Figure 5-30: AFM micrograph inside the ablation crater of chitosan film was irradiated with 193 nm laser, imaged in 10 × magnification, repetition rate 1 Hz, irradiated with high laser fluence 760 mJcm^{-2}.

MatLAB was used to implement a simple model using equations ((2-39)-(2-42)) to simulate the propagation of a laser generated stress wave in a material that has a free surface. Figure (5-31) shows the simulated photo-acoustic wave propagating in a planar film at different times after absorption of a laser pulse.

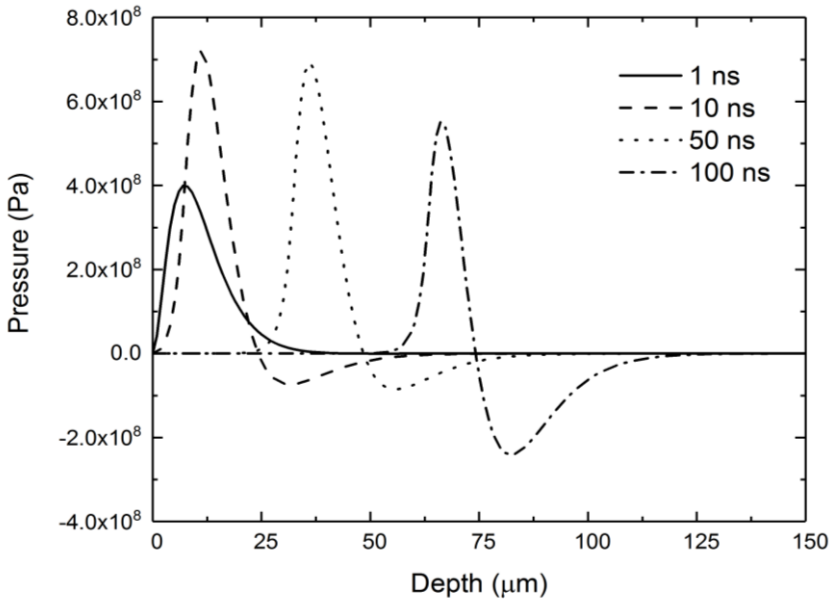

Figure 5-31: Simulated photoacoustic stress wave using MatLAB. Positive values correspond to compressive stresses and negative values are tensile stresses. The different curves correspond to times: 1 ns, 10ns, 50 ns, and 100 ns. The laser pulse is 11.5 ns FWHM, and a Gruneisen coefficient of $\Gamma = 1$. Laser fluence of 760 mJcm^{-2}.

Figure (5-31) is simulated for the material chitosan and at a corresponding laser fluence of 760 $mJcm^{-2}$. A tensile stress corresponds to a negative value and conversely a positive value corresponds to a compressive stress. As can be seen a tensile stress increases as the acoustic wave propagates with depth into the chitosan sample.

5.3.7. Grating fabrication by laser lithography

Diffraction gratings made from bio-compatible materials are receiving a great deal of interest within the scientific community. There are different techniques now used to manufacture diffraction gratings. Mechanical scribing [43], dip pen lithography [44], 3D printing [45], micro-contact printing [46,47] and laser ablation [48–50]. In this section we report the realisation of diffraction gratings by a laser direct write (LDW) method. In the research field the diffraction grating is useful in many areas of technology as gratings can be written at specific spatial location on a sample or device architecture. Using LDW a small features can be realised rapidly and over large areas. This fabrication technique has the advantage over some processes as it is a relatively quick processing technique as the work can be rapidly translated relative to a stationary beam. The diffraction grating was discussed with more details in chapter 4 of this thesis.

5.3.7.1. Surface relief grating on the chitosan film

An optical micrograph of the chitosan grating is shown below in figure (5-32). As can be seen well defined linear grooves have been produced leaving little re-deposited debris on surface of the chitosan film. From WLI data a line profile was extracted and a grating period of Λ =12 μm was measured. A graph of the grating spatial frequency is shown in Figure (5-33). This data was acquired using a WLI and analysed using the Power Spectral Density (PSD) function.

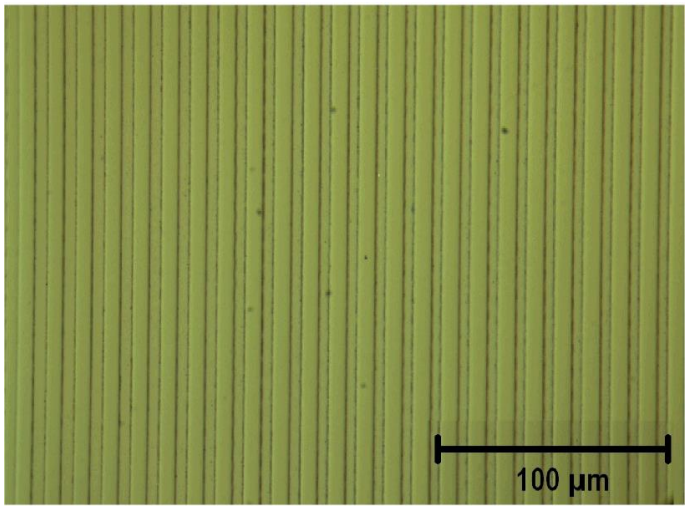

Figure 5-32: Optical micrograph of a chitosan relief grating realised by laser ablation a wavelength of 193 nm. The grating period is Λ=12 µm, laser fluence F = 110 mJcm^{-2}, 42 overlapping pulses and a pulse repetition frequency of 10 Hz.

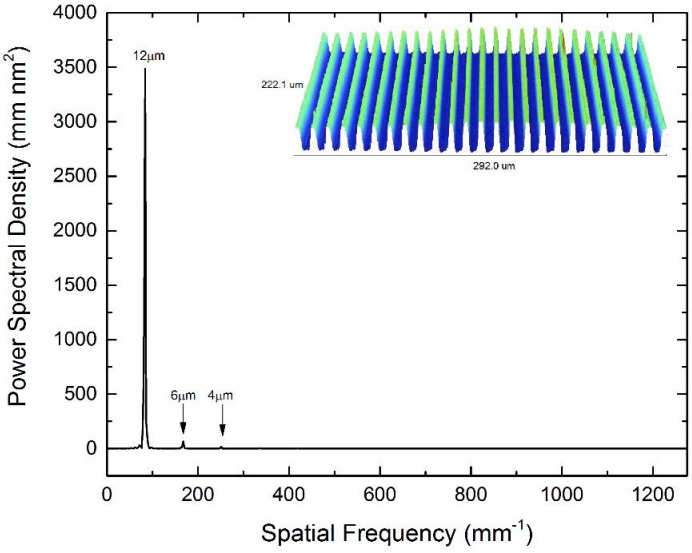

Figure 5-33: Power Spectral Density (PSD) measurement of the surface relief grating using a white light interferometer, objective 10 × magnification. Inset shows a 3D view of a typical section of the grating.

As can be seen from the PSD result the grating has a well-defined period of 12 µm. It is also noted from the graph one can see evidence of sub grating periodic structure at periods of ~4 µm and ~6 µm. This is thought to be due to stitch errors and possibly stress relaxation taking place. The inset of Figure (5-33) shows a 3D image of a small area on the grating. A magnified 1D cross-section of the grating showing five peaks is shown in Figure (5-34) below.

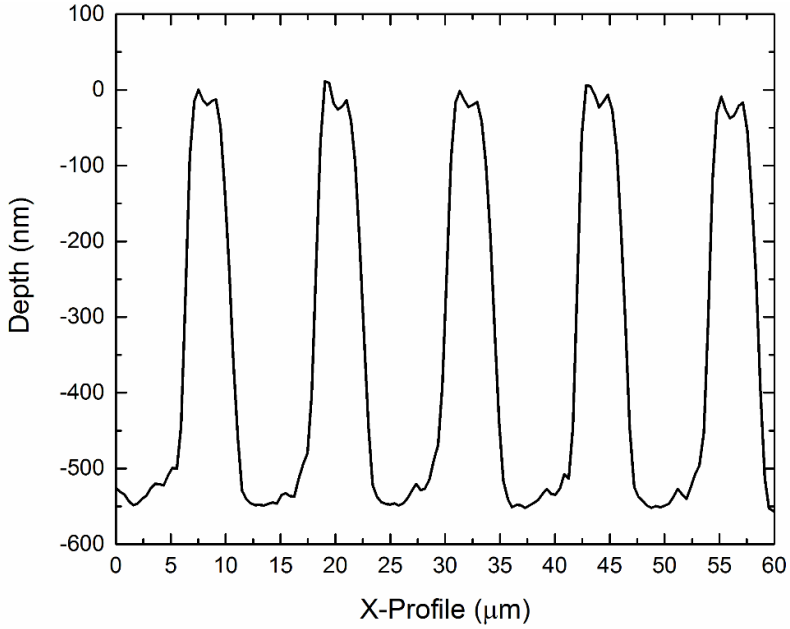

Figure 5-34: 1D cross-section of the 12 μm chitosan grating using data from the white light interferometer. Depth of the grating is ~510 nm.

There is some evidence that the asymmetric structure of the peaks is consistent with the PSD measurements. Figure (5-35) shows a scanning electron micrograph (SEM) measurement of the grating. The SEM shows well defined chitosan tracks with some evidence of surface texturing on the top of these tracks.

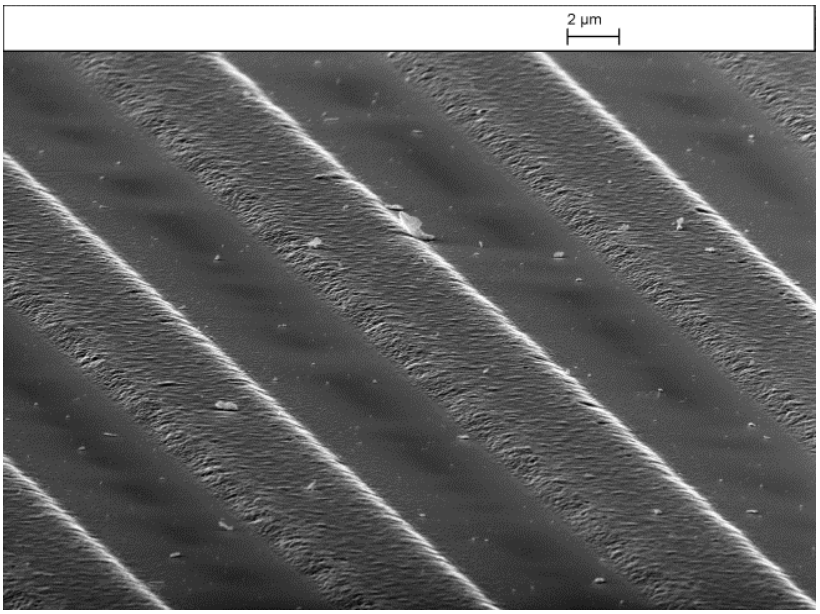

Figure 5-35: The scanning electron micrograph of chitosan relief grating (11.85k × magnifications, 80◦ tilt). A laser fluence of 110mJcm^{-2} at a pulse repetition frequency of 10 Hz, 42 overlapping pulses and a pulse repetition frequency of 10 Hz.

Using a WLI we compared the surface roughness of the as spun chitosan films with the laser processed chitosan. In the as-spun film a surface roughness R_a of 4 nm was measured, whilst for the laser processed chitosan, using a masking technique, revealed a slight increase in the surface roughness producing a value of R_a = 6 nm. We note the area over which these measurements were acquired were small area and it is therefore not really possible to draw any conclusive comparison between the irradiated and unirradiated chitosan other than the spun coated surface roughness is low. The grating tracks should be void of 193 nm photon flux and therefore the texturing may be due to stress induced relaxation as the temperature of the chitosan rises and falls. An AFM micrograph of the chitosan grating is shown by figure (5-36) with clear evidence of finding some surface texture on grating surface.

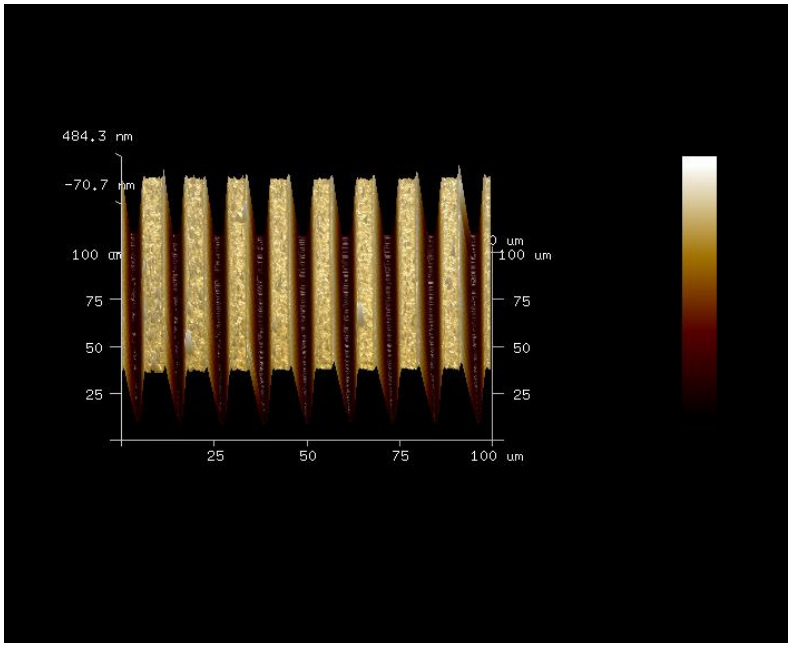

Figure 5-36: AFM micrograph of the surface relief grating 12μm period on the chitosan film. A laser fluence of 110mJcm^{-2} at a pulse repetition frequency of 10 Hz, 42 overlapping pulses and a pulse repetition frequency of 10 Hz.

Figure (5-37) below shows an intensity cross-section of light from a HeNe 632.8 nm laser. The data shows clearly the 0 order and ± 1, ±2 diffracted orders. Some diffracted and or scattered light is also evident between the orders.

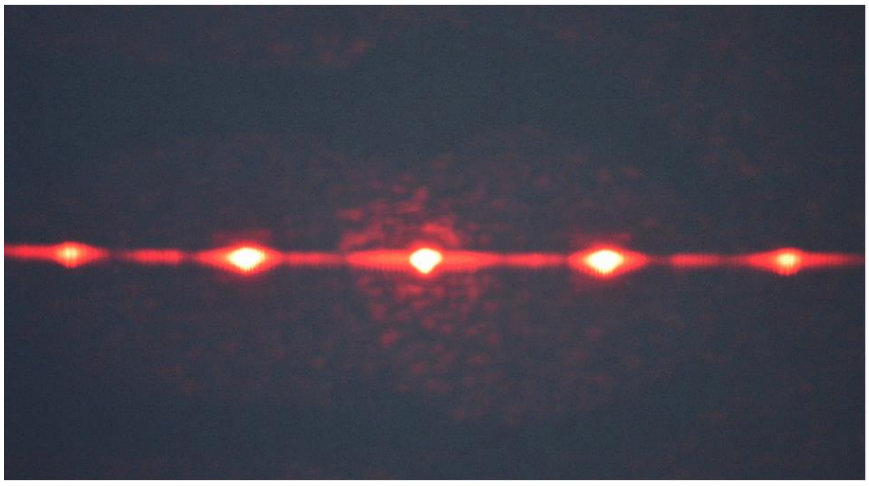

Figure 5-37: Far-field Fraunhofer diffraction pattern of the chitosan relief grating, illuminated with a 5W HeNe laser, wavelength 632.8nm.

Diffraction grating order efficiency measurements were also undertaken. The films were left supported on their glass substrates and probed using a low power HeNe laser λ = 632.8 nm. Within the uncertainty associated with the grating measurements the efficiencies were symmetrical between the corresponding positive and negative diffracted orders: **0** = 40%, **±1** = 24%, **± 2** = 2% (order uncertainty ±3%, reflection loss 4%). Laser processing of chitosan at a wavelength of 193 nm is seen to exhibit strong efficient coupling of UV light with relatively little laser induced damage. Calculations of the heat diffusion length l_h is confined to within a short distance, $l_h = \sqrt{4D\tau}$ = 200nm. Laser ablation was carried out close to the ablation threshold minimising the induced temperature rise.

5.3.7.2. Surface relief grating on the agarose film

The surface relief grating was fabricated on the agarose film in thickness of 750 nm. The agarose film was spin coated on the soda lime glass microscope slide 25 mm^2. An optical

micrograph of agarose grating is shown in figure (5-38) with an evidence of some texture was deposited on the surface.

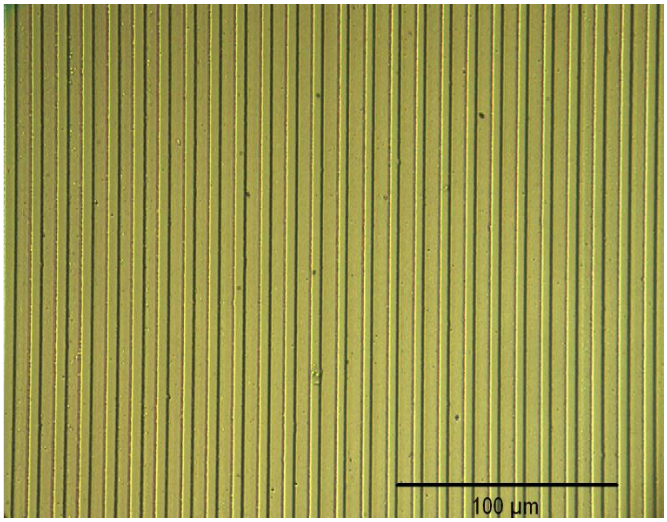

Figure 5-38: Optical micrograph of agarose relief grating realised by laser ablation a wavelength of 193 nm. The grating period is Λ=11.5 µm, laser fluence F = 125 mJcm^{-2}, 65 overlapping pulses and a pulse repetition frequency of 10 Hz.

The Power Spectral Density (PSD) of the grating data was extracted by the WLI is shown in figure (5-39). It can be observed that the grating in period of 11.5µm with indication of smaller periods of 5.7µm and 3.7µm were created on the surface. The small period structure might be due to stitch the lines or the heating relaxation produces by the laser. The inset in the figure (5-39) is the 3D WLI of the grating. The SEM image of the grating 11.5µm is shown in figure (5-40). This figure illustrates well defined grooves with an evidence of producing texture on the bars of the grooves.

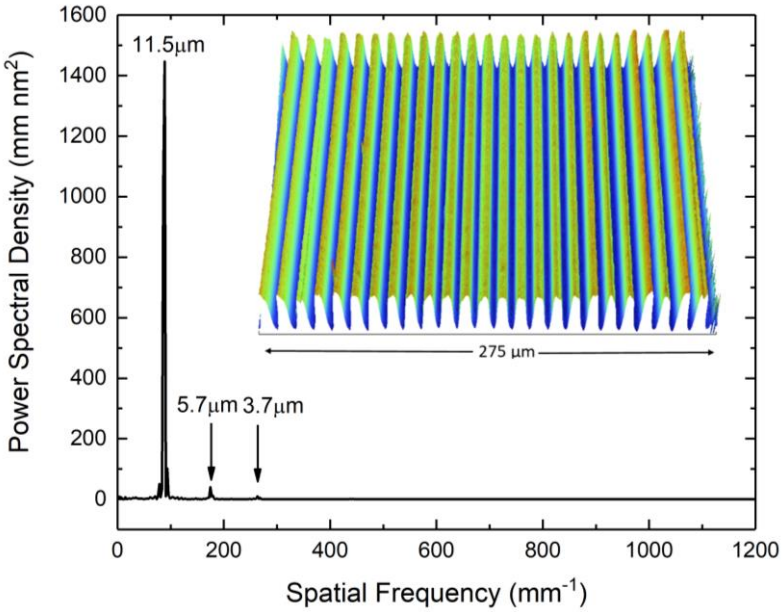

Figure 5-39: Power Spectral Density (PSD) measurement of the surface relief grating on the agarose film using a white light interferometer, objective 10 × magnification. Inset shows a 3D view of a typical section of the grating.

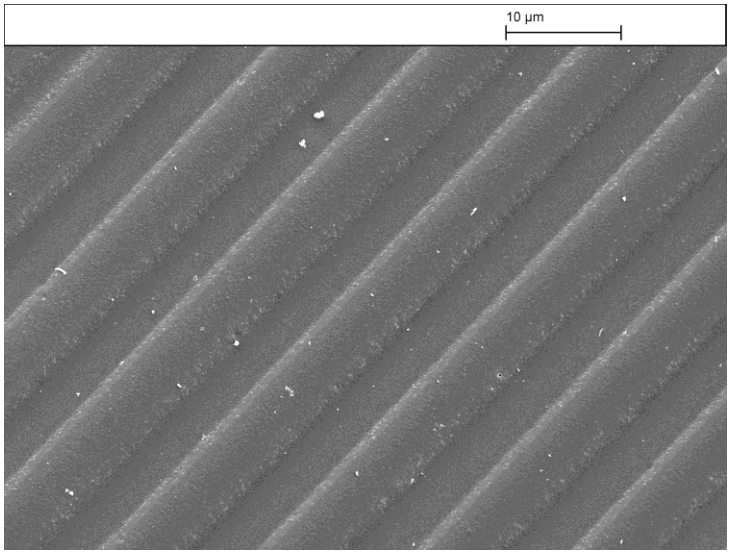

Figure 5-40: The SEM micrograph of the grating was formed on the agarose film in thickness of 750nm, 1/5 demagnification, parallel bar grid (400 bars), ablation site 390 um, laser fluence 125 mJcm^{-2}, feed rate 0.06mm/sec, depth ~ 380nm, 6k SEM magnification, 10° tilt.

Figure (5-41) below shows the AFM micrograph of the surface relief grating on the agarose film. It is clear that the agarose film surface was affected by the laser irradiation, therefore some ablated material were deposited on the surface.

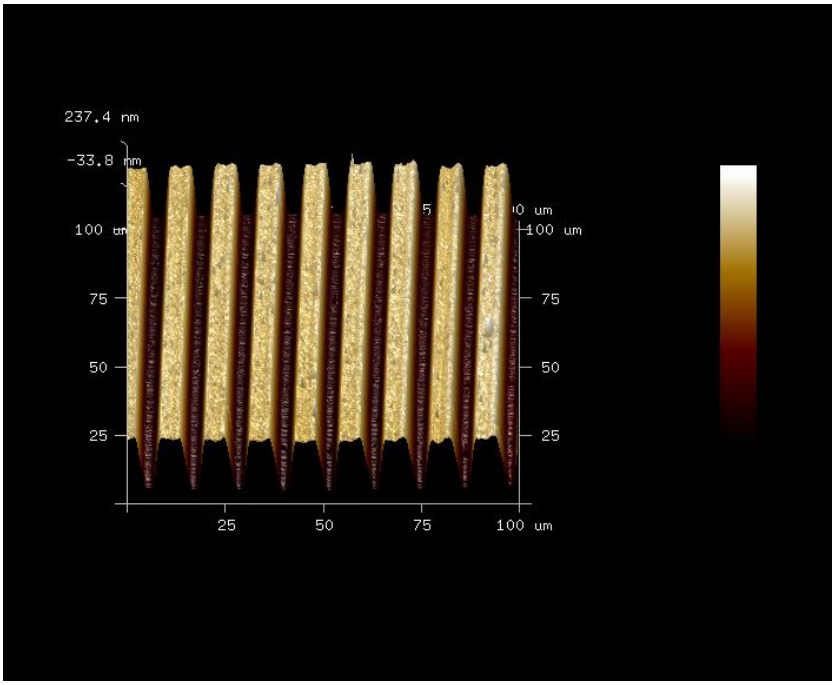

Figure 5-41: AFM micrograph of the surface relief grating on the agarose film. Using a 1/5 demagnification, parallel bar grid (400 bars), ablation site 390 um, laser fluence 125 mJcm^{-2}, feed rate 0.06mm/sec, depth ~ 380nm.

The surface roughness measurements were carried out using masking technique with the WLI to compare the surface roughness of unirradiated agarose film and grated film with 193 nm laser. The measurements show that the Ra of unirradiated agarose film was 3nm whereas for the grated film is approximately 16.5 nm on the top of grooves bars and 12.75 nm on the bottom of the grooves which is relatively high. These roughness measurements values were taken of an average of four reading of different position for the bottom and for the top of bars of grooves. The increasing in the roughness is due to the texture on the grating surface. In addition, this is evidence that the agarose film was effected with laser irradiation. Figure (5-42) shows the 1D cross section of 4 peaks of the grating was got from the WLI.

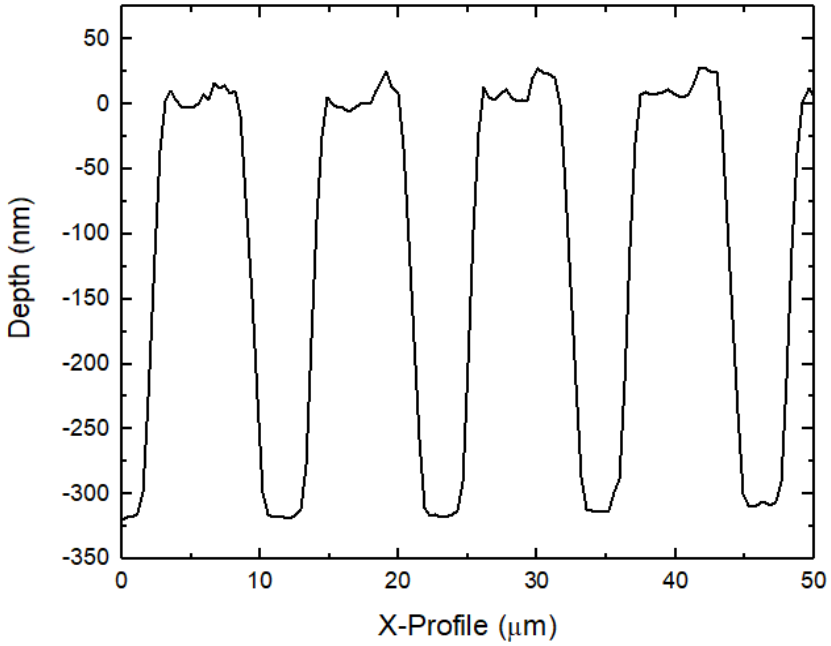

Figure 5-42: 1D cross-section of the grating realized on the agarose film using data from the white light interferometer. Depth of the grating is ~325 nm.

Figure (5-43) shows the far-field of the diffraction grating orders of agarose grating was carried out using HeNe, 632.8 nm, 5mW. The figure indicates the 0 and ±4 diffraction orders corresponding to the positive and negative orders with clear patterns between orders.

Figure 5-43: Far-field Fraunhofer diffraction pattern of the agarose relief grating, illuminated with a HeNe laser wavelength 632.8nm, 5mW.

5.3.8. Diffraction grating using soft-lithography

Periodic arrays of lines with periods of 1µm on the polyester film were successfully replicated. The power spectral density (PSD) of an example of the periodic line structure is given in Figure (5-44) and the inset shows the 3D WLI and the card images of the grating array. The PSD of this example shows a spacing of 1µm with evidence of 0.48 µm were fabricated on the film surface. The inset in the figure (5-44) shows two pictures, the 3D WLI image of the example grating (left) and the card image (right).

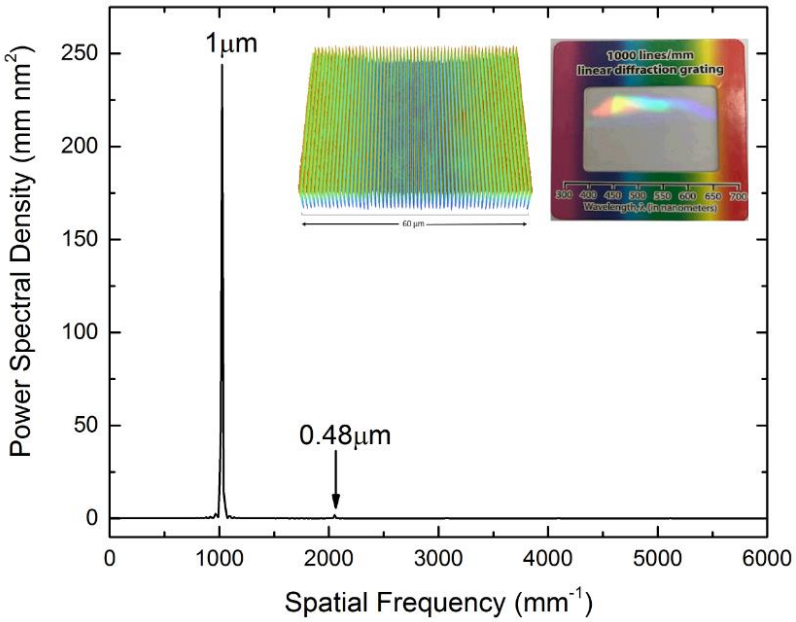

Figure 5-44: Power spectral density (PSD) of one example of linear grating. Inset shows the WLI image of the grating and the image of the card includes the polyester film.

5.3.8.1. Grating replicated on the chitosan film

Figure (5-45) shows the power spectral density (PSD) of periodic lines 1µm were replicated on the chitosan film using imprinting technique. The figure illustrates two grating period, 1µm which corresponds to the original spacing on the polyester film and 0.48 µm which corresponds to the small spacing was shown on the film.

Figure (5-46 A and B) shows the AFM micrographs of the 1µm chitosan grating. It showed that the parallel lines remained with the same spacing of the original film.

However, the density of the smallest feature size 0.48 µm is increased slightly than the original one. It can be seen that the structure does not influence the quality of the replication process as well as the resolution not been affected. In addition, it can be observed that the surface of the grating lines is smooth with well define walls. 1D cross section with 7 peaks of the replicated grating is shown in figure (5-47) and these data was extracted from the WLI.

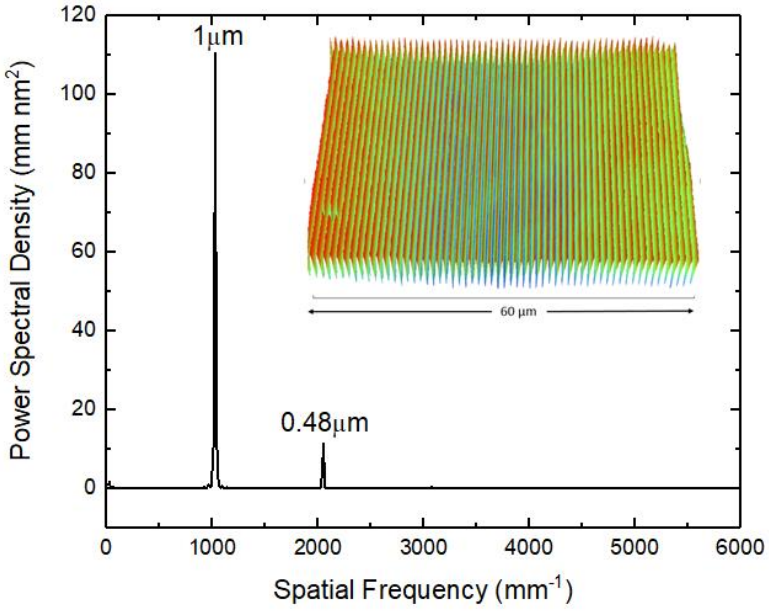

Figure 5-45: Power Spectral Density (PSD) measurement of the chitosan printed grating using a white light interferometer, objective 50 × magnification. Inset shows a 3D view of a typical section of the grating.

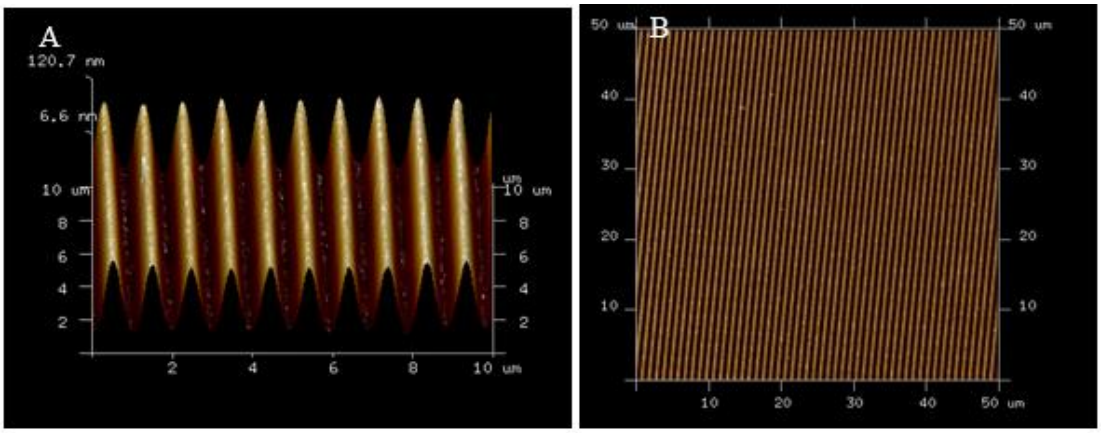

Figure 5-46: The AFM micrograph of the printed grating on the chitosan film in period of 1µm with two different scanning area (A) 10 µm² (B) 50 µm².

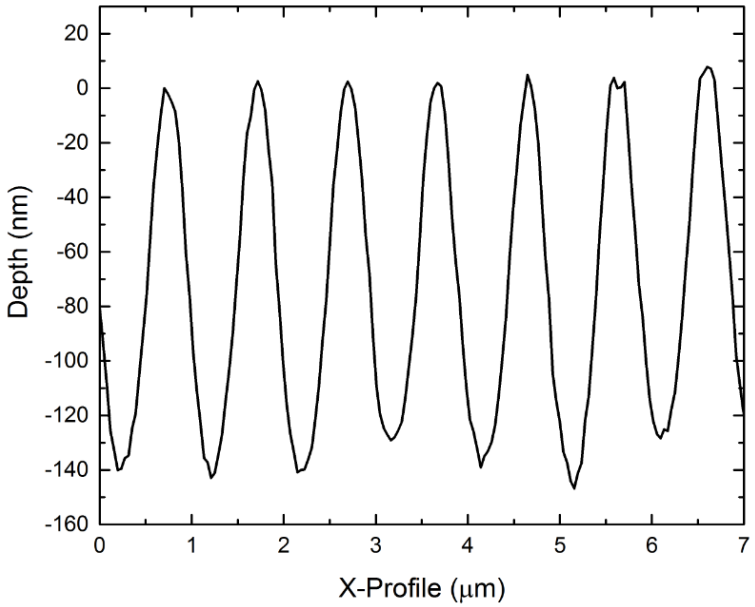

Figure 5-47: 1D cross section of the imprinted grating on the chitosan film and it indicates the grating depth is ~140nm.

The chitosan film has not shown a noticeable adhesion on a polyester film of the grating after the nanoimprinting process. Furthermore, nanoimprinting lithography offers a simple and inexpensive fabrication method for micro- and nanoscale structures of chitosan. The nanoimprinted chitosan patterns can be utilized as structures for nanotechnology and biosensors applications.

5.3.8.2. Grating replicated on the agarose film

A power spectral density (PSD) of the replication diffraction leaner grating formed on the agarose film is shown in figure (5-48). It can be observed that both feature patterns the original feature size 1um and the smallest one 0.48 μm has replicated into agarose film. As well as, it can be noticed that the diffraction grating resolution remain the same for both feature size. However, the surface of the grooves tend to be rough due to the imprinting processing. An atomic force microscopy (AFM) image in Figure (5-49, A and B) shows periodic pattern of 1 μm directly transferred to the agarose film. These nano-printing was achieved by the drop casting of agarose solution into transmission diffraction grating (Edmund co.). The 1D cross-section measurement extracted from WLI

corresponding to the leaner grating is illustrated in Figure (5-50). It can be seen that the replicated features of 1 µm realized in the agarose film are approximately in depth of ~225 nm. Other visible depth in the cross-section is an object of the drop casting process, has been addressed.

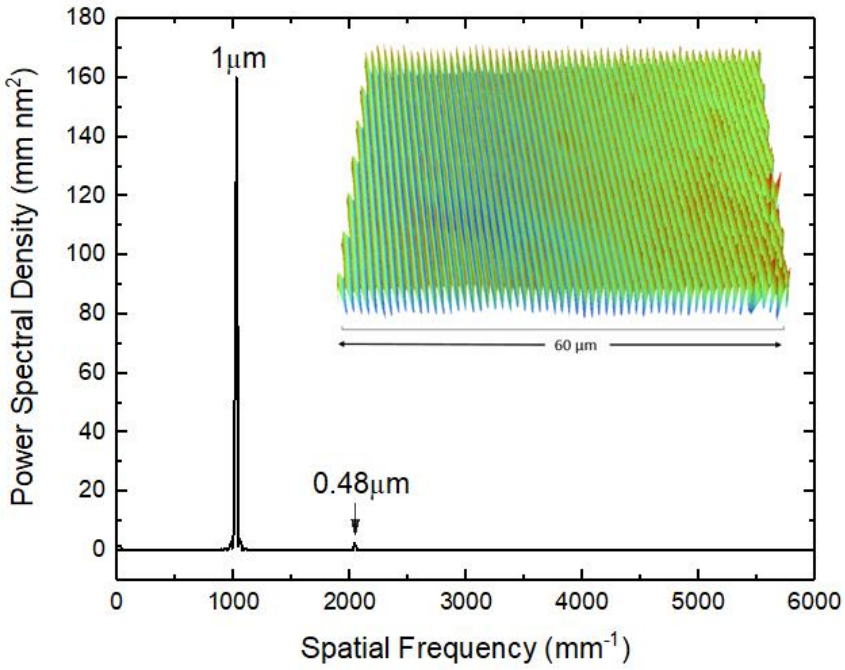

Figure 5-48: Power Spectral Density (PSD) measurement of the printed grating using a white light interferometer, objective 50 × magnification. Inset shows a 3D view of a typical section of the grating.

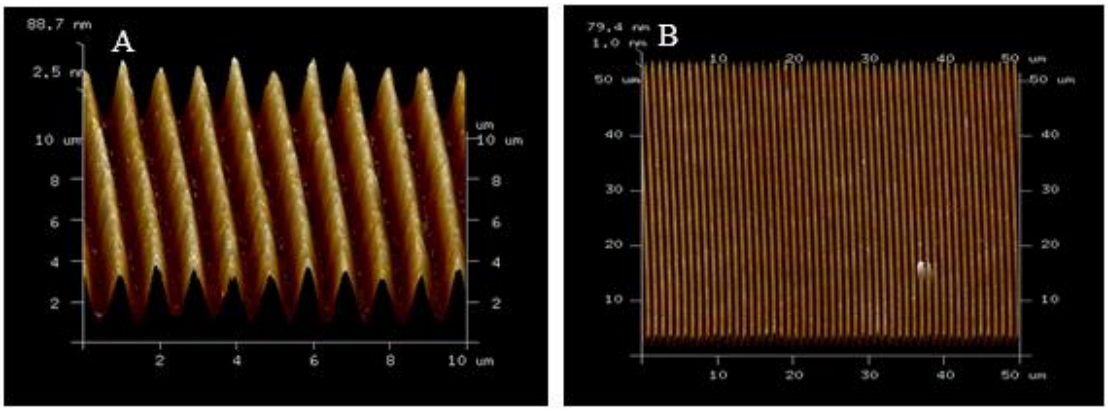

Figure 5-49: The AFM micrograph of the imprinted grating on the chitosan film in period of 1µm with two different scanning area (A) 10 µm^2 (B) 50 µm^2.

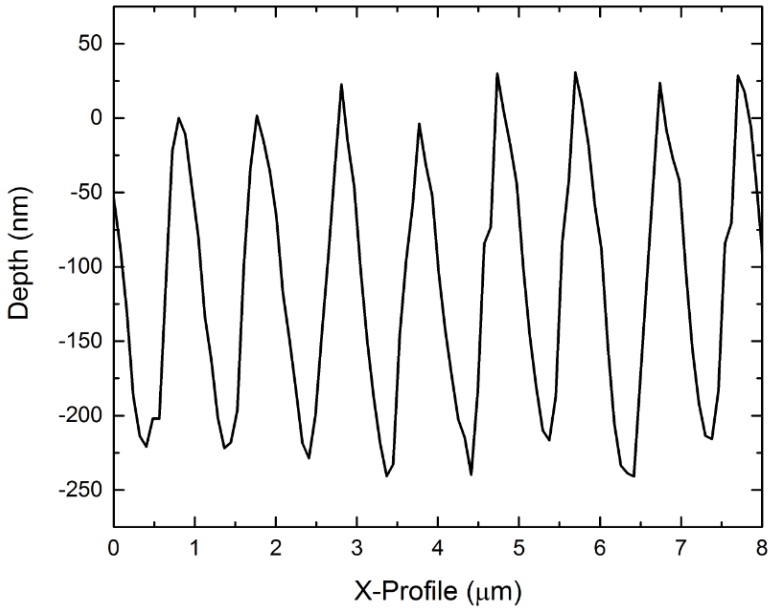

Figure 5-50: 1D cross section of 1μm period of the imprinting grating on the agarose film in depth of ~225 nm.

The agarose film has not shown a noticeable adhesion property on a polyester film of the grating. In addition, it was noticed that the agarose film is peeled off itself. These nano-imprinting experiments of the patterned films fabricated with this technique provides a capability for future experiments of the formation of diffraction grating on the biocompatible materials for a wide range of micro and nano applications.

Laser processing of bio-compatible materials is an active area of research. Part of this work has been carried out to investigate the interaction of UV 193 nm laser radiation with chitosan and to study the possibility of realising small optical components on biocompatible materials; chitosan and agarose. A wide range of laser fluences were used to determine the ablation threshold of chitosan at 193 nm laser and 85 $mJcm^{-2}$ has been reported. A foaming formation was observed on the chitosan film at higher laser fluence. A photoacoustic effect is a suggested mechanism for the foaming formation on the surface. Diffraction gratings are one of the optical components that might be used on various optical applications such as lab on chip (LOC), grating couplers and biosensors. In this work, two techniques have been used to produce the diffraction grating; laser

lithography and nanoimprinting. Direct-writing laser beam lithography represents a high flexibility tool for realising a diffraction grating. However, a relatively large grating period fabricated on biocompatible materials (mentioned above) using this method has been reported. Therefore, reducing the grating pitch using the laser lithography technique may be the next step forward in this work.

5.3.8.3. Fabrication a microstructure

The Figure (5-51) shows a 2D cross-grating was realised in chitosan, a biocompatible chitosan film, using an Argon Fluoride excimer laser. This figure shows small parts of the grating, 5mm × 5mm, measured with a white light interferometer (WLI) WYKO NT 1100. The structure was produced by mask projection and translating the sample in orthogonal directions relative to the stationary 193 nm laser beam. Laser ablation was carried out using a laser fluence of 110 $mJcm^{-2}$, a pulse repetition frequency of 10 Hz and a motion control stage (Aerotech Fiber Align) velocity of 0.1 mms^{-1}. The column-like structures are 7 microns square and 525 nm high.

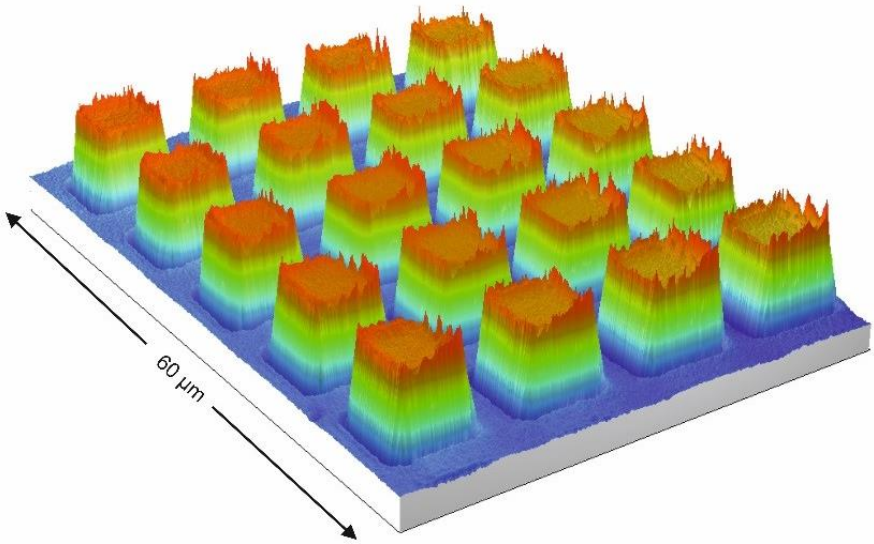

Figure 5-51: White light Interferometry (WLI) measurement of laser irradiated chitosan. The square structures are 7 microns square and 525 nm high. The structure was produced by mask projection and translating the sample relative to the beam using a laser fluence 110 $mJcm^{-2}$, at a pulse repetition frequency of 10 Hz, a stage velocity of 0.1 mms^{-1} and receiving 40 overlapping laser pulses.

The SEM micrographs of the microstructure made of chitosan film are shown in figure (5-52, A and B). A square array of 7×7 is shown in figure (5-52 A) and more squares lines can be seen in the same figure (B) due to the tilt of 80° action during the SEM measurements. Clear evidence of temperature effect on the squares walls and this due to the heating effect of the laser during the ablation process.

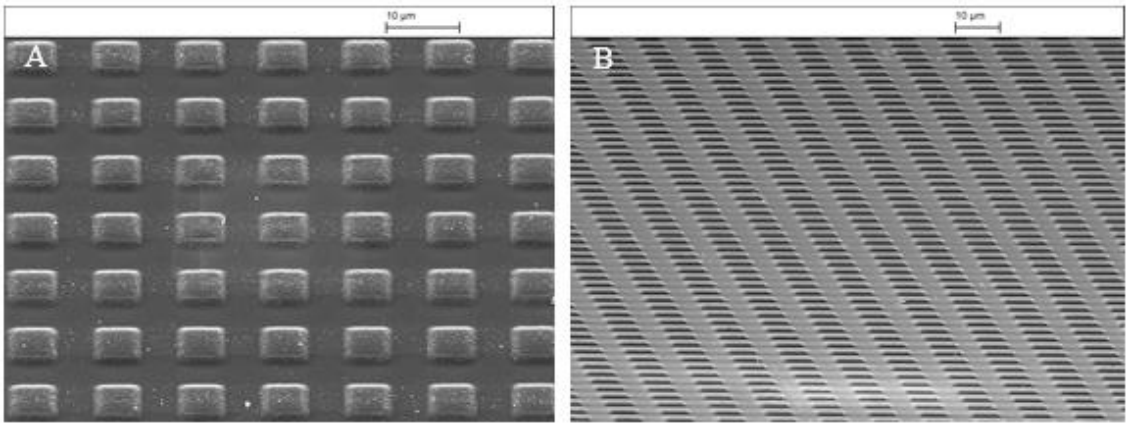

Figure 5-52 : The SEM micrograph of the patterning structure was formed on the chitosan film, film thickness of 600 nm, laser fluence 110 mJcm^{-2}, depth 320 µm, feed rate 0.1 mms^{-1}, 5× demagnification and laser pulse overlapping of 42 pulses, (A) ×5k SEM magnification, 45° tilt and (B) ×3k magnification with 80° tilt.

An AFM micrograph of the chitosan microstructure is shown in figure (5-53A). It can be seen that the squares features are rounded with more ablated area and this is interpreted by the lines crossed during the mask dragging process. On inspection of the chitosan there is little evidence of thermal damage to the square features. This may be attributable to the low laser fluence of 110 mJcm^{-2}, the short laser pulse duration and the low value of thermal diffusivity in chitosan. The diffraction order of the chitosan microstructure is shown in figure (5-53B), this was illuminated with the HeNe laser 632.8 nm, 5mW. It can be seen that the diffraction orders 0 and ±4 are in all directions. The ± corresponding to the positive and negative diffraction order.

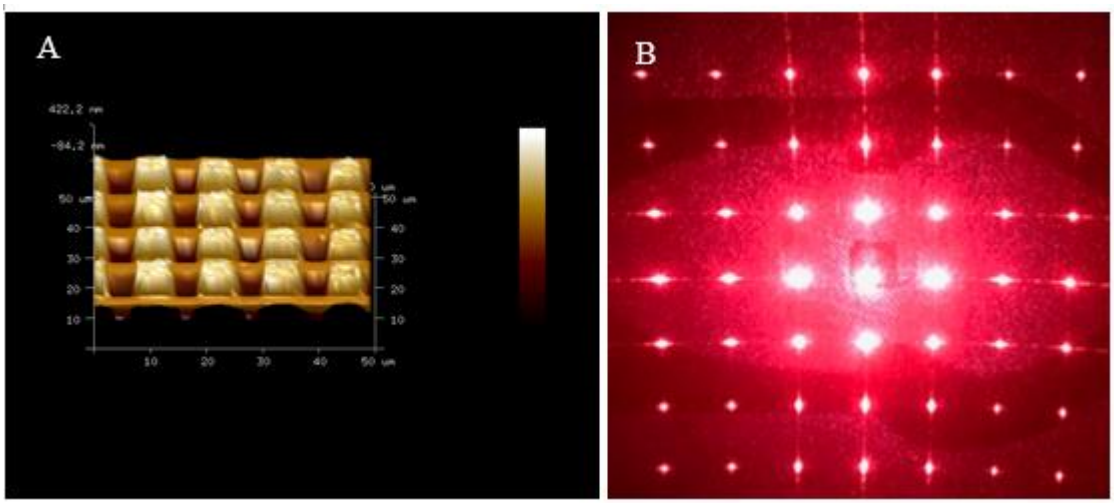

Figure 5-53: (A) The AFM micrograph of the chitosan microstructure under the same conditions of figure (8-2) and (B) the diffraction grating order of the chitosan microstructure produced with HeNe laser 632.8 nm wavelength.

Biocompatible agarose is another material processed with an ArF 193 nm laser to produce a microstructure. A film of agarose with thickness of 750 nm produced by spin coating the agarose film onto a microscope slide (soda lime glass). The presented technique was used to micromachine a 3D microstructure onto the agarose film. The SEM micrographs of the fabricated microstructure array of squares 5×4 with dimension of 5µm×7µm and depth of 420µm on the agarose film is shown in figures (5-54A and B). In figure (5-54B) is the same structure but with more squares lines due to tilted action of 80° sample rotation during the SEM measurements. These structure were made at the laser fluence of 125 $mJcm^{-2}$, 65 overlapping pulse and 10 Hz repetition rate frequency with a feed rate of (XYZ) nano-stages of 0.06 mm s^{-1}. A clean ablated surface can be observed with little evidence of damaging the edges of the squares and that may be due to either the photothermal effect of high temperature produced during the ablation process or when lines crossed together.

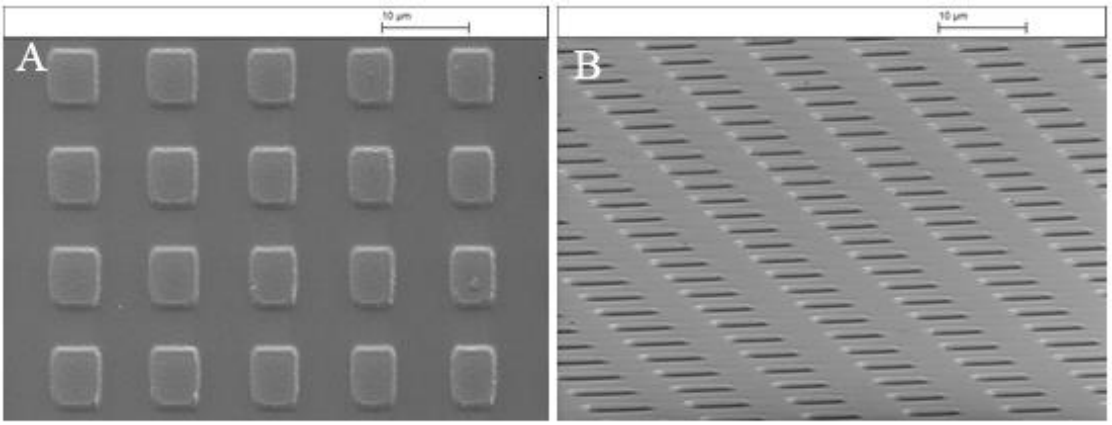

Figure 5-54: The SEM micrograph of the patterning structure was formed on the agarose film, film thickness of 750 nm, laser fluence 125 $mJcm^{-2}$, depth 420µm, feed rate 0.06 mms^{-1}, 5× demagnification and laser pulse overlapping of 65 pulses, (A) ×6k SEM magnification, 0° tilt and (B) ×6k magnification with 80° tilt.

An AFM image of the agarose microstructure is shown in figure (5-55A). It can be noticed that the ablated area around squares features is deepest. This structure was also characterized with the HeNe laser 632.8 nm, 5 mW to produce the diffraction grating orders. The diffraction order 0 and ±3 in all directions are shown in figure (5-55B).

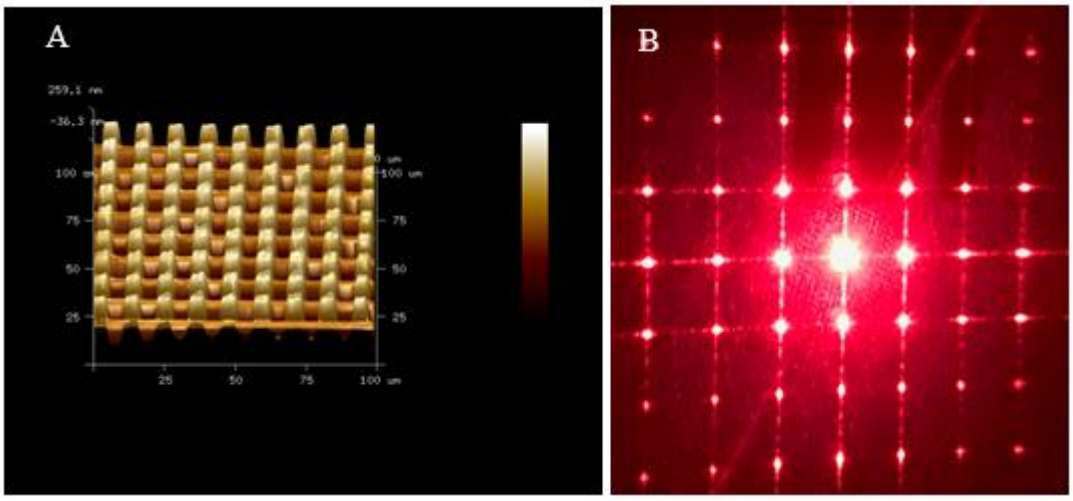

Figure 5-55: (A) An AFM micrograph of the agarose pattern structure under the same condition as figure (8-4) and (B) the diffraction order of the agarose microstructure produced with HeNe laser 632.8 nm wavelength.

These above examples of microstructures demonstrate that these arrangements can be effectively fabricated with a mask projection technique. These results also suggest that this technique can be employed to produce a microstructure with a few microns resolution

and large area of several millimeters. In addition all microstructure parameters can be controlled by the mask shape and laser parameters include; laser fluence, repetition rate frequency and to control the overlapping pulse.

Another set of experiments successfully utilised the Laser Ablation technique to fabricate a TEM-Hexagonal grid on the biocompatible chitosan film. Laser Ablation can be used to establish a well-organized TEM grid crater to be used for different applications. 5× demagnification was used to image the grid hexagonal (50 mesh and a diameter of 3.05 mm, Agar grids hexagonal 50 mesh, Nickel, AGG2405N, a tube of 100) onto the chitosan film aiming to modify the biomaterial chitosan surface by ArF laser beam. SEM and WLI were employed to characterise the modification surface. Figures (5-56-A,B,C and D) shows SEM micrographs of a crater formation with a diameter of 410 μm and depth of ~340 nm. This is a result of five laser pulses interacting with a flat surface and a laser fluence of 300 $mJcm^{-2}$. It can be observed that well define walls of the crater were established by the Laser Ablation. A part of the laser processing is to deposit the ablated material on the surface. However, due to ablation process there is debris present in the grid this is very clear on the figure (5-56D).

Near field of Fresnel diffraction was produced due to the laser beam that passed through the grid slots. The diffraction in front of the pinhole is occurred and it is altering as the light travels along the optical axis through and away when the light passing through the pinhole. As it close to be impossible to study the diffraction pattern near to the pinhole. Then it would be much easier to project the pinhole into a films using a lens with a demagnification system. In this work, as a hexagonal grid have been used in the projection system then each hexagonal mesh will work as a pinhole. For this reason, the near-field diffraction pattern producing during the ablation processing using a lens can be easily viewed on the irradiated sample. Also, a lens in this system is used to focus the light as a

solution of losing the light intensity. Therefore, a focused beam spot will has all the intensity of the beam. Using a demagnification system a higher percentage of the laser beam passes through this grid, therefore a more intensity of light beam will be in the diffraction patterns. Furthermore, the producing near field diffraction is changed as a function of the distance away from the projection mask. This can be seen clearly observed in the micrographs presented in figures (5-56 B and D). In addition, a halo appears around the ablated crater, this could be as a result of either stress or a photoacoustic mechanism could taken place during the ablation process which is discussed previously in this thesis. In addition, the heat produced by the laser irradiation influenced the surface of the ablated area. A 1D cross-section of the hexagonal crater was extracted from WLI data is shown in figure (5-57). This exhibits a depth of ~340 nm for four hexagonal unit structures.

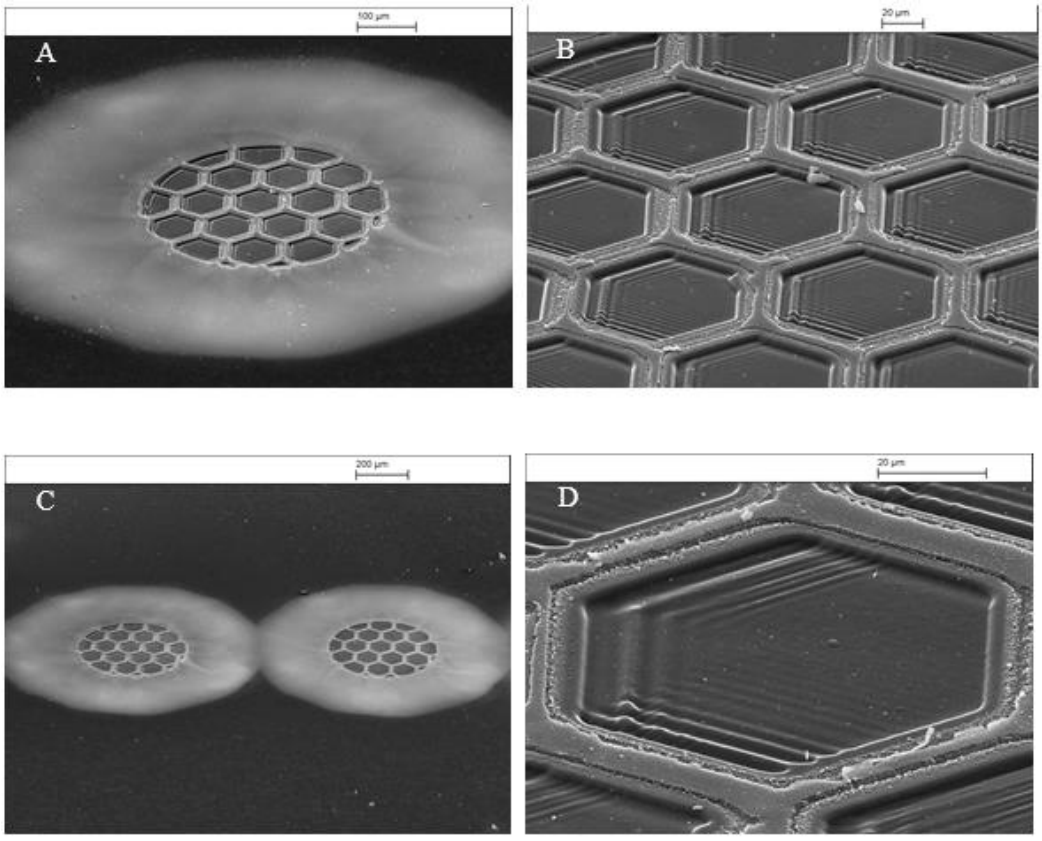

Figure 5-56: SEM micrographs of Hexagonal TEM grid 50 mesh imaged on the chitosan film using 193 nm laser, 5× demagnification, laser fluence 300 mJcm^{-2}, 5 pulses (A) 450× magnification, 60° tilt (B) 1.7K× magnification, 60° tilt (C) two ablation site with 200× magnification, 60° tilt (D) One hexagonal structure, 4K× magnification, 60° tilt .

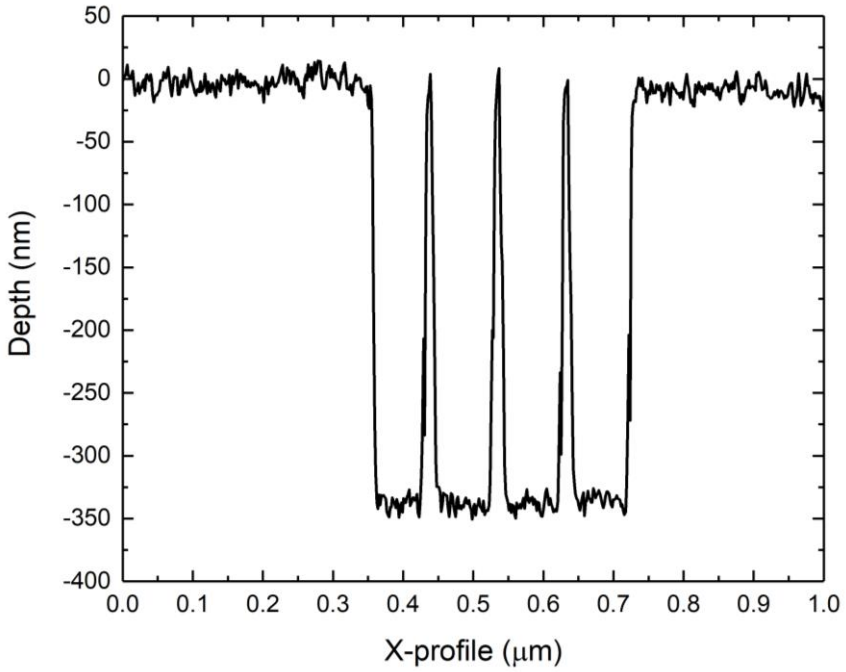

Figure 5-57: 1D cross section of hexagonal TEM grid imaged on the chitosan film with the same conditions as figure (8-6), this indicates that the depth of the ablation site is ~ 340 nm.

Fabrication of periodic structures with micron and nano features on the biocompatible materials is the area of interest of the researcher groups. An array of microstructures were formed on the biocompatible materials films utilising mainly laser direct writing, which is considered as a multipurpose technique to produce microstructures and to modify the surface of materials.

5.3.9. Electro-Optical properties of 5CB doped chitosan

5.3.9.1. Results and discussion

In this section the results of all experiments were carried out using the 5CB LC doped chitosan material and will be presented and discussed at a later point.

5.3.9.1.1 UV-VIS measurement

UV-VIS measurements were carried out on solutions of 5CB LC and 5CB LC doped chitosan. The absorbance of 5CB LC and 5CB LC doped chitosan is represented in figure

(5-58). It can be seen that the 5CB LC has a relatively high absorption in the ultraviolet and visible range. As can be seen the optical absorption increases more at wavelengths < 350 nm. This figure shows that the absorption of PDLC and PDLC doped dye have similar behavior but the sample containing chitosan shows a slightly stronger absorption at shorter wavelength.

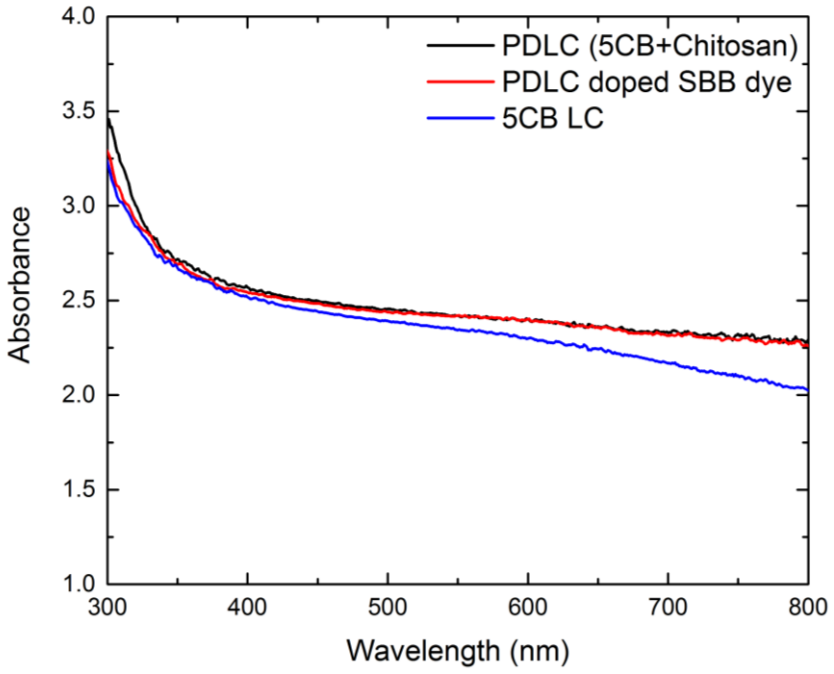

Figure 5-585: The UV-VIS spectrum of the absorbance of 5CB LC solution (blue line), PDLC 1% (5CB LC doped chitosan, black line) and PDLC doped 0.5% SBB dye (red line).

UV-VIS absorbance of SBB at different concentrations (0.1%, 0.2%, 0.3%, 0.4%, 0.5%) wt. /v is shown in figure (5-59). It is clear that the absorbance of the dye is increased by increasing the dye concentration. It can be seen that the SBB dye has a maximum absorbance at a wavelength of 600 nm. SBB dye absorbs the light in the visible range by promoting electrons in π orbital from the ground state to the higher energy state [342].

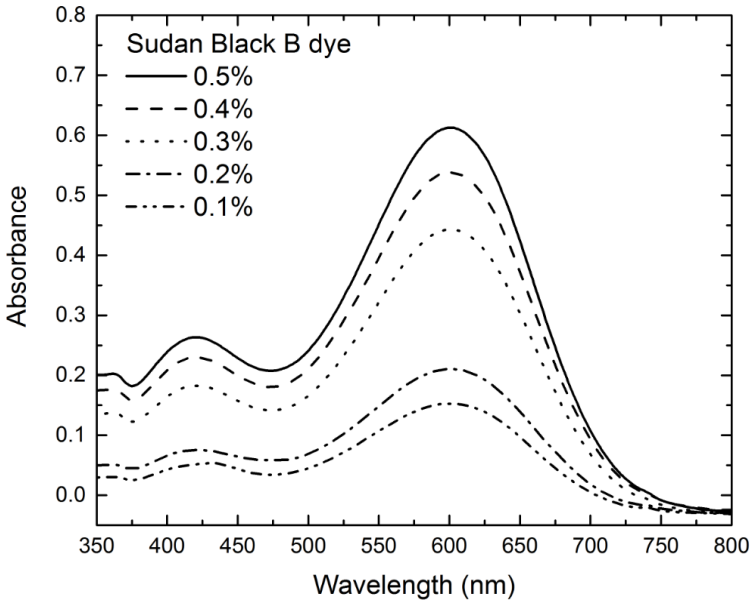

Figure 5-59: The UV-VIS spectrum of Sudan black B (SBB) in different concentrations (0.1%, 0.2%, 0.3%, 0.4%, and 0.5%) wt. /v.

The optical bandgap energy (E_g) of a material can be obtained from the UV-VIS spectrum using the Tauc relation. With knowledge of the absorption coefficient one can determine the optical bandgap. The Tauc relation can be written as follows [343].

$$\alpha = A\frac{\left(h\nu - E_g\right)^n}{h\nu} \tag{5-20}$$

Where, α is the absorption coefficient, A is constant, E_g is the bandgap energy and n is 0.5 and 2 for a material that has direct transition and for a material that has indirect transition respectively.

The bandgap energy of SBB dye is calculated using the Tauc relation with $n = 0.5$ as the SBB dye has a direct transition. Plots between $h\nu$ and $\left(\alpha h\nu\right)^2$ were carried out for different concentration (0.1%, 0.3%, 0.5%) of SBB to determine the band gap energy and they are shown in figures 5-60, 5-61 and 5-62 respectively. The absorption coefficient was calculated using Beer's law $\left(\alpha = A/cb\right)$ where, A is the absorbance, c is the concentration and b is the path length of the medium inside the cuvette.

These figures show that the band gap energy is decreasing by increasing the dye concentration to 1.838 eV, 1.821 eV and 1.814 eV for 0.1%, 0.3% and 0.5% respectively.

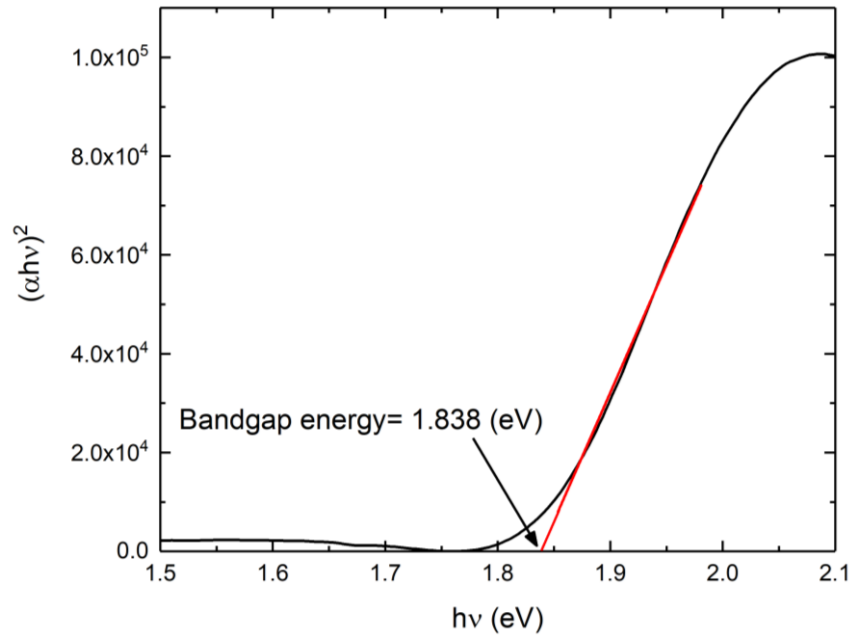

Figure 5-60: The bandgap energy measurement of Sudan Black B dye in concentration of 0.1% wt. /v using the Tauc relation.

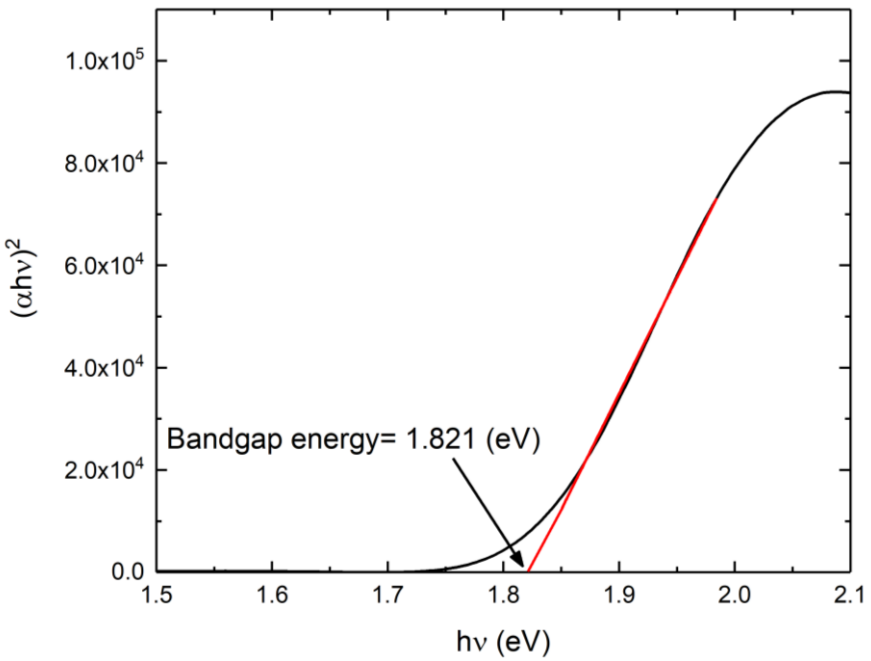

Figure 5-61: The bandgap energy measurement of Sudan Black B dye in concentration of 0.3% wt. /v using the Tauc relation.

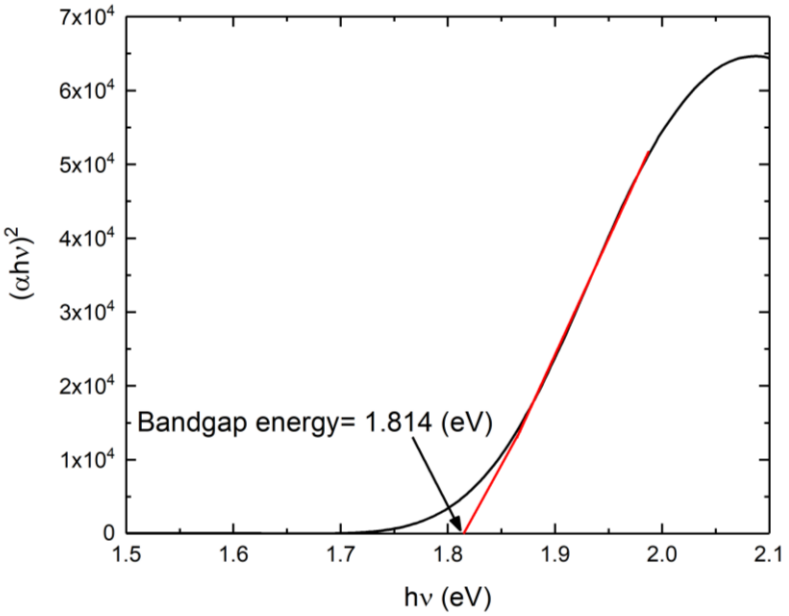

Figure 5-62: The bandgap energy measurement of Sudan Black B dye in concentration of 0.5% wt. /v using the Tauc relation.

Figure (5-63) shows the optical textures of the polymer dispersed LC in the ratio of 20:80 (wt. %) (5CB: chitosan). Optical microscopic images show a non-homogeneous distribution of 5CB LC dispersed in the biopolymer chitosan matrix. The birefringence of the 5CB texture is apparent in these optical microscope images. The birefringence is one of the optical properties of the nematic LC materials. The nematic LC exhibits the birefringence because the refractive index is affected by the light direction passing through the sample [58]. Also, change in the birefringence is accompanied with changing of the transition of liquid crystalline phases [344]. The nematic LC has a large birefringence make them suitable for liquid crystal display devices [58]. As well as an observation that indicates that the liquid crystal is non-homogenously dispersed in the biopolymer matrix. It can be noticed in figure (5-63, B) that the 5CB LC has orientated as trees structures and these are may be due to the coating process. AFM micrographs of randomly distributed molecules of 5CB LC are shown in figure (5-64) which confirm the observation in the optical micrographs.

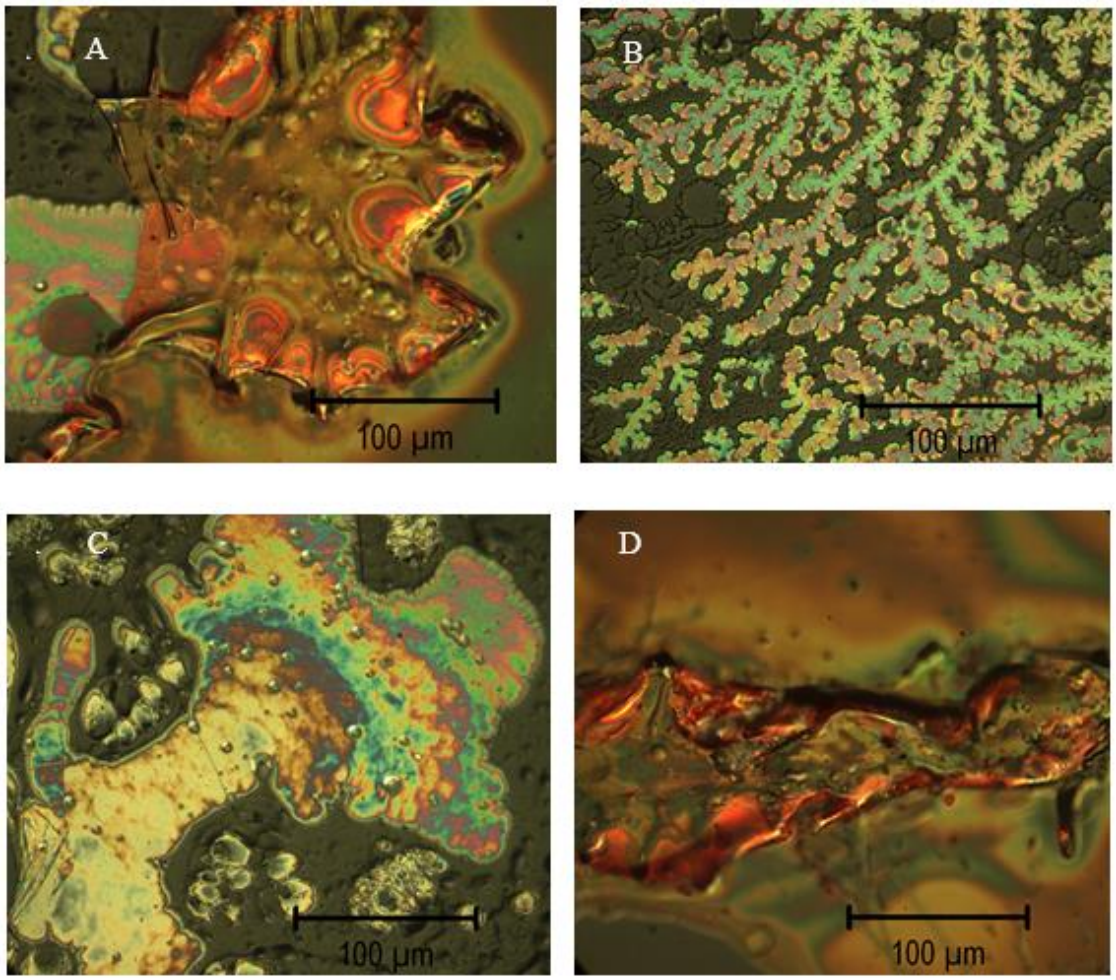

Figure 5-63: (A, B, C, D) optical micrographs of 20:80 (wt. %) polymer dispersed liquid crystal 5CB doped with chitosan.

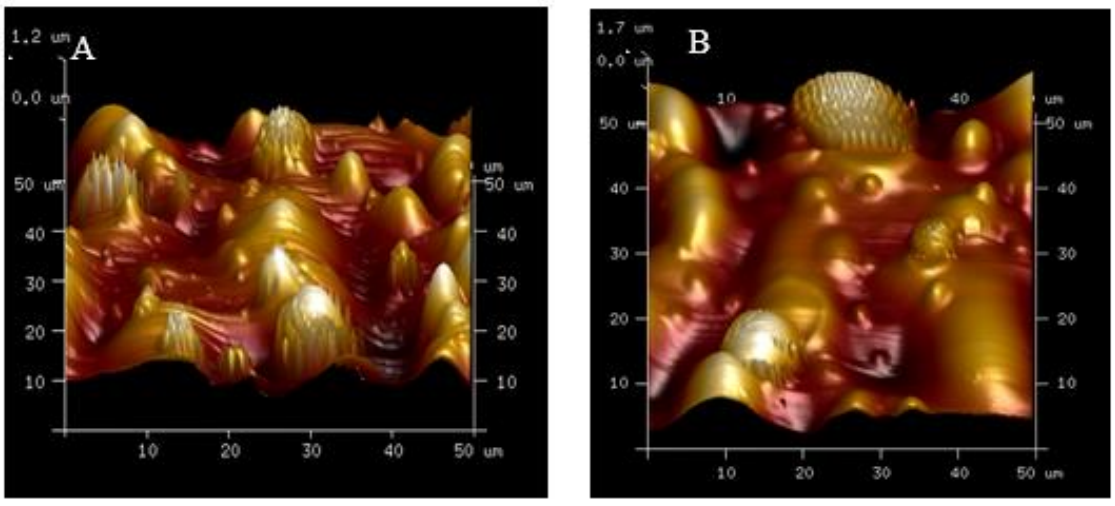

Figure 5-64: (A and B) AFM micrographs of 20:80 polymer dispersed liquid crystal 5CB doped with chitosan.

Figure (5-65) below shows a photograph of the electro optical cell used in the experiments. The cell construction is discussed later in this chapter. The wires shown in this figure were used to apply the electric field and were attached using silver dag.

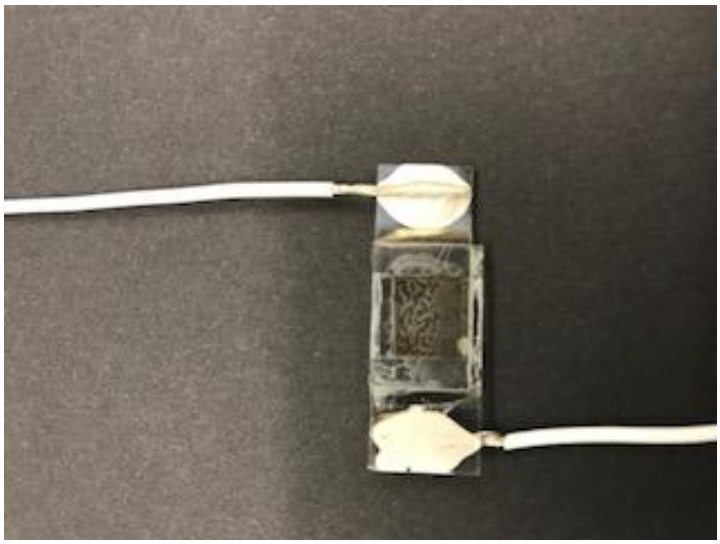

Figure 5-65: The cell of PDLC (5CB doped with chitosan) doped with SBB dye.

Figure (5-66) shows a HeNe laser probe beam that is incident on a viewing screen after the light beam passed through the LC cell Figure (5-65) containing 5CB LC doped with SBB dye. The cell cavity used in the experiment was 10 μm in length. A relatively small cavity length cavity was chosen so that a large electric field could be applied at a small applied voltage. We note two effects in the figures that are of interest. In both figures A and B there are concentric rings forming around the central laser spot. In Figure (5-66B) we observe diffraction orders, along a horizontal plane. The diffracted orders are formed by the grating that has been inscribed by the interference of the overlapping HeNe writing beams. The ±1 and ±2 orders can be seen in the photograph. As can be seen the intensity deceases with increasing diffraction order. We interpret the concentric rings as being due to nonlinear response of the refractive index and the Gaussian spatial HeNe beam. On application of an electric field the rings were seen to vanish at 3±0.1

Volts. This corresponds to an electric field strength of 3×10^5 Vm^{-1}. Similar rings patterns have been previously seen in publications and are thought to be due to the Freedericksz transition [345] or due to a nonlinear effects [346].

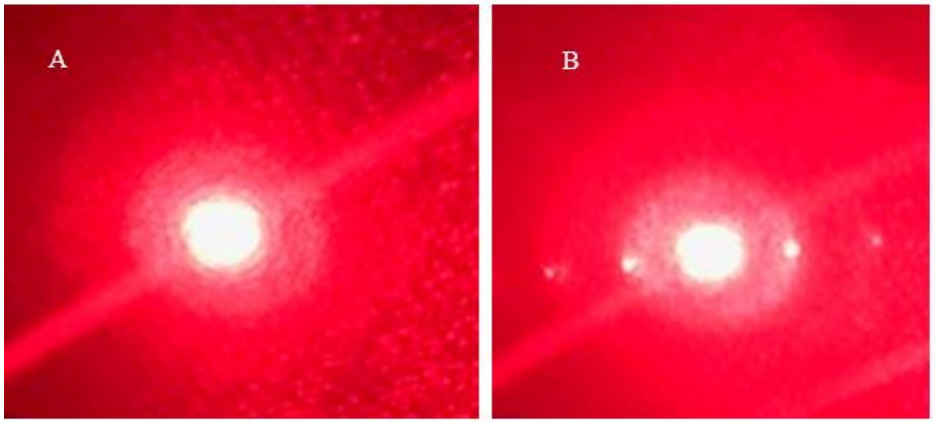

Figure 5-66: Photographic images of the viewing screen showing concentric rings centered around the central HeNe laser probe beam. Both figures show a ring pattern produced when the cell is applied with 3 volts across the LC cell. Figure A is shown without the HeNe intersecting writing beams. Figure B has the same conditions as in (A) but with addition of two interfering HeNe beams used for inscribing a grating inside the cell. One can observe in a horizontal direction the ±1 and ±2 diffraction orders. The cell thickness along the beam direction is 10 µm

Table 5-2: The experimental values of the 5CB doped with SBB dye.

Properties	Value
Voltage threshold (V)	3.0±0.1
Electric field threshold (Vm^{-1})	$3.0\pm0.1\times10^5$
Elastic constant (N)	1.06×10^{-10}

The Freedricksz transition of 5CB LC doped with SBB dye was determined to be 6.2 V [106]. This corresponds to an electric field of 3.1×10^5 Vm^{-1} for the 20 µm thick cell used in the experiment. This is a good agreement with the obtained value in this work. The rings formation reached a maximum diameter at an electric field of 5×10^5 Vm^{-1} and vanished when an electric field was applied at 6×10^5 Vm^{-1} and above. On sussation of the electric field the rings remained for an estimated 5 seconds before vanishing. It can be

seen in figure (5-66B) there are the ±1 and ±2 diffraction orders positioned along an almost horizontal direction. The diffraction orders occurred after 25 minutes after switching on the HeNe intersecting grating inscribing beam. The grating period was calculated using the order spacing and the geometry of the experimental setup and corresponded to a grating period of 16 μm. This value has a good agreement with grating period calculated by equation (4-1) which corresponded to 15 μm. The grating orders with the highest contrast was observed at an applied voltage of 5 V, this corresponds to an applied electric field of 5×10^5 Vm^{-1}. The formation of the diffraction grating can be explained qualitatively as being due to alignment of the LC molecules along the interfering fringes that have the higher intensity.

Application of an electric field has the effect of assisting the alignment as shown in the illustration figure (5-66). We refer to these two processes as the optical field and the electric field. Turning our attention to the ring patterns around the HeNe probe beam. The power of the probe beam was 1 mW and had a typical Gaussian beam with a diameter of 1 mm. Therefore, the central on-axis part of the beam has the highest intensity. The refractive index of the LC is highly birefringent and its value is dependent on the laser beam intensity according to the relation $(\Delta n = n_2 I)$, where $\Delta n = n_e - n_0$, n_e and n_0 are the extraordinary and ordinary parts of refractive index respectively, n_2 is the nonlinear coefficient and *I* corresponds to the HeNe beam intensity. Therefore, a higher intensity will have a higher refractive index. Moreover, the refractive index will reach the highest value in the central portion of the Gaussian beam while out towards the wings of the Gaussian the refractive index decreases. Consequently, there is a change in the phase of the propagating wave and rings will form due to constructive and destructive interference occurring. In this experiment there is therefore two processes taking place. Ring

formation due to the spatial dependent refractive index and there is a grating formed due to the intersecting inscribing HeNe beam. From this information we can calculate the birefringence (Δn) using the equation $\left(\Delta n = \frac{N\lambda}{d}\right)$ [346]. Using the corresponding information, where N is the number of observed rings the birefringence is calculated to be 0.126, λ is the wavelength 632.8 nm and d is the cell thickness which is 10 μm. Similarly, rings patterns generated on the 5CB doped with methyl red dye (MR) as self-phase modulation (SPM) have been reported using Nd:YVO_2 laser operating at a wavelength of 532 nm [346]. The concentric rings represented by the figure (6-16A and B) could back to Freedericksz transition in the liquid crystal molecules. This transition is a result of the contribution between the alignment of the molecules director at the surface and the boundary of the cell. The molecular director can be induced within the sample by applying a sufficient electric field or magnetic field [188]. Regarding the diffraction order represented by the dots in the figure (6-16B), these diffraction grating can be produced by irradiating the liquid crystal with polarized light. The optical field of the light impinging the sample controls the orientation of the liquid molecules to generate the phase grating of the liquid crystal material.

A set of experiments were carried out on PDLC doped with SBB dye with the aim of realising an electro-optic tunable diffraction grating the results of which are discussed. Photographs of the images recorded on a viewing screen are shown in figure (5-67 A and B): (A) the incident probe beam on the viewing screen after passing through the cell without the writing beam. (B) images on the viewing screen when the writing beams are switched on for a cell of PDLC doped with SBB dye and with an applied electric field. There is some evidence of faint, low contrast circles around the incident probe beams for both images A and B.

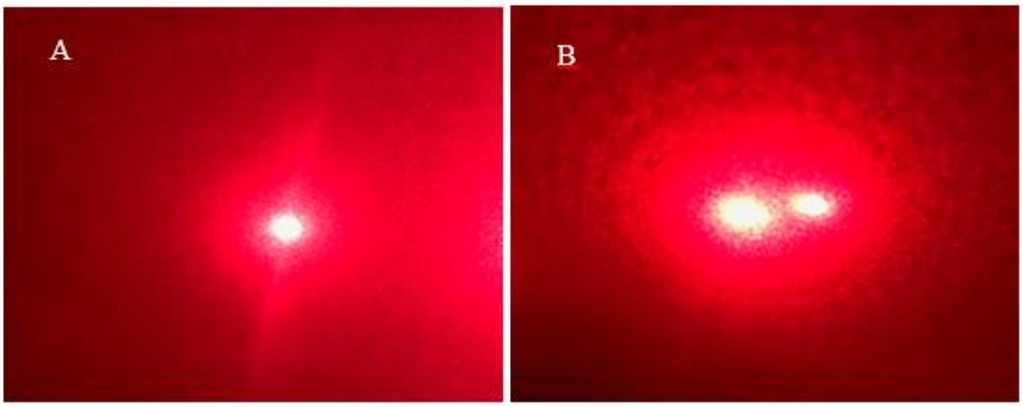

Figure 5-67: (A) the incident probe beam on the viewing screen after propagating the cell containing PDLC (5CB doped with chitosan) and with doped with SBB dye. (B) The incident of writing beams on the viewing screen after propagating the cell. All these images were under applying electric field. The thickness of the cell is 10 µm.

SEM micrographs of the surface of the PDLC (5CB doped with chitosan) doped with dye after probing with a HeNe, whilst applying an electric field are shown in figure (5-68A and B). It was observed that the suspension of PDLC doped dye had solidified and had a silver color. However it is not known if the changes were due to the interaction with the HeNe laser, due to the application of the electric field or a combination of the two processes. Looking at figure (5-68A) there is also the appearance of cavities. The changes that have occurred to the material require more investigations to explain the related mechanism.

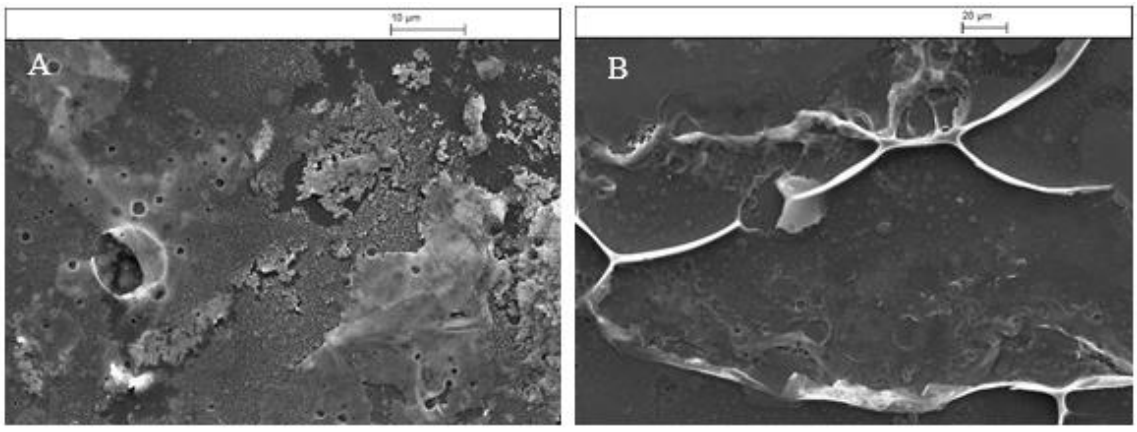

Figure 5-68: SEM micrographs of the surface of PDLC doped with SBB dye after probing with a HeNe laser and applying an electric field. The sample thickness is 10 µm. A magnification of ×5 was used, at a tilt angle of 0°, (B) ×1.5K magnification, and 0° tilt angle.

Figure (5-69, A and B) shows optical micrographs of PDLC doped SBB dye after probing the LC cell with a HeNe laser beam and applying an electric field across the material. It shows that there is a significant change in the distribution of 5CB LC dispersed in the biopolymer matrix and optical textures of the mixture.

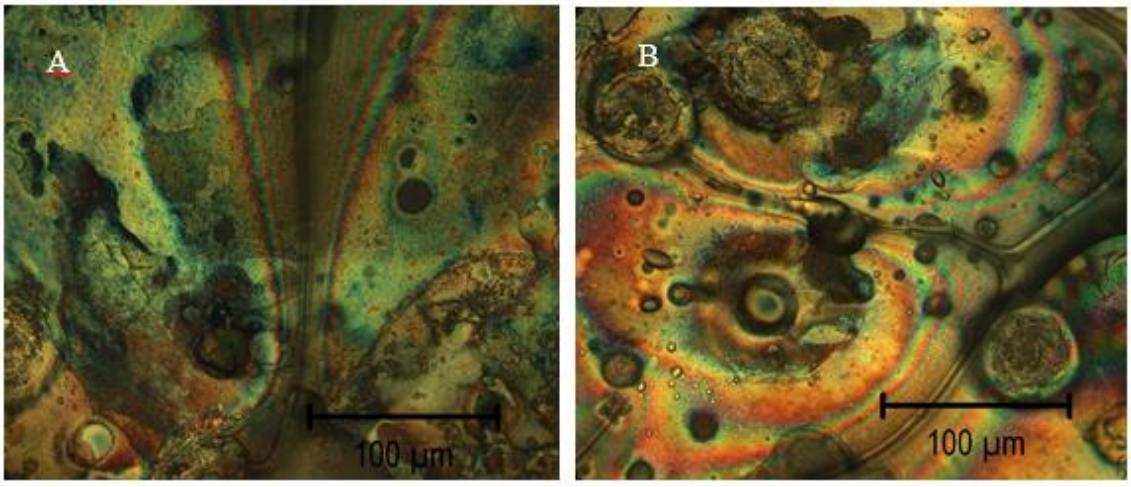

Figure 5-69: Optical micrographs of PDLC (5CB doped chitosan) doped Sudan black B (SBB) dye after probing with HeNe laser and applying an electric field.

The next set of experiments were intended to have a 5CB doped with SBB mixed with chitosan. Previous work on chitosan doped 5CB reported the miscibility [296]. An experiment was performed using the same experimental conditions as the non-chitosan experiment previously described. However the results did not yield a diffraction pattern and hence under the same conditions we concluded a diffraction grating had not been inscribed.

As has been mentioned above that filling the cell in thickness of 10 µm with the mixture of the PDLC doped chitosan and with SBB dye converted into a solid within a few minutes after interacting with the HeNe beams and applying a DC electric field. Although the refractive index and absorption coefficient were not measured and no values could be found in the literature it is expected that the optical properties for this set

of experiments are different to the previous one that had no chitosan present. The optical penetration depth at 632.8 nm, the refractive index and elastic constant will all be different. All of which will play a role in inscribing a grating. This does not however conclude that it is not possible to inscribe a grating in 5CB doped with SBB and chitosan. It may be that different experimental parameters are required in order to realise a grating. We discuss this further in the chapter on future work at the end of this thesis.

Conclusions

In conclusion, spin coated films of chitosan and agarose have been irradiated using an ArF laser emitting at a wavelength of 193 nm. An ablation threshold of 85±8 $mJcm^{-2}$ was determined from etch rate data. Thermo-gravimetric analysis measurements were carried out on chitosan and agarose to determine the thermal decomposition temperatures. These were identified as ~300°C and ~285°C for chitosan and agarose respectively and they are consistent with those found in the literature. Optical absorption is relatively high at a wavelength of 193 nm (6.4eV) for both chitosan and agarose; 3×10^{3} cm^{-1} and 1.67×10^{3} cm^{-1} respectively. Strong absorption is advantagious from a laser processing perspective as this permits high depth resolution per laser pulse. Close to the ablation threshold etch rates are typically 5 nm per pulse and increase with laser fluence.

It is often important to minimise thermal damage during the ablation process. Therefore to prevent or reduce denaturaion of chitosan and agarose adjacent to the irradiated sample it is recommended that laser processing is carried out at laser fluence close to the ablation threshold, namely, 110$mJcm^{-2}$ and 125 $mJcm^{-2}$ for chitosan and agarose respectively. Processing well above the laser ablation threshold initiates mechanical damage in the ablated regions. Inspection of laser ablation craters show evidence of foaming and cavity formation. The damage mechanism is tentatively explained as being due to a combination of thermal and photo-mechanical mechanisms. Atomic force microscopy and white light interferometry measurements confirm surface roughness of the ablated samples increase with laser fluence. Average roughness values, are at a nanometer level, typically Ra = 6 nm and Ra = 12 nm just above the ablation threshold where the surface changes.

Temperature rise simulations have been carried out using software using a finite element method, COMSOL^{TM} Multiphysics v5.3. Simulations show that the temperature rise in chitosan at laser fluence close to the laser ablation threshold is low, typically a rise of ~33°C at the surface. At elevated laser fluence, 760 mJcm^{-2} the temperature at the surface reaches the corresponding decomposition point of ~300°C for chitosan. Therefore for applications that require minimal damage and low surface roughness one should ideally process as close to the ablation threshold. However, there is a caveat to this and one may need to consider how much material and what is the aceptable surface roughness.

The shortest grating period fabricated uisng a laser direct writing method had grove periods of 12 µm for both chitosan and agarose. Optical microscopy and scanning electron microscopy measurements reveal clean ablation with the minimal redeposited material. On careful inspection there was some evidence of laser induced texturing occuring on the laser irradiated sites. However, further experiments would need to be carried out to determine whether or not the texturing was detrimental for a specific application. Laser processing results were promissing and this may open up new routes towards processing biocompatible materials. A laser interference lithography and the use of Schwarzchild objectives could be adopted to further decrease the grating period.

The ability to tune diffraction gratings either by changing the grove period or the ability to switch on and off a grating is of technological importance. Although there are several ways of achieving this we have investigated an electro-optical method using a liquid crystal namely 5CB. In this work we mixed Sudan Black B, (SBB) to increase the absorption of light at the inscription wavelength of 632.8 nm. This sample is identified as 5CB/SBB. A second sample was made by adding chitosan. This sample is therefore

refered to as 5CB/SBB/Chitosan. Two sets of experiments were carried using these samples, 5CB/SBB and 5C/SBB/Chitosan. The former was used as a reference and the latter, to our knowledge, has not been reported in the literature. A HeNe laser beam was split uisng a 50:50 cubic beam splitter and beams recombined to form interference fringes inside the samples. A set of experiments were carried out to investigate the effects of applying an eletric field normal to the sample surface whilst the grating inscription process is taking place. From the geometry of the interfering HeNe laser beams a fringe spacing of 15 μm was calculated. Light from an HeNe laser was switched on and an electric field of magnitude 5.1×10^{5} Vm^{-1} was applied at the same time. After 25 minutes the ±1 and ±2 diffrcation orders were observed on a viewing screen placed behind the sample. From these results we conclude the addition of SBB increased the optical absorption at the wavelength 632.8 nm and aided in the formation of a diffraction grating. The experiment was then repeated using a different sample, namely 5CB/SBB/Chitosan.

It is also worth noting that the 5CB/SBB/chitosan sample soldified after the experiment. A separate experiment revealed solidification occurred under the same conditions after 15 minutes. However, the mechanism of solidification was not investigated. The solidification may be due to a combination of factors. The interaction of light from the HeNe interacting with the chitosan may change the material structure or it may be due to the misibility between 5CB and SBB. Using the the same experimental conditions as those used for the 5CB/SBB sample it was not possible to observe a diffracting structure. The ratio of 5CB/SBB/Chitosan used in the experiment was 1:4:8 respecively and further experiments using different ratio’s of materials have been discussed for future experimental investigations.

To conclude, biocompatible materials chitosan and agarose have been processed using an ArF excimer laser. These materials can be sucessfully processed without casuing significant damage or contaniation from recondensed ablation products. Laser interference lithography has beeen adopted with the assistance of an electric field to form diffracting structures made from 5CB/SBB. However, forming a diffrcation grating out of 5CB/SBB/Chitosan require further investigations. Finally, this research has stimulated other related interests. The methods used here could be translated across to investigate other biocompatible materials. Similarly, it might be of inteerest to investigate the realisation and integration of other optical components.

CHAPTER 6.

6.1. Future works

The present work of this thesis has provided an essential knowledge of processing biocompatible materials using an ArF excimer laser operating at a wavelength of 193 nm. Moreover, producing diffraction grating made of biocompatible materials using different methods, mask projection and nanoimprinting have been reported. Also, creating an electric field diffraction grating formed of 5CB LC doped with dye and Polymer dispersed Liquid Crystal PDLC (5CB doped with chitosan) doped with dye has been investigated. Some future work have been suggested as follows:

1. One of the important goals of the future work is to minimize the grating period to achieve a submicron diffraction grating, and that can be made using a Schwarzschild objective lens.
2. Another future work goal is a generated grating period made of biocompatible materials films using Schwarzschild objective lens that can be employed for optical applications such as bio-sensor devices, grating coupler devices and Distributed Feedback laser (DFB).
3. Continuing with PDLC, 5CB doped with chitosan doped with dye to realise an electric field diffraction grating. In this regard, different concentrations of 5CB doped with chitosan then doped with dye should be investigated. Also, a cell with different thicknesses can be prepared for these experiments.
4. Silk fibroin is the next biocompatible material needs to be characterized and processed with ArF_2 excimer laser 193 nm wavelength. First, establishing the ablation threshold at 193 nm laser then generating a diffraction grating with submicron period to be employed for optical and medical applications.

REFERENCES

[1] Nielsen SE. Laser material processing of polymers. Polym Test 1983;3:303–10. doi:10.1016/0142-9418(83)90015-6.

[2] Kim J, Xu X. Excimer laser fabrication of polymer microfluidic devices. J Laser Appl 2003;15:255.

[3] Sionkowska a., Kaczmarek H, Wisniewski M, Skopinska J, Lazare S, Tokarev V. The influence of UV irradiation on the surface of chitosan films. Surf Sci 2006;600:3775–9. doi:10.1016/j.susc.2006.01.090.

[4] Castillejo M, Ezquerra TA, Martín M, Oujja M, Pérez S, Rebollar E. Laser nanostructuring of polymers: Ripples and applications. AIP Conf Proc 2012;1464:372–80. doi:10.1063/1.4739891.

[5] Zamiri R, Azmi BZ, Naseri MG, Ahangar HA, Darroudi M, Nazarpour FK. Laser based fabrication of chitosan mediated silver nanoparticles. Appl Phys A Mater Sci Process 2011;105:255–9. doi:10.1007/s00339-011-6525-7.

[6] P??rez S, Rebollar E, Oujja M, Mart??n M, Castillejo M. Laser-induced periodic surface structuring of biopolymers. Appl Phys A Mater Sci Process 2013;110:683–90. doi:10.1007/s00339-012-7186-x.

[7] Click M. Fabrication of porous biopolymer substrates for cell growth by UV laser: the role of pulse duration Marta Castillejo * , Esther Rebollar, Mohamed Oujja, Mikel Sanz n.d.

[8] Ihlemann J, Muller S, Puschmann S, Schafer D, Wei M, Li J, et al. Fabrication of submicron gratings in fused silica by F2-laser ablation. Appl Phys A Mater Sci Process 2003;76:751–3. doi:10.1007/s00339-002-1467-8.

[9] Phillips HM, Callahan DL, Sauerbrey R, Szab?? G, Bor Z. Sub-100 nm lines produced by direct laser ablation in polyimide. Appl Phys Lett 1991;58:2761–3. doi:10.1063/1.104778.

[10] Kim DY, Tripathy SK, Li L, Kumar J. Laser-induced holographic surface relief gratings on nonlinear optical polymer films. Appl Phys Lett 1995;66:1166–8. doi:10.1063/1.113845.

[11] Pissadakis S, Reekie L, Hempstead M, Zervas MN, Wilkinson JS. Ablated gratings on borosilicate glass by 193-nm excimer laser radiation. Appl Phys A Mater Sci Process 1999;69:739–41. doi:10.1007/s003399900244.

[12] Guo W, Holmberg P, Laurell F, Fokine M. Fabrication of long-period fiber gratings through periodic ablation using a focused CO_2-laser beam. Opt Mater Express 2015;5:2702. doi:10.1364/OME.5.002702.

[13] Pantelic D, Savic S. Biopolymer holographic diffraction gratings 2008;30:1205–7. doi:10.1016/j.optmat.2007.05.056.

[14] Ramanujam PS. Optical fabrication of nano-structured biopolymer surfaces. Opt Mater (Amst) 2005;27:1175–7. doi:10.1016/j.optmat.2004.08.079.

[15] Refojo MF. Application of Materials in Medice and Dentistry: Ophthalmologic Applications. 1996. doi:10.1016/B978-0-08-087780-8.00148-0.

[16] Hashemi P, Zarjani RA. A wide range pH optical sensor with mixture of Neutral Red and Thionin immobilized on an agarose film coated glass slide. Sensors Actuators, B Chem 2008;135:112–5. doi:10.1016/j.snb.2008.08.010.

[17] Mercey E, Obeïd P, Glaise D, Calvo-Muñoz ML, Guguen-Guillouzo C, Fouqué B. The application of 3D micropatterning of agarose substrate for cell culture and in situ comet assays. Biomaterials 2010;31:3156–65. doi:10.1016/j.biomaterials.2010.01.020.

[18] Bariáin C, Matías IR, Arregui FJ, López-Amo M. Optical fiber humidity sensor based on a tapered fiber coated with agarose gel. Sensors Actuators, B Chem 2000;69:127–31. doi:10.1016/S0925-4005(00)00524-4.

[19] Qiu Z-Y, Chen C, Wang X-M, Lee I-S. Advances in the surface modification techniques of bone-

related implants for last 10 years. Regen Biomater 2014;1:67–79. doi:10.1093/rb/rbu007.

[20] Wu G, Li P, Feng H, Zhang X, Chu PK. Engineering and functionalization of biomaterials via surface modification. J Mater Chem B 2015;3:2024–42. doi:10.1039/C4TB01934B.

[21] Bazaka K, Jacob M V., Crawford RJ, Ivanova EP. Plasma-assisted surface modification of organic biopolymers to prevent bacterial attachment. Acta Biomater 2011;7:2015–28. doi:10.1016/j.actbio.2010.12.024.

[22] Jiao YP, Cui FZ. Surface modification of polyester biomaterials for tissue engineering. Biomed Mater 2007;2. doi:10.1088/1748-6041/2/4/R02.

[23] Kulkarni V, Butte K, Rathod S. Natural Polymers – A Comprehensive Review. Int J Res Pharm Biomed Sci 2012;3:1597–613.

[24] Kaushik K., Sharma R.B, Agarwal S. Natural polymers and their applications. Int J Pharm Sci Rev Res 2016;37:30–36.

[25] He X, Zhong L, Wang G, Liao Y, Liu Q. Tribological behavior of femtosecond laser textured surfaces of 20CrNiMo/beryllium bronze tribo-pairs. Ind Lubr Tribol 2015;67:630–8. doi:10.1108/ILT-03-2015-0042.

[26] Yang Y. Recent Advances on Surface Modification of Halloysite Nanotubes for Multifunctional Applications. Appl Sci 2017;7:1215. doi:10.3390/app7121215.

[27] Dhandayuthapani B, Yoshida Y, Maekawa T, Kumar DS. Polymeric scaffolds in tissue engineering application: A review. Int J Polym Sci 2011;2011. doi:10.1155/2011/290602.

[28] Hunt JA, Williams RL, Tavakoli SM, Riches ST. Laser surface modification of polymers to improve biocompatibility. J Mater Sci Mater Med 1995;6:813–7. doi:10.1007/BF00134323.

[29] Heitz J, Barb RA, Sajdl P, Svorˇ V. Applied Surface Science Comparison of KrF and ArF excimer laser treatment of biopolymer surface ˇ 2015;339:144–50. doi:10.1016/j.apsusc.2015.02.137.

[30] Wisniewski M, Sionkowska A, Kaczmarek H, Skopinska J, Lazare S, Tokarev V. The influence of KrF excimer laser irradiation on the surface of collagen and collagen/PVP films. Int J Photoenergy 2006;2006:1–7. doi:10.1155/IJP/2006/35126.

[31] Srinivasan R, Braren B, Dreyfus RW, Hadel L, Seeger DE. Mechanism of the ultraviolet laser ablation of polymethyl methacrylate at 193 and 248 nm: laser-induced fluorescence analysis, chemical analysis, and doping studies. J Opt Soc Am B 1986;3:785. doi:10.1364/JOSAB.3.000785.

[32] Skordoulis CD, Makropoulou MI, Bolovinos AL, Serafetinides AA. Xecl Laser Ablation of Biocompatible Ptfe Studied By Photothermal Beam Deflection. Lasers Med Sci 1997;12:313–9.

[33] Vogel A, Venugopalan V. Mechanisms of pulsed laser ablation of biological tissues. Chem Rev 2003;103:577–644. doi:10.1021/cr010379n.

[34] Lazare S, Tokarev VN, Sionkowska A, Wi'sniewski M. Negative pressure model for surface foaming of collagen and other biopolymer films by KrF laser ablation. J Phys Conf Ser 2007;\bf{59}:543–7. doi:10.1088/1742-6596/59/1/116.

[35] Lazare S, Bonneau R, Gaspard S, Oujja M, Sionkowska A, Castellejo M. Modeling the dynamics of one laser pulse surface nanofoaming of biopolymers. Appl Phys A Mater Sci Process 2009;94:719–29. doi:10.1007/s00339-008-4950-z.

[36] Gaspard S, Oujja M, de Nalda R, Abrusci C, Catalina F, Bañares L, et al. Nanofoaming in the surface of biopolymers by femtosecond pulsed laser irradiation. Appl Surf Sci 2007;254:1179–84. doi:10.1016/j.apsusc.2007.09.099.

[37] Pettit GH, Ediger MN. Corneal-tissue absorption coefficients for 193- and 213-nm ultraviolet radiation. Appl Opt 1996;35:3386–91. doi:10.1364/AO.35.003386.

[38] Puliafito CA, Steinert RF, Deutsch TF, Hillenkamp F, Dehm EJ, Adler CM. Excimer Laser Ablation of the Cornea and Lens: Experimental Studies. Ophthalmology 1985;92:741–8. doi:10.1016/S0161-6420(85)33962-3.

[39] Srinivasan R, Braren B, Dreyfus RW, Hadel L, Seeger DE. Mechanism of the ultraviolet laser ablation of polymethyl methacrylate at 193 and 248 nm: laser-induced fluorescence analysis, chemical analysis, and doping studies. J Opt Soc Am B 1986;3:785. doi:10.1364/JOSAB.3.000785.

[40] Rothschild M, Horn MW, Keast CL, Kunz RR, Palmateer SC, Doran SP, et al. Photolithography at 193 nm. Lincoln Lab J 1997;10:19–34. doi:10.1.1.69.2253.

[41] Huang W, Pu D, Yang X, Wei G, Fang Z, Zhou X, et al. A high-order external distributed feedback polymer laser with low working threshold. J Phys D Appl Phys 2016;49:175106. doi:10.1088/0022-3727/49/17/175106.

[42] Paterson J, Natansohn a., Rochon P, Callender CL, Robitaille L. Optically inscribed surface relief diffraction gratings on azobenzene-containing polymers for coupling light into slab waveguides. Appl Phys Lett 1996;69:3318–20. doi:10.1063/1.117292.

[43] Palmer C. Diffraction Grating Handbook. J Opt Soc Am 2005;46:271. doi:10.1364/JOSA.46.000050.

[44] Lenhert S, Brinkmann F, Laue T, Walheim S, Vannahme C, Klinkhammer S, et al. Lipid multilayer gratings. Nat Nanotechnol 2010;5:275–9. doi:10.1038/nnano.2010.17.

[45] Squires AD, Constable E, Lewis RA. 3D Printed Terahertz Diffraction Gratings And Lenses. J Infrared, Millimeter, Terahertz Waves 2014;36:72–80. doi:10.1007/s10762-014-0122-8.

[46] Dyer PE, Maswadi SM, Walton CD, Ersoz M, Fletcher PDI, Paunov VN. 157-nm laser micromachining of N-BK7 glass and replication for microcontact printing. Appl Phys A Mater Sci Process 2003;77:391–4. doi:10.1007/s00339-002-1936-0.

[47] Hermann S, Shallcross RC, Meerholz K. Simple Fabrication of an Organic Laser by Microcontact Molding of a Distributed Feedback Grating. Adv Mater 2014;26:6019–24. doi:10.1002/adma.201401616.

[48] Ihlemann J, Müller S, Puschmann S, Schäfer D, Wei M, Li J, et al. Fabrication of submicron gratings in fused silica by F2-laser ablation. Appl Phys A Mater Sci Process 2003;76:751–3. doi:10.1007/s00339-002-1467-8.

[49] Meinertz J, Fricke-Begemann T, Ihlemann J. Micron and sub-micron gratings on glass by UV laser ablation. Phys Procedia 2013;41:708–12. doi:10.1016/j.phpro.2013.03.137.

[50] Dyer PE, Farley RJ, Giedl R, Karnakis DM. Excimer laser ablation of polymers and glasses for grating fabrication. Appl Surf Sci 1996;96–98:537–49. doi:10.1016/0169-4332(95)00528-5.

[51] Arnold CB, Piqué A. L aser Direct-Write Processing. MRS Bull 2007;32:9–15. doi:10.1557/mrs2007.9.

[52] Senechal M, Press C. Advanced 1997:996–7.

[53] Chung S-H, Noh HY. Polymer-dispersed liquid crystal devices with graphene electrodes. Opt Express 2015;23:32149. doi:10.1364/OE.23.032149.

[54] Drzaic PS. Polymer dispersed liquid crystals for high efficiency displays Paul n.d.;2:1–2.

[55] Montgomery GP, Vaz N a. Contrast ratios of polymer-dispersed liquid crystal films. Appl Opt 1987;26:738–43. doi:10.1364/AO.26.000738.

[56] Lin YH, Ren H, Wu ST. High contrast polymer-dispersed liquid crystal in a 90° twisted cell. Appl Phys Lett 2004;84:4083–5. doi:10.1063/1.1753052.

[57] Neto AMF. Nonlinear Optical Properties of Liquid Crystals Probed by Z-scan Technique The Z-scan technique. Brazilian J Phys 2003;33:813–20.

[58] Khoo I-C. Liquid Crystals. vol. 22. 2007. doi:10.1002/0470084030.

[59] Chen Y-D, Fuh AY-G, Cheng K-T. Particular thermally induced phase separation of liquid crystal and poly (N-vinyl carbazole) films and its application. Opt Express 2012;20:16777–84.

[60] Fuh AY-G, Chen C-C, Liu C-K, Cheng K-T. Polarizer-free, electrically switchable and optically rewritable displays based on dye-doped polymer-dispersed liquid crystals. Opt Express

2009;17:7088–94. doi:10.1364/OE.17.007088.

[61] Nieto D, Ezequiel Á, Flores-arias MT. Laser Surface Microstructuring of Biocompatible Materials Using a Microlens Array and the Talbot Effect: Evaluation of the Cell Adhesion. Materials (Basel) 2017. doi:10.3390/ma10020214.

[62] Applegate M, Partlow BP, Coburn J, Moreau J, Marelli B, Kaplan D, et al. 3D Laser Ablation of Biocompatible Silk Fibroin Hydrogels for Biomedical Applications. Cleo 2015 2015:STh3M.5. doi:10.1364/CLEO_SI.2015.STh3M.5.

[63] Makropoulou M, Serafetinides AA, Skordoulis CD. Ultra-violet and infra-red laser ablation studies of biocompatible polymers. Lasers Med Sci 1995;10:201–6. doi:10.1007/BF02133332.

[64] Module SP. Short Pulse Module 2013;3052:7002.

[65] Nikogosyan DN, Görner H. Towards the laser photochemistry of the cornea: Studies of the most common and highly absorbing aliphatic amino acids in collagen. J Photochem Photobiol B Biol 1998;47:63–7. doi:10.1016/S1011-1344(98)00204-8.

[66] Lazare S, Sionkowska A, Zaborowicz M, Planecka A, Lopez J, Dijoux M, et al. Bombyx mori silk protein films microprocessing with a nanosecond ultraviolet laser and a femtosecond laser workstation: Theory and experiments. Appl Phys A Mater Sci Process 2012;106:67–77. doi:10.1007/s00339-011-6639-y.

[67] Slepička P, Michaljaničová I, Sajdl P, Fitl P, Švorčík V. Surface ablation of PLLA induced by KrF excimer laser. Appl Surf Sci 2013;283:438–44. doi:10.1016/j.apsusc.2013.06.127.

[68] Strong J. The Johns Hopkins University and Diffraction Gratings. J Opt Soc Am 1960;50:1148. doi:10.1364/JOSA.50.001148.

[69] Zhang S, Liu Y, Qian Y, Li W, Juvert J, Tian P, et al. Manufacturing with light - micro-assembly of opto-electronic microstructures. Opt Express 2017;25:28838. doi:10.1364/OE.25.028838.

[70] Zero-order diffractive microstructures for security applications M.T. Gale, K. Knop and R. Morf Paul Scherrer Institute, Zurich, Switzerland 1990;1210:83–9.

[71] Folch a, Ayon a, Hurtado O, Schmidt M a, Toner M. Molding of deep polydimethylsiloxane microstructures for microfluidics and biological applications. J Biomech Eng 1999;121:28–34. doi:10.1115/1.2798038.

[72] Danilevicius P. Micro-structured polymer scaffolds fabricated by direct laser writing for tissue engineering. J Biomed Opt 2012;17:81405. doi:10.1117/1.JBO.17.8.081405.

[73] Tiefenthaler K, Lukosz W. Grating couplers as integrated optical humidity and gas sensors. Thin Solid Films 1985;126:205–11. doi:10.1016/0040-6090(85)90312-8.

[74] Liang T, Ziolkowski RW. Grating assisted waveguide-to-waveguide couplers. IEEE Photonics Technol Lett 1998;10:693–5. doi:10.1109/68.669328.

[75] Vörös J, Ramsden JJ, Csúcs G, Szendro I, De Paul SM, Textor M, et al. Optical grating coupler biosensors. Biomaterials 2002;23:3699–710. doi:10.1016/S0142-9612(02)00103-5.

[76] Taillaert D, Bogaerts W, Bienstman P, Krauss TF, Van Daele P, Moerman I, et al. An out-of-plane grating coupler for efficient butt-coupling between compact planar waveguides and single-mode fibers. IEEE J Quantum Electron 2002;38:949–55. doi:10.1109/JQE.2002.1017613.

[77] Eriksson N, Hagberg M, Larsson A. Highly directional grating outcouplers with tailorable radiation characteristics. IEEE J Quantum Electron 1996;32:1038–47. doi:10.1109/3.502382.

[78] Ang TW, Reed GT, Vonsovici A, Evans AGR, Routley PR, Josey MR. Effects of grating heights on highly efficient unibond SOI waveguide grating couplers. IEEE Photonics Technol Lett 2000;12:59–61. doi:10.1109/68.817493.

[79] Dong P, Kirk AG. Compact double-grating coupler between vertically stacked silicon-on-insulator waveguides. Appl Opt 2005;44:7540–7. doi:10.1117/12.527965.

[80] Mulé A V, Villalaz R, Gaylord TK, Meindl JD. Quasi-free-space optical coupling between diffraction grating couplers fabricated on independent substrates. Appl Opt 2004;43:5468–75. doi:10.1364/AO.43.005468.

[81] Brazas JC, Li L, McKeon AL. High-efficiency input coupling into optical waveguides using gratings with double-surface corrugation. Appl Opt 1995;34:604–9. doi:10.1364/AO.34.000604.

[82] Taillaert D, Van Laere F, Ayre M, Bogaerts W, Van Thourhout D, Bienstman P, et al. Grating couplers for coupling between optical fibers and nanophotonic waveguides. Japanese J Appl Physics, Part 1 Regul Pap Short Notes Rev Pap 2006;45:6071–7. doi:10.1143/JJAP.45.6071.

[83] Zhang C, Sun J-H, Xiao X, Sun W-M, Zhang X-J, Chu T, et al. High Efficiency Grating Coupler for Coupling between Single-Mode Fiber and SOI Waveguides. Chinese Phys Lett 2013;30:14207. doi:10.1088/0256-307X/30/1/014207.

[84] Li C, Zhang H, Yu M, Lo GQ. CMOS-compatible high efficiency double-etched apodized waveguide grating coupler. Opt Express 2013;21:7868. doi:10.1364/OE.21.007868.

[85] Liu R, Wang Y, Yin D, Ye H, Yang X, Han Q. A high-efficiency grating coupler between single-mode fiber and silicon-on-insulator waveguide. J Semicond 2017;38:54007. doi:10.1088/1674-4926/38/5/054007.

[86] Hagberg M, Eriksson N, Kjellberg T, Larsson a. Dependence of output coupling efficiency on detuning in surface grating output couplers. Opt Lett 1995;20:180–2. doi:10.1364/OL.20.000180.

[87] Galan J V., Sanchis P, Blasco J, Marti J. Study of high efficiency grating couplers for silicon-based horizontal slot waveguides. IEEE Photonics Technol Lett 2008;20:985–7. doi:10.1109/LPT.2008.923546.

[88] Mathews CB, Libish TM, Biswas P, Bandyopadhyay S, Dasgupta K, Radhakrishnan P. A Chitosan coated Fiber Optic Long Period Grating Biosensor for the Detection and Estimation of Cholesterol 2014:12–4.

[89] Mathews CB, Libish TM, Kaushalkumar B, Vivek V, Prabhu R, Radhakrishnan P. A fiber optic biosensor for the detection of cholesterol levels based on chitosan coated long period grating. Optoelectron Lett 2016;12:23–6. doi:10.1007/s11801-016-5229-9.

[90] Dubas ST, Iamsamai C, Potiyaraj P. Optical alcohol sensor based on dye-Chitosan polyelectrolyte multilayers. Sensors Actuators, B Chem 2006;113:370–5. doi:10.1016/j.snb.2005.03.032.

[91] Aldana AA, Barrios B, Strumia M, Correa S, Martinelli M. Dendronization of chitosan films: Surface characterization and biological activity. React Funct Polym 2016;100:18–25. doi:10.1016/j.reactfunctpolym.2016.01.003.

[92] Xin-Yuan S. New Contact Lens Based on Chitosan/Gelatin Composites. J Bioact Compat Polym 2004;19:467–79. doi:10.1177/0883911504048410.

[93] Behl G, Iqbal J, O'Reilly NJ, McLoughlin P, Fitzhenry L. Synthesis and Characterization of Poly(2-hydroxyethylmethacrylate) Contact Lenses Containing Chitosan Nanoparticles as an Ocular Delivery System for Dexamethasone Sodium Phosphate. Pharm Res 2016;33:1638–48. doi:10.1007/s11095-016-1903-7.

[94] Jayakumar R, Reis RL, Mano JF. Chemistry and applications of phosphorylated chitin and chitosan. E-Polymers 2006:1–16. doi:035.

[95] Kumar M. A review of chitin and chitosan applications. React Funct Polym 2000;46:1–27. doi:10.1016/S1381-5148(00)00038-9.

[96] Mironenko AY, Sergeev AA, Nazirov AE, Modin EB, Voznesenskiy SS, Bratskaya SY. H2S optical waveguide gas sensors based on chitosan/Au and chitosan/Ag nanocomposites. Sensors Actuators, B Chem 2016;225:348–53. doi:10.1016/j.snb.2015.11.073.

[97] Chen LH, Li T, Chan CC, Menon R, Balamurali P, Shaillender M, et al. Chitosan based fiber-optic Fabry-Perot humidity sensor. Sensors Actuators, B Chem 2012;169:167–72. doi:10.1016/j.snb.2012.04.052.

[98] Yoon SH, Jeong WT, Kim KC, Kim KJ, Oh MC, Lee SM. Development of the Biopolymeric Optical Planar Waveguide with Nanopattern. J Surf Eng Mater Adv Technol 2011;1:56–61. doi:10.4236/jsemat.2011.12009.

[99] Waldhäusl R, Schnabel B, Dannberg P, Kley E-B, Bräuer A, Karthe W. Efficient Coupling into Polymer Waveguides by Gratings. Appl Opt 1997;36:9383. doi:10.1364/AO.36.009383.

[100] Waldausl R, Schnabel B, Kley E, Brauer A. Efficient focusing polymer waveguide grating couplers. Electron Lett 1997;33:623–4.

[101] Voznesenskiy SS, Sergeev AA, Kulchin YN, Mironenko AY, Bratskaya SY. Nanostructured Biopolymer Systems for Optical Sensing Applications. Physics, Chem Appl Nanostructures Rev Short Notes 2013:595–8.

[102] Jain A, Yang AHJJ, Erickson D. Gel-based optical waveguides with live cell encapsulation and integrated microfluidics. Opt Lett 2012;37:1472–4. doi:10.1364/OL.37.001472.

[103] Doane JW, Golemme A, West JL, Whitehead JB, Wu B-G. Polymer Dispersed Liquid Crystals for Display Application. Mol Cryst Liq Cryst Inc Nonlinear Opt 1988;165:511–32. doi:10.1080/00268948808082211.

[104] S CRH, Bunning TJ, Natarajan L V, Tondiglia VP, Sutherland RL. Holographic Polymer Dispersed liquid 2000:83–115.

[105] A.JENNEY J. Holographic Recording with Photopolymers. J Opt Soc Am 1970;60:1155–61. doi:10.1364/JOSA.60.001155.

[106] Afshari H, Olyaeefar B, Khoshsima H. The refractive index grating formation in azo dye doped nematic liquid crystal. Mol Cryst Liq Cryst 2012;561:36–41. doi:10.1080/15421406.2012.686706.

[107] Pei Y, Yao F, Hou C, Sun X, Zhou Z. High diffraction efficiency and a quasi-permanent grating in photorefractive nematic liquid crystal at low temperature. Opt Lett 2005;30:631–3. doi:10.1364/OL.30.000631.

[108] d'Alessandro A, Asquini R, Gizzi C, Caputo R, Umeton C, Veltri A, et al. Electro-optic properties of switchable gratings made of polymer and nematic liquid-crystal slices. Opt Lett 2004;29:1405. doi:10.1364/OL.29.001405.

[109] Fuh AY-G, Chen W-K, Cheng K-T, Liu Y-C, Liu C-K, Chen Y-D. Formation of holographic gratings in polymer-dispersed liquid crystals using off-resonant light. Opt Mater Express 2015;5:774. doi:10.1364/OME.5.000774.

[110] Liu X, Chu PK, Ding C. Surface modification of titanium, titanium alloys, and related materials for biomedical applications. Mater Sci Eng R Reports 2004;47:49–121. doi:10.1016/j.mser.2004.11.001.

[111] Anitha A, Sowmya S, Kumar PTS, Deepthi S, Chennazhi KP, Ehrlich H, et al. Chitin and chitosan in selected biomedical applications. Prog Polym Sci 2014;39:1644–67. doi:10.1016/j.progpolymsci.2014.02.008.

[112] Nizamoglu S, Gather MC, Humar M, Choi M, Kim S, Kim KS, et al. Bioabsorbable polymer optical waveguides for deep-tissue photomedicine. Nat Commun 2016;7:1–7. doi:10.1038/ncomms10374.

[113] Applegate MB, Coburn J, Partlow BP, Moreau JE, Mondia JP, Marelli B, et al. Laser-based three-dimensional multiscale micropatterning of biocompatible hydrogels for customized tissue engineering scaffolds. Proc Natl Acad Sci 2015;112:12052–7. doi:10.1073/pnas.1509405112.

[114] Koh WG, Pishko M V. Fabrication of cell-containing hydrogel microstructures inside microfluidic devices that can be used as cell-based biosensors. Anal Bioanal Chem 2006;385:1389–97. doi:10.1007/s00216-006-0571-6.

[115] Praxedes APP, da Silva AJC, da Silva RC, Lima RPA, Tonholo J, Ribeiro AS, et al. Effects of UV irradiation on the wettability of chitosan films containing dansyl derivatives. J Colloid Interface Sci 2012;376:255–61. doi:10.1016/j.jcis.2012.02.056.

[116] Weibel DE, Michels AF, Feil AF, Amaral L, Teixeira SR, Horowitz F. Adjustable hydrophobicity of al substrates by chemical surface functionalization of nano/microstructures. J Phys Chem C 2010;114:13219–25. doi:10.1021/jp103702d.

[117] Scolaro C, Torrisi L, Cutroneo M, Velardi L. Wetting ability modifications in biocompatible polymers induced by pulsed lasers. J Phys Conf Ser 2014;508:1–6. doi:10.1088/1742-6596/508/1/012030.

[118] Tien NC, Jeong S, Phinney LM, Fushinobu K, Bokor J. Surface adhesion reduction in silicon microstructures using femtosecond laser pulses. Appl Phys Lett 1996;68:197–9. doi:10.1063/1.116458.

[119] Deepak KLN, Sai R, Kumar S, Rao DN, Rao SV. Microstructures and Diffraction Gratings in Poly (Dimethyl Siloxane) Fabricated Using Femtosecond Pulses 2009:2–5.

[120] Lee K, Asher SA. Photonic crystal chemical sensors: pH and ionic strength. J Am Chem Soc 2000;122:9534–7. doi:10.1021/ja002017n.

[121] Yan WG, Qi JW, Li Z Bin, Tian JG. Fabrication and Optical Properties of Au-Coated Polystyrene Nanosphere Arrays with Controlled Gaps. Plasmonics 2014;9:565–71. doi:10.1007/s11468-013-9665-0.

[122] Wu MH, Park C, Whitesides GM. Generation of submicrometer structures by photolithography using arrays of spherical microlenses. J Colloid Interface Sci 2003;265:304–9. doi:10.1016/S0021-9797(03)00311-4.

[123] Akashi T, Yoshimura Y. Deep reactive ion etching of borosilicate glass using an anodically bonded silicon wafer as an etching mask. J Micromechanics Microengineering 2006;16:1051–6. doi:10.1088/0960-1317/16/5/024.

[124] Gower MC, Davies E, Holmes a. S. Optical Modeling of Laser Ablation for Microstructure Fabrication. J Laser Micro/Nanoengineering 2013;8:56–64. doi:10.2961/jlmn.2013.01.0012.

[125] Tseng AA, Chen YT, Ma KJ. Fabrication of high-aspect-ratio microstructures using excimer laser. Opt Lasers Eng 2004;41:827–47. doi:10.1016/S0143-8166(03)00062-9.

[126] Chen KH, Wu W, Chu BH, Chang CY, Lin J, Pearton SJ, et al. UV excimer laser drilled high aspect ratio submicron via hole. Appl Surf Sci 2009;256:183–6. doi:10.1016/j.apsusc.2009.07.105.

[127] Rizvi N. Production of novel 3D microstructures using excimer laser mask projection techniques. Proc SPIE 1999.

[128] Guo LJ. Nanoimprint lithography: Methods and material requirements. Adv Mater 2007;19:495–513. doi:10.1002/adma.200600882.

[129] Chou S, Krauss P, Renstrom P. Imprint of sub-25nm vias and trenches in polymers. Appl Phys Lett 1995;67:3114. doi:10.1063/1.114851.

[130] Piner RD, Zhu J, Xu F, Hong S, Mirkin CA. "Dip-pen" nanolithography. Science (80-) 1999;283:661–3. doi:10.1126/science.283.5402.661.

[131] Salaita K, Wang Y, Mirkin CA. Applications of dip-pen nanolithography. Nat Nanotechnol 2007;2:145–55. doi:10.1038/nnano.2007.39.

[132] Santhanam V, Andres RP. Microcontact Printing of Uniform Nanoparticle Arrays. Nano Lett 2004;4:41–4. doi:10.1021/nl034851r.

[133] Boisen A, Birkelund K, Hansen O, Grey F. Fabrication of submicron suspended structures by laser and atomic force microscopy lithography on aluminum combined with reactive ion etching. J Vac Sci Technol B 1998;16:2977–81. doi:10.1116/1.590329.

[134] Hu S. Fabrication of silicon and metal nanowires and dots using mechanical atomic force lithography. J Vac Sci Technol B Microelectron Nanom Struct 1998;16:2822. doi:10.1116/1.590277.

[135] Hu S. Novel approach to atomic force lithography. J Vac Sci Technol B Microelectron Nanom Struct 1998;16:1983. doi:10.1116/1.590117.

[136] Heyderman LJ, Schift H, David C, Ketterer B, Auf der Maur M, Gobrecht J. Nanofabrication using hot embossing lithography and electroforming. Microelectron Eng 2001;57–58:375–80. doi:10.1016/S0167-9317(01)00436-1.

[137] Nakamura T, Nakagawa M. lithography with high-viscosity photo-curable resins n.d.:1–4.

[138] Bender M, Otto M, Hadam B, Spangenberg B, Kurz H. Multiple imprinting in UV-based nanoimprint lithography: Related material issues. Microelectron Eng 2002;61–62:407–13.

doi:10.1016/S0167-9317(02)00470-7.

[139] Chou SY. Sub-10 nm imprint lithography and applications. J Vac Sci Technol B Microelectron Nanom Struct 1997;15:2897. doi:10.1116/1.589752.

[140] Gourgon C, Perret C, Micouin G, Lazzarino F, Tortai JH, Joubert O, et al. Influence of pattern density in nanoimprint lithography. J Vac Sci Technol B Microelectron Nanom Struct 2003;21:98. doi:10.1116/1.1532735.

[141] Glinsner T, Kreindl G. Nanoimprint Lithography. Lithography 2010. doi:10.5772/8190.

[142] Grego S, Huffman A, Lueck M, Stoner BR, Lannon J. Nanoimprint lithography fabrication of waveguide-integrated optical gratings with inexpensive stamps. Microelectron Eng 2010;87:1846–51. doi:10.1016/j.mee.2009.11.003.

[143] Truskett VN, Watts MPC. Trends in imprint lithography for biological applications. Trends Biotechnol 2006;24:312–7. doi:10.1016/j.tibtech.2006.05.005.

[144] Li K, Morton K, Veres T, Cui B. Nanoimprint Lithography and Its Application in Tissue Engineering and Biosensing. Compr Biotechnol Second Ed 2011;5:126–39. doi:10.1016/B978-0-08-088504-9.00497-9.

[145] Yao Y, Liu H, Wang Y, Li Y, Song B, Bratkovsk A, et al. Nanoimprint lithography: an enabling technology for nanophotonics. Appl Phys A Mater Sci Process 2015;121:327–33. doi:10.1007/s00339-015-9438-z.

[146] Nie Z, Kumacheva E. Patterning surfaces with functional polymers. Nat Mater 2008;7:277–90. doi:10.1038/nmat2109.

[147] Gilmore JH. NIH Public Access. North 2008;29:1883–9. doi:10.3174/ajnr.A1256.Functional.

[148] Amsden BJJ, Domachuk P, Gopinath A, White RD, Negro LD, Kaplan DL, et al. Rapid Nanoimprinting of Silk Fibroin Films for Biophotonic Applications 2010:1–4. doi:10.1002/adma.200903166.

[149] Madhukumar R, Asha S, Lakshmeesha Rao B, Sarojini BK, Byrappa K, Wang Y, et al. Optical properties of γ-irradiated Bombyx mori silk fibroin films. Radiat Eff Defects Solids 2015;170:906–15. doi:10.1080/10420150.2015.1136309.

[150] Perry H, Gopinath A, Kaplan DL, Negro LD, Omenetto FG. Nano- and micropatterning of optically transparent, mechanically robust, biocompatible silk fibroin films. Adv Mater 2008;20:3070–2. doi:10.1002/adma.200800011.

[151] Ofir Y, Moran IW, Subramani C, Carter KR, Rotello VM. Nanoimprint lithography for functional three-dimensional patterns. Adv Mater 2010;22:3608–14. doi:10.1002/adma.200904396.

[152] Hoff JD, Cheng LJ, Meyhöfer E, Guo LJ, Hunt AJ. Nanoscale protein patterning by imprint lithography. Nano Lett 2004;4:853–7. doi:10.1021/nl049758x.

[153] Park I, Cheng J, Pisano AP, Lee ES, Jeong JH. Low temperature, low pressure nanoimprinting of chitosan as a biomaterial for bionanotechnology applications. Appl Phys Lett 2007;90:1–4. doi:10.1063/1.2709914.

[154] Jang MJ, Nam Y. Agarose-assisted micro-contact printing for high-quality biomolecular micro-patterns. Macromol Biosci 2015;15:613–21. doi:10.1002/mabi.201400407.

[155] Senesi AJ, Rozkiewicz DI, Reinhoudt DN, Mirkin CA. Agarose-assisted dip-pen nanolithography of oligonucleotides and proteins. ACS Nano 2009;3:2394–402. doi:10.1021/nn9005945.

[156] Tanaka N, Moriguchi H, Sato A, Kawai T, Shimba K, Jimbo Y, et al. Microcasting with agarose gel via degassed polydimethylsiloxane molds for repellency-guided cell patterning. RSC Adv 2016;6:54754–62. doi:10.1039/C6RA11563B.

[157] C. Bosshard, K. Sutter RS and PG. Electro-optic effects in molecular crystals. Josa B 1993;10:867–85. doi:10.1364/JOSAB.10.000867.

[158] CHAPTER 4 Application of Electro-Optic Materials: Design of Polymeric Optical Modulators n.d.;1:135–61.

[159] Tomlinson WJ, Brackett CA. Telecommunications Applications of Integrated Optics and Optoelectronics. Proc IEEE 1987;75:1512–23. doi:10.1109/PROC.1987.13912.

[160] Taylor HF. Application of Guided-Wave Optics in Signal Processing and Sensing. Proc IEEE 1987;75:1524–35. doi:10.1109/PROC.1987.13913.

[161] Maldonado TA. Electro-Optic Modulators n.d.

[162] Oh M-C, Zhang H, Szep A, Chuyanov V, Steier WH, Zhang C, et al. Electro-optic polymer modulators for 1.55 μm wavelength using phenyltetraene bridged chromophore in polycarbonate. Appl Phys Lett 2000;76:3525–7. doi:10.1063/1.126695.

[163] H-pdlcs HPLC, Bunning TJ, Natarajan L V, Sutherland RL, Tondiglia VP. 11 . 1 : Invited Paper : Switchable Reflective Displays Formed from 2000:121–3.

[164] Presnyakov V, Asatryan K, Galstian T, Chigrinov V. Optical polarization grating induced liquid crystal micro-structure using azo-dye command layer. Opt Express 2006;14:10558–64. doi:10.1364/OE.14.010558.

[165] Su W-C, Huang C-Y, Chen J-Y, Su W-H. Effect of recording-beam ratio on diffraction efficiency of polarization holographic gratings in dye-doped liquid-crystal films. Opt Lett 2010;35:405–7. doi:10.1364/OL.35.000405.

[166] Jepsen M Lou, Gerritsen HJ. Liquid-crystal-filled gratings with high diffraction efficiency. Opt Lett 1996;21:1081–3. doi:10.1364/OL.21.001081.

[167] Marthandappa M, Somashekar R, Nagappa. Electro???optic effects in nematic liquid crystals. Phys Status Solidi 1991;127:259–63. doi:10.1002/pssa.2211270129.

[168] Tamaoki N. Cholesteric Liquid Crystals for Color Information Technology. Adv Mater 2001;13:1135–47. doi:10.1002/1521-4095(200108)13:15<1135::AID-ADMA1135>3.0.CO;2-S.

[169] McMillan W. Simple Molecular Model for the Smectic A Phase of Liquid Crystals. Phys Rev A 1971;4:1238–46. doi:10.1103/PhysRevA.4.1238.

[170] Helfrich W. Electric Alignment of Liquid Crystal. Mol Cryst Liq Cryst 1973;21:187–209. doi:10.1080/15421407308083319.

[171] Litton CW, Collins TC, Reynolds DC, Litton CW. Physical review letters 5 1965;22:25–9.

[172] Schadt M, Helfrich W. Voltage-dependent optical activity of a twisted nematic liquid crystal. Appl Phys Lett 1971;18:127–8. doi:10.1063/1.1653593.

[173] Bezrodna T, Melnyk V, Vorobjev V, Puchkovska G. Low-temperature photoluminescence of 5CB liquid crystal. J Lumin 2010;130:1134–41. doi:10.1016/j.jlumin.2010.02.009.

[174] Lebovka N, Melnyk V, Klishevich G. Low temperature phase transformations in 4-cyano-4 ' -pentylbiphenyl (5CB) filled by multiwalled carbon nanotubes n.d.:1–9.

[175] O'Neill M, Kelly SM. Photoinduced surface alignment for liquid crystal displays. J Phys D Appl Phys 2000;33:667.

[176] Khot SA. Enhancement of thermal storage system using phase change material. Energy Procedia 2014;54:142–51. doi:10.1016/j.egypro.2014.07.257.

[177] Matharu AS, Jeeva S, Ramanujam PS. Liquid crystals for holographic optical data storage. Chem Soc Rev 2007;36:1868. doi:10.1039/b706242g.

[178] Yakunin S, Gayvoronsky V, Miniewicz A, Sworakowski J. Nanosecond laser pulse-induced refractive index changes in anthraquinone-doped liquid crystal. Mol Cryst Liq Cryst 2008;496:310–21. doi:10.1080/15421400802451923.

[179] Sengupta A. 2013 Topological Microfluidics. 2013. doi:10.1007/978-3-319-00858-5.

[180] Bogi A, Faetti S. Elastic, dielectric and optical constants of 4′-pentyl-4-cyanobiphenyl. Liq Cryst 2001;28:729–39. doi:10.1080/02678290010021589.

[181] Shi Z, Shao L, Wang F, Deng F, Liu Y, Wang Y. Fabrication of dye-doped polymer-dispersed liquid crystals with low driving voltage based on nucleophile-initiated thiol-ene click reaction. Liq Cryst 2017;45:1–7. doi:10.1080/02678292.2017.1360955.

[182] Ahmad F, Jamil M, Jeon YJ, Woo LJ, Jung JE, Jang JE. Investigation of nonionic diazo dye-doped polymer dispersed liquid crystal film. Bull Mater Sci 2012;35:221–31. doi:10.1007/s12034-012-0286-6.

[183] Montgomery GP, West JL, Tamura-Lis W. Light scattering from polymer-dispersed liquid crystal films: Droplet size effects. J Appl Phys 1991;69:1605–12. doi:10.1063/1.347256.

[184] Ramanitra H, Chanclou P, Vinouze B, Dupont L. Application of Polymer Dispersed Liquid Crystal (Pdlc) Nematic: Optical-Fiber Variable Attenuator. Mol Cryst Liq Cryst 2003;404:57–73. doi:10.1080/15421400390249952.

[185] Majles Ara MH, Seidali Z. The effect of Sudan dyes concentration in the linear dichroism of the nematic liquid crystals. Optik (Stuttg) 2015;126:297–300. doi:10.1016/j.ijleo.2014.08.161.

[186] Majles Ara MH, Mousavi SH, Salmani S, Koushki E. Measurement of nonlinear refraction of dyes doped liquid crystal using moiré deflectometry. J Mol Liq 2008;140:21–4. doi:10.1016/j.molliq.2007.12.009.

[187] Frederiks WM. Histochemistry in Lipid Histochemistry 1977;37:27–37.

[188] Fatriansyah JF, Yusuf Y. Dynamic Freedericksz Transition in the Nematic Liquid Crystals Incorporating Elastic Constant k 24 Dynamic Freedericksz Transition in the Nematic Liquid Crystals Incor- porating Elastic Constant k 24 2009.

[189] Zolina V. Forces Causing the Orientation of an Anisotropic Liquid . 1933.

[190] B.J. Frisken* and P. Palffy-Muhoray. Freedericksz transitions in nematic liquid crystals: The effects of an in-plane electric field 1989;40:6099–102.

[191] Robert H. Chen. Liquid Crystal Displays Fundamental Physics and Technology. Hoboken, New Jersey: 2011.

[192] Al-Azzawi A. Light and Optics principles and Practices. 2006.

[193] Kakani SL, Kakani A. Material Science 2004:657. doi:10.1063/1.3050638.

[194] Brown MS, Arnold CB. Fundamentals of Laser-Material Interaction and Application to Multiscale Surface Modification n.d.:91–120. doi:10.1007/978-3-642-10523-4.

[195] Hecht E. fifth edition 5 Optics. n.d.

[196] Jenkins FA, White HE. Fundamentals of Optics. n.d.

[197] Optical Society of America. Handbook of Optics. 2004. doi:10.1119/1.11846.

[198] Greivenkamp JE. Field guide to geometrical optics. 2004. doi:10.1117/3.547461.

[199] Asha S, Sangappa Y, Ganesh S. Tuning the Refractive Index and Optical Band Gap of Silk Fibroin Films by Electron Irradiation. J Spectrosc 2015;2015:879296/1-7. doi:10.1155/2015/879296.

[200] Tuma FA. The Optical Constants of Poly Methyl Methacrylate PMMA Polymer Doped by Alizarin Red Dye 2016:13–8.

[201] Al-Taa'Y WA, Oboudi SF, Yousif E, Abdul Nabi M, Yusop RM, Derawi D. Fabrication and characterization of nickel chloride doped PMMA films. Adv Mater Sci Eng 2015;2015. doi:10.1155/2015/913260.

[202] Jenkins FA, White He. Fundamentals of Optics. n.d.

[203] Greivenkamp JE. Field guide to geometrical optics. 2004. doi:10.1117/3.547461.

[204] Peter WM, Joseph HE. Lasers. United States of America: 1988.

[205] M. R. B. Andreeta. ArF Excimer Laser Annealing of Polycrystalline Silicon Thin Film. Cryst. - Sci. Technol., 2013, p. 485–486.

[206] Basting D. Excimer laser technology. Lamda Phys AG 2001.

[207] Rao MC. Review Article A Brief Introduction to Excimer Lasers : Fundamental Study 2013;2:533–6.

[208] Basting D, Pippert K, Stamm U, Ag LP. History and future prospects of excimer laser technology 2002;43:14–22.

[209] W. W. Duely. UV Lasers: effects and applictions in materials science. University of cambridge press; 1996.

[210] Prof. Dr. Frank Trager (Ed.). Springer Handbook of Lasers and Optics. Second Edi. Kassel, Germany: 2012. doi:10.1007/978-3-642-19409-2.

[211] Chen T, Darling R. Fundamentals of Laser Ablation of the Materials Used in Microfluiducs. IntechopenCom n.d.;m. doi:10.5772/1364.

[212] Kim M, Kim D, Kim D, Kang Y. Analysis of laser-induced damage during laser ablation process using picosecond pulse width laser to fabricate highly efficient PERC cells. Sol Energy 2014;108:101–6. doi:10.1016/j.solener.2014.06.020.

[213] J. Perriere EM and EF. Recent Advances in Laser Processing of Materials. First Edit. 2006.

[214] Wyant JC. White light interferometry. Proc SPIE - Int Soc Opt Eng 2002;4737:98–107. doi:10.1117/12.474947.

[215] Sathiamoorthy K, Ahmed T. Construction and Validation of a White Light Interferometer Construction and Validation of a White Light 2010.

[216] Lippert T. Polymers and Light. Polym Light 2004;168:51–246. doi:10.1007/b12437.

[217] Mojtaba Kahrizi. Micromachining Techniques for Fabrication of Micro and Nano Structures. n.d. doi:DOI: 10.5772/1364.

[218] Zakariyah SS. Laser Ablation for Polymer Waveguide Fabrication. Micromach Tech Fabr Micro Nano Struct 2012:109–30. doi:10.5772/1364.

[219] Jackson SR, Metheringham WJ, Dyer PE. Excimer laser ablation of Nd: YAG and Nd: glass. Appl Surf Sci 1995;86:223–7. doi:10.1016/0169-4332(94)00415-3.

[220] Hashida M, Semerok a. F, Gobert O, Petite G, Izawa Y, Wagner JF. Ablation threshold dependence on pulse duration for copper. Appl Surf Sci 2002;197–198:862–7. doi:10.1016/S0169-4332(02)00463-4.

[221] Zimmer K. Laser Processing and Chemistry. vol. 208. 1999. doi:10.1524/zpch.1999.208.Part_1_2.291a.

[222] Lemoine P, Blau W. Photoablation of polymers. Appl Surf Sci 1992;54:240–3. doi:10.1016/0169-4332(92)90051-X.

[223] Lippert T. UV Laser Ablation of Polymers : From Structuring to Thin Film Deposition n.d.

[224] Processing LM. No Title. n.d.

[225] D.Laude L. Excimer Lasers. vol. 265. 1994. doi:10.1007/978-94-015-8104-2.

[226] Tatiana E. Itina. Laser ablation-From fundamentals to applications. InTech, Chapters published December 21, 2017 under CC BY 3.0 license; 2017. doi:10.5772/67961.

[227] Lawrence J (Jonathan). Advances in laser materials processing : technology, research and applications. 2010.

[228] Russo RE, Mao X, Gonzalez JJ, Zorba V, Yoo J. Laser ablation in analytical chemistry. Anal Chem 2013;85:6162–77. doi:10.1021/ac4005327.

[229] LaHaye NL, Harilal SS, Diwakar PK, Hassanein A. The effect of laser pulse duration on ICP-MS signal intensity, elemental fractionation, and detection limits in fs-LA-ICP-MS. J Anal At Spectrom 2013;28:1781. doi:10.1039/c3ja50200g.

[230] Kappes RS, Schönfeld F, Li C, Golriz A a, Nagel M, Lippert T, et al. A study of photothermal laser ablation of various polymers on microsecond time scales. Springerplus 2014;3:489. doi:10.1186/2193-1801-3-489.

[231] Laser Processing and Chemistry. n.d.

[232] Bityurin N, Luk BS, Hong MH, Chong TC. Models for Laser Ablation of Polymers 2003.

[233] Serafetinides a. a., Spyratou E, Makropoulou M. Laser ablation and high precision patterning of biomaterials and intraocular lenses A.A. 2010;7747:77470V–77470V–14. doi:10.1117/12.882844.

[234] Spear JD, Russo RE. Transverse photothermal beam deflection within a solid. J Appl Phys 1991;70:580–6. doi:10.1063/1.349659.

[235] Krajnovich DJ. Near-Threshold Photoablation Characteristics of Polyimide and Poly(ethylene terephthalate). J Appl Phys 1997;82:427–35. doi:10.1063/1.366290.

[236] Rinaudo M. Chitin and chitosan: Properties and applications. Prog Polym Sci 2006;31:603–32. doi:10.1016/j.progpolymsci.2006.06.001.

[237] Bansal V, Sharma PK, Sharma N, Pal OP, Malviya R. Applications of Chitosan and Chitosan Derivatives in Drug Delivery. Biol Res 2011;5:28–37. doi:10.1007/12.

[238] Sinha VR, Singla AK, Wadhawan S, Kaushik R, Kumria R, Bansal K, et al. Chitosan microspheres as a potential carrier for drugs. Int J Pharm 2004;274:1–33. doi:10.1016/j.ijpharm.2003.12.026.

[239] Rabea EI, Badawy MET, Stevens C V., Smagghe G, Steurbaut W. Chitosan as antimicrobial agent: Applications and mode of action. Biomacromolecules 2003;4:1457–65. doi:10.1021/bm034130m.

[240] Croisier F, Jérôme C. Chitosan-based biomaterials for tissue engineering. Eur Polym J 2013;49:780–92. doi:10.1016/j.eurpolymj.2012.12.009.

[241] Voznesenskiy SS, Sergeev AA, Mironenko AY, Bratskaya SY, Kulchin YN. Integrated-optical sensors based on chitosan waveguide films for relative humidity measurements. Sensors Actuators, B Chem 2013;188:482–7. doi:10.1016/j.snb.2013.07.043.

[242] Camilo CS, dos Santos DS, Rodrigues JJ, Vega ML, Campano Filho SP, Oliveira ON, et al. Surface-relief gratings and photoinduced birefringence in layer-by-layer films of chitosan and an azopolymer. Biomacromolecules 2003;4:1583–8. doi:10.1021/bm034220r.

[243] Nosal WH, Thompson DW, Yan L, Sarkar S, Subramanian A, Woollam JA. UV-vis-infrared optical and AFM study of spin-cast chitosan films. Colloids Surfaces B Biointerfaces 2005;43:131–7. doi:10.1016/j.colsurfb.2004.08.022.

[244] Da Róz AL, Leite FL, Pereiro L V., Nascente PAP, Zucolotto V, Oliveira ON, et al. Adsorption of chitosan on spin-coated cellulose films. Carbohydr Polym 2010;80:65–70. doi:10.1016/j.carbpol.2009.10.062.

[245] Lieder R, Darai M, Orlygsson G, Sigurjonsson OE. Solution casting of chitosan membranes for in vitro evaluation of bioactivity. Biol Proced Online 2013;15:11. doi:10.1186/1480-9222-15-11.

[246] Li S, Wu Z, Li B, Zhu R, Wang Y. Chitosan resins synthesised by improved drop-sphere-forming method for Cr(VI) removal from aqueous solutions. Water Sci Technol 2012;66:2461–7. doi:10.2166/wst.2012.437.

[247] Lazare S, Tokarev V, Sionkowska A, Wi??niewski M. Surface foaming of collagen, chitosan and other biopolymer films by KrF excimer laser ablation in the photomechanical regime. Appl Phys A Mater Sci Process 2005;81:465–70. doi:10.1007/s00339-005-3260-y.

[248] Dyer PE, Srinivasan R. Nanosecond photoacoustic studies on ultraviolet laser ablation of organic polymers. Appl Phys Lett 1986;48:445–7. doi:10.1063/1.96526.

[249] Kermani O, Lubatschowski H. [Structure and dynamics of photo-acoustic shock-waves in 193 nm excimer laser photo-ablation of the cornea]. Fortschr Ophthalmol 1991;88:748–53.

[250] Doukas AG, Flotte TJ. Physical characteristics and biological effects of laser-induced stress waves. Ultrasound Med Biol 1996;22:151–64. doi:10.1016/0301-5629(95)02026-8.

[251] Landau LD, Lifshitz EM, Sykes JB, Reid WH, Dill EH. Theory of Elasticity: Vol. 7 of Course of Theoretical Physics. Phys Today 1960;13:44. doi:10.1063/1.3057037.

[252] Itzkan I, Albagli D, Dark ML, Perelman LT, Rosenberg C V, Feld MS. The Thermoelastic Basis

of Short Pulsed Laser Ablation of Biological Tissue. Pnas 1995;92:1960–4. doi:10.1073/pnas.92.6.1960.

[253] Albagli D, Dark M, von Rosenberg C, Perelman L, Itzkan I, Feld MS. Laser-induced thermoelastic deformation: A three-dimensional solution and its application to the ablation of biological tissue. Med Phys 1994;21:1323–31. doi:10.1118/1.597202.

[254] Goodier JN. On the integration of the thermoelastic equations. Philos Mag 1937;23:1017–32.

[255] Carome EF, Clark NA, Moeller CE. Generation of acoustic signals in liquids by ruby laser-induced thermal stress transients. Appl Phys Lett 1964;4:95–7. doi:10.1063/1.1753985.

[256] Paltauf G, Dyer PE. Photomechanical processes and effects in ablation. Chem Rev 2003;103:487–518. doi:10.1021/cr010436c.

[257] Lazare S, Elaboudi I, Castillejo M, Sionkowska A. Model properties relevant to laser ablation of moderately absorbing polymers. Appl Phys A Mater Sci Process 2010;101:215–24. doi:10.1007/s00339-010-5754-5.

[258] Singh S. Diffraction gratings: Aberrations and applications. Opt Laser Technol 1999;31:195–218. doi:10.1016/S0030-3992(99)00019-5.

[259] Seward GH. Basic Physical Optics. Fundam Photonics 2008:35–51. doi:10.1117/3.855480.ch5.

[260] Design DO, Shea DCO, Suleski TJ, Alan D, Prather DW, Tt V, et al. Diffractive Optics. n.d.

[261] Hutley MC, Loewen EG, Verrill JF, Verrill JF, Wilson IJ, Botten LC, et al. Diffraction gratings (manufacture) n.d.

[262] Nguyen HT, Shore BW, Bryan SJ, Britten J a, Boyd RD, Perry MD. High-efficiency fused-silica transmission gratings. Opt Lett 1997;22:142–4.

[263] BRON M, MA, Dr Phil F, EMIL WOLF, PhD Ds. Principles of optics: Electromagnetic theory of propaqation interference and diffraction of light. Seventh Ed. United Kingdom, University Press, Cambridge: 1999.

[264] Loeweh E. Diffraction Grating and Applications. 1197.

[265] Frank L. Pedrotti SJ, Pedrotti LS. Introduction to Optics. Third Edit. United States: 2007.

[266] Frank L. Pedrotti SJ, Pedrotti LS. Introduction to Optics. Second Edi. United States: 1993.

[267] Zhang S, Mi X, Zhang Q, Feng S, Yu H, Qi X. Groove shape characteristics of echelle gratings with high diffraction efficiency. Opt Commun 2016;387:1–0. doi:10.1016/j.optcom.2016.10.063.

[268] Hatsui T, Setoyama H, Shigemasa E, Kosugi N. Design of a novel transmission-grating spectrometer for soft X-ray emission studies. J Electron Spectros Relat Phenomena 2005;144–147:1059–62. doi:10.1016/j.elspec.2005.01.074.

[269] Loeweh E. Diffraction Grating and Applications. New York, United States of America: 1197.

[270] Namioka T. 17. Diffraction Grating. Takeshi Namioka. vol. 31. 1998.

[271] Gaylord TK, Moharam MG. Analysis and applications of optical diffraction by gratings. Proc IEEE 1985;73:894–937. doi:10.1109/PROC.1985.13220.

[272] Corporation O. Optometrics Corporation. Technology n.d.:1–32.

[273] Palmer, Jr. CH. Diffraction Grating Handbook. J Opt Soc Am 2005;46:271. doi:10.1364/JOSA.46.000050.

[274] Giles MK, Hughes RS, Thompson JL. Angular dispersion of diffraction gratings used for tuning organic dye lasers. Appl Opt 1973;12:421. doi:10.1364/AO.12.000421.

[275] Mäder M. Nano-Patterning by Diffraction Mask-Projection Laser Ablation. J Laser Micro/Nanoengineering 2008;3:9–13. doi:10.2961/jlmn.2008.01.0003.

[276] Chen Y, Li Z, Zhang Z, Psaltis D, Scherer A. Nanoimprinted circular grating distributed feedback dye laser Nanoimprinted circular grating distributed feedback dye laser 2016;51109:89–92. doi:10.1063/1.2757600.

[277] Lin CH, Lin YM, Liang CC, Lee YY, Fung HS, Shew BY, et al. Extreme UV diffraction grating fabricated by nanoimprint lithography. Microelectron Eng 2012;98:194–7. doi:10.1016/j.mee.2012.07.037.

[278] Lim H, Kim G, Choi KB, Jeong M, Ryu J, Lee J. Nanoimprint lithography with a soft roller and focused UV light for flexible substrates. Microelectron Eng 2012;98:279–83. doi:10.1016/j.mee.2012.04.030.

[279] Desaute P, Merdji H, Greiner V, Missalla T, Chenais-Popovics C, Troussel P. Characterization of a high resolution transmission grating. Opt Commun 2000;173:37–43.

[280] Sailaja S, Arora V, Kumbhare SR, Naik PA, Gupta PD. Study of di€ raction e• ciency of a free-standing transmission grating in keV spectral region using laser produced plasmas 1998;30:407–10.

[281] Newport. The Physics of Diffrcation Excerpt from Diffraction Grating Handbook - 2005:20–42.

[282] Fattinger C. The bidiffractive grating coupler. Appl Phys Lett 1993;62:1460–2. doi:10.1063/1.108658.

[283] Karasiński P. Sensor properties of planar waveguide structures with grating couplers. Opto-Electronics Rev 2007;15:168–78. doi:10.2478/s11772-007-0018-4.

[284] Wang Y, Flueckiger J, Lin C, Chrostowski L. Universal grating coupler design 2013:89150Y. doi:10.1117/12.2042185.

[285] Xiao Z, Luan F, Liow T-Y, Zhang J, Shum P. Design for broadband high-efficiency grating couplers. Opt Lett 2012;37:530. doi:10.1364/OL.37.000530.

[286] Laere FVLF Van, Kotlyar MVKM V., Taillaert DTD, Thourhout DVTD Van, Krauss TFKTF, Baets RBR. Compact Slanted Grating Couplers Between Optical Fiber and InP–InGaAsP Waveguides. IEEE Photonics Technol Lett 2007;19:151–6. doi:10.1109/LPT.2007.891975.

[287] Avrutsky IA, Svakhin AS, Sychugov VA, Parriaux O. High-efficiency single-order waveguide grating coupler. Opt Lett 1990;15:1446–8. doi:10.1364/OL.15.001446.

[288] Halir R, Cheben P, Janz S, Xu D-X, Molina-Fernández I, Wangüemert-Pérez JG. Waveguide grating coupler with subwavelength microstructures. Opt Lett 2009;34:1408–10. doi:10.1364/OL.34.001408.

[289] Orobtchouk R, Layadi a, Gualous H, Pascal D, Koster a, Laval S. High-Efficiency Light Coupling in a Submicrometric Silicon-on-Insulator Waveguide. Appl Opt 2000;39:5773–7. doi:10.1364/AO.39.005773.

[290] Li L, Gupta MC. Effects of beam focusing on the efficiency of planar waveguide grating couplers. Appl Opt 1990;29:5320–5. doi:10.1364/AO.29.005320.

[291] Wang Y, Wang X, Flueckiger J, Yun H, Shi W, Bojko R, et al. Focusing sub-wavelength grating couplers with low back reflections for rapid prototyping of silicon photonic circuits. Opt Express 2014;22:20652–62. doi:10.1364/OE.22.020652.

[292] Ding Y, Peucheret C, Ou H, Yvind K, Ding Y, Peucheret C, et al. Fully etched apodized grating coupler on the SOI platform with – 0 . 58 dB coupling efficiency To cite this version : Fully etched apodized grating coupler on the SOI platform with − 0 . 58 dB coupling efficiency 2014:0–3.

[293] Tiefenthaler K, Lukosz W. Integrated optical switches and gas sensors. Opt Lett 1984;9:137–9. doi:10.1364/OL.9.000137.

[294] Tiefenthaler K, Lukosz W. Sensitivity of grating couplers as integrated-optical chemical sensors. J Opt Soc Am B 1989;6:209. doi:10.1364/JOSAB.6.000209.

[295] Harvey EC, Rumsby PT. Fabrication techniques and their application to produce novel micromachined structures and devices using excimer laser projection</title> 1997:26–33. doi:10.1117/12.284497.

[296] Marin L, Popescu MC, Zabulica A, Uji-I H, Fron E. Chitosan as matrix for bio-polymer dispersed

liquid crystal systems. Carbohydr Polym 2013;95:16–24. doi:10.1016/j.carbpol.2013.02.028.

[297] Lienhard IV JH, Lienhard V JH. A HEAT TRANSFER TEXTBOOK, fourth edition. Phlogist Press 2012:766. doi:978-04864793161.

[298] Cengel YA. Heat Transfer: A Practical Approach. Mc Graw-Hill 2003:785–841.

[299] Favre-marinet M, Tardu S. Convective Heat Transfer. 2009. doi:10.1002/9780470611890.

[300] Heat S, Through G. F undamentals of Microwaves 2002:561–604.

[301] Incropera FP, DeWitt DP, Bergman TL, Lavine AS. Introduction to Conduction. Fundam Heat Mass Transf 2007:997. doi:10.1016/j.applthermaleng.2011.03.022.

[302] Brno University of Technology Transfer and Fluid Flow Labora Ph . D . Thesis (Diserta č ní práce) Topic : (Inverzní úlohy mechaniky s vazbou na technický experiment) 2006.

[303] Watanabe H, Seong DJ. The Thermal Conductivity and Thermal Diffusivity of Liquid n-Alkanes: C^nH_2n+2 (n=5 to 10) and Toluene. Int J Thermophys 2002;23:337–56. doi:10.1023/A:1015158401299.

[304] Soltanolkotabi M, Bennis GL, Gupta R. Temperature dependence of the thermal diffusivity of GaAs in the 100-305 K range measured by the pulsed photothermal displacement technique. J Appl Phys 1999;85:794–8. doi:10.1063/1.369161.

[305] COMSOL Multiphysics. Introduction to Heat Transfer Module. Manual 2012:1–34.

[306] COMSOL. Introduction to COMSOL Multiphysics 5.3. Manual 2014:168.

[307] Dong Y, Ruan Y, Wang H, Zhao Y, Bi D. Studies on glass transition temperature of chitosan with four techniques. J Appl Polym Sci 2004;93:1553–8. doi:10.1002/app.20630.

[308] Sakurai K, Maegawa T, Takahashi T. Glass transition temperature of chitosan and miscibility of chitosan/poly(N-vinyl pyrrolidone) blends. Polymer (Guildf) 2000;41:7051–6. doi:10.1016/S0032-3861(00)00067-7.

[309] Group F. Chitosan- based Hydrogels. 2012.

[310] Rinaudo M. Chitin and chitosan: Properties and applications. Prog Polym Sci 2006;31:603–32. doi:10.1016/j.progpolymsci.2006.06.001.

[311] Czechowska-biskup R, Jarosińska D, Rokita B, Ulański P, Rosiak JM. Determination of Degree of Deacetylation of Chitosan - Comparaison of Methods. Prog Chem Appl Chitin Its Deriv 2012;XVII:5–20.

[312] Aranaz I, Mengíbar M, Harris R, Paños I, Miralles B, Acosta N, et al. Functional Characterization of Chitin and Chitosan. Curr Chem Biol 2009;3:203–30. doi:10.2174/187231309788166415.

[313] Alvarenga ES De. Characterization and Properties of Chitosan. Biotechnol Biopolym 2011:91–108.

[314] Dutta PK, Duta J, Tripathi VS. Chitin and Chitosan: Chemistry, properties and applications. J Sci Ind Res (India) 2004;63:20–31. doi:10.1002/chin.200727270.

[315] Draget KI. Alginates. 2009.

[316] Burke, A. and Hasirci N. Biomaterials: From Molecules to Engineered Tissues. 2004.

[317] Kurita K. Controlled functionalization of the polysaccharide chitin. Prog Polym Sci 2001;26:1921–71. doi:10.1016/S0079-6700(01)00007-7.

[318] Oliveira BF, Santana MH a, Re MI. Spray-dried chitosan microspheres cross-linked with D,L-glyceraldehyde as a potential drug delivery system: Preparation and characterization. Brazilian J Chem Eng 2005;22:353–60.

[319] Mehta GK, Kondaveeti S, Siddhanta AK. Facile synthesis of agarose-l-phenylalanine ester hydrogels. Polym Chem 2011;2:2334. doi:10.1039/c1py00250c.

[320] Normand V, Lootens DL, Amici E, Plucknett KP, Aymard P. New insight into agarose gel mechanical properties. Biomacromolecules 2000;1:730–8. doi:10.1021/bm005583j.

[321] Hashemi P, Abolghasemi MM. Preparation of a novel optical sensor for low pH values using agarose membranes as support. Sensors Actuators, B Chem 2006;115:49–53. doi:10.1016/j.snb.2005.08.046.

[322] Wilchek M, Miron T. Thirty years of affinity chromatography. React Funct Polym 1999;41:263–8. doi:10.1016/S1381-5148(99)00042-5.

[323] Lindgren GES. Method of cross-linking a porous polysaccharide gel 1990:1–4.

[324] March SC, Parikh I, Cuatrecasas P. A simplified method for cyanogen bromide activation of agarose for affinity chromatography. Anal Biochem 1974;60:149–52. doi:10.1016/0003-2697(74)90139-0.

[325] Wang C, Zhou B, Jiang H, He S. Agarose Filled Fabry-Perot Cavity for Temperature Self-Calibration Humidity Sensing. IEEE Photonics Technol Lett 2016;28:2027–30. doi:10.1109/LPT.2016.2581990.

[326] Lee SH, Moon JJ, West JL. Three-dimensional micropatterning of bioactive hydrogels via two-photon laser scanning photolithography for guided 3D cell migration. Biomaterials 2008;29:2962–8. doi:10.1016/j.biomaterials.2008.04.004.

[327] Hashemi P, Abolghasemi MM, Alizadeh K, Zarjani RA. A calmagite immobilized agarose membrane optical sensor for selective monitoring of Cu2+. Sensors Actuators, B Chem 2008;129:332–8. doi:10.1016/j.snb.2007.08.033.

[328] Cheng S-Y, Heilman S, Wasserman M, Archer S, Shuler ML, Wu M. A hydrogel-based microfluidic device for the studies of directed cell migration. Lab Chip 2007;7:763–9. doi:10.1039/b618463d.

[329] Tourniaire G, Collins J, Campbell S, Mizomoto H, Ogawa S, Thaburet JF, et al. Polymer microarrays for cellular adhesion. Chem Commun 2006:2118–20. doi:10.1039/b602009g.

[330] Mourant JR, Bigio IJ, Jack D a, Johnson TM, Miller HD. Measuring absorption coefficients in small volumes of highly scattering media: source-detector separations for which path lengths do not depend on scattering properties. Appl Opt 1997;36:5655–61. doi:10.1364/AO.36.005655.

[331] Ahmed NM, Sauli Z, Hashim U, Al-douri Y. Investigation of the absorption coefficient , refractive index , energy band gap, and film thickness for Al0.11Ga0.89N by optical transmission method. Int J Nanoelectron Mater 2009;2:189–95.

[332] Ghanipour M, Dorranian D. Effect of Ag-Nanoparticles Doped in Polyvinyl Alcohol on the Structural and Optical Properties of PVA Films. J Nanomater 2013;2013. doi:10.1155/2013/897043.

[333] Hong PZ, Li SD, Ou CY, Li CP, Yang L, Zhang CH. Thermogravimetric analysis of chitosan. J Appl Polym Sci 2007;105:547–51. doi:10.1002/app.25920.

[334] Engineering E, E-mail P. Thermogravimetry of Chitosan with Nanofillers Anna Puchalska , Maria Mucha n.d.;XVI:31–42.

[335] Huang Y, Paul DR. Dielectric Relaxations of Chitosan: The Effect of Water on the a-Relaxation and the Glass Transition Temperature. J Polym Sci Part B Polym Phys 2007;45:1390–8. doi:10.1002/polb.

[336] Lazaridou A, Biliaderis CG. Thermophysical properties of chitosan, chitosan-starch and chitosan-pullulan films near the glass transition. Carbohydr Polym 2002;48:179–90. doi:10.1016/S0144-8617(01)00261-2.

[337] Zhang LM, Wu CX, Huang JY, Peng XH, Chen P, Tang SQ. Synthesis and characterization of a degradable composite agarose/HA hydrogel. Carbohydr Polym 2012;88:1445–52. doi:10.1016/j.carbpol.2012.02.050.

[338] Gobbi PG, Carones F, Brancato R, Pini R, Siano S. Acoustic transients following excimer laser ablation of the cornea. Eur J Ophthalmol 1995;5:275–6.

[339] Cross FW, Al-Dhahir RK, Dyer PE, MacRobert AJ. Time-resolved photoacoustic studies of vascular tissue ablation at three laser wavelengths. Appl Phys Lett 1987;50:1019–21. doi:10.1063/1.97994.

[340] Lazare S, Bonneau R, Gaspard S, Oujja M, de Nalda R, Castillejo M, et al. Dynamics of one laser pulse surface nanofoaming of biopolymers. J Laser Micro Nanoeng 2009;4:152–8. doi:10.2961/jlmn.2009.03.0002.

[341] Dyer PE, Walton CD, Akeel K a. Coherence effects in surface roughness induced by vacuum ultraviolet F_2 laser ablation. Opt Lett 2005;30:1336–8. doi:10.1364/OL.30.001336.

[342] Ara MHM, Seidali Z, Mousavi SH. Electro-Optical Properties of Dye-Doped Nematic Liquid Crystals. Mol Cryst Liq Cryst 2010;526:130–8. doi:10.1080/15421406.2010.485531.

[343] Tumuluri A, Naidu KL, Raju KCJ. Band gap determination using Tauc 's plot for LiNbO3 thin films. Int J ChemTech Res 2014;6:3353–6.

[344] Pelzl G, Hauser A. Birefringence and phase transitions in liquid crystals. Phase Transitions 1991;37:33–62. doi:10.1080/01411599108203447.

[345] Eakin JN, Xie Y, Pelcovits RA, Radcliffe MD, Crawford GP. Zero voltage Freedericksz transition in periodically aligned liquid crystals. Appl Phys Lett 2004;85:1671–3. doi:10.1063/1.1789578.

[346] Lucchetti L, Gentili M, Simoni F, Pavliuchenko S, Subota S, Reshetnyak V. Surface-induced nonlinearities of liquid crystals driven by an electric field. Phys Rev E - Stat Nonlinear, Soft Matter Phys 2008;78. doi:10.1103/PhysRevE.78.061706.